Development of a self-contained approach for estimating space-time changes of seismic scattering properties based on seismic interferometry

博士論文

Development of a self-contained approach for estimating space-time changes of seismic scattering properties based on seismic interferometry

（地震波干渉法に基づく地震波散乱特性の時空間変化推定のための自己完結的手法の構築）

廣瀬　郁

令和元年

Doctoral Thesis

Development of a self-contained approach for estimating space-time changes of seismic scattering properties based on seismic interferometry

[地震波干渉法に基づく地震波散乱特性の時空間変化推定のための自己完結的手法の構築]

Takashi Hirose
(廣瀬　郁)

Department of Geophysics
Graduate School of Science
Tohoku University

Thesis Committee Members

Associate Professor	Hisashi	Nakahara	(Chair, Supervisor)
Professor	Takeshi	Nishimura	
Professor	Michel	Campillo	(Université Grenoble Alpes)
Dr.	Eric	Larose	(ISTerre, Université Grenoble Alpes)
Professor	Ryota	Hino	
Associate Professor	Tomomi	Okada	

2019

Acknowledgement

Foremost, I would like to express my gratitude to my advisor Associate Prof. Hisashi Nakahara for the continuous guidance and advice throughout my Ph.D study, for his patience, motivation and enthusiasm. I could not accomplish the present study without his support and encouragement. I would also like to express my sincere appreciation to Prof. Takeshi Nishimura for his valuable advice and useful comments to develop my study.

I also would like to express my gratitude to Prof. Michel Campillo for his continuous support and valuable advice. Chapter3 of this thesis, which was conducted while I was in Grenoble, could not be completed without his guidance and helpful comments. I would like to thank Dr. Eric Larose for providing me with opportunities to discuss the results and for giving me many constructive comments.

I am very thankful to Prof. Ryota Hino and Associate Prof. Tomomi Okada, for their invaluable comments on this study. I would like to thank Emeritus Prof. Haruo Sato for his many constructive advice to my research. Also, I would like to thank Associate Prof. Tomofumi Kozono, Assistant Prof. Kentaro Emoto, and Assistant Prof. Masayuki Kano for their valuable advice on my work and for their help during my studies. I express my gratitude to all the professors of the Research Center for Prediction of Earthquakes and Volcanic Eruptions for their comments and discussions in the weekly seminar.

My sincere thanks also go to Dr. Qingyu Wang, for useful discussions and all her help related to my stay in Grenoble. I am deeply grateful to all members of Solid Earth Physics Laboratory, Research Center for Prediction of Earthquakes, ISTerre, and the International Joint Graduate Program in Earth and Environmental Sciences (GP-EES) for stimulating discussions and for all the fun we have had. Many thanks to Ms. Chika Kamada, Ms. Naoko Mizuta and Ms. Shinobu Okuyama for all their help.

I thank the Japan Meteorological Agency for providing us with continuous seismic data. I also used seismograms obtained from the active seismic experiments conducted by the Disaster Prevention Research Institute, Kyoto University along with eight other Japanese universities and JMA at Sakurajima that were lead by Tomoki Tsutsui and Masato Iguchi. I am also grateful to the National Research Institute for Earth Science and Disaster Resilience for providing us with continuous seismic data.

This work was supported by the Japan Society for the Promotion of Science (JSPS), the

Ministry of Education, Culture, Sports, Science and Technology (MEXT) of Japan, under its Earthquake and Volcano Hazards Observation and Research Program, and GP-EES. I am also grateful to the Integrated Program from Next Generation Volcano Research and Human Resource Development.

Finally, I would like to express my deep and sincere gratitude to my family for their continuous supports and encouragements.

Abstract

Seismic interferometry enables us to estimate changes in seismic velocity and seismic scattering property continuously by using cross-correlation functions (CCFs) of seismic ambient noise. In recent years, spatial distributions of seismic velocity changes associated with volcanic activities or earthquakes have been estimated at many places over the world. On the other hand, there are only a few previous studies that applied seismic interferometry to detect seismic scattering property changes related to volcanic activities or earthquakes. To estimate spatial distributions of seismic scattering property changes using linear least-squares inversions, it is necessary to know the values of scattering and intrinsic absorption parameters in a study area. These parameters are measures of medium heterogeneities, and have been estimated by using the data of natural earthquakes or active shot records. Therefore, it is difficult to estimate those parameters in the regions of low seismicity and no active seismic experiment.

In chapter 2, we overcome such a limitation by developing a passive method for the estimation of scattering and intrinsic absorption parameters using seismic ambient noise CCFs. Firstly, we apply and validate the method at Sakurajima volcano, Japan. The scattering mean free paths and intrinsic absorption parameters estimated from the passive method are 1.6-2.4 km and 0.04-0.06 s^{-1} at 0.5-1 Hz, 1.6-2.0 km and 0.08-0.09 s^{-1} at 1-2 Hz, and 1.6-3.2 km and 0.16-0.18 s^{-1} at 2-4 Hz, respectively. The validity of these results is confirmed at the 1-2 Hz and 2-4 Hz bands by comparing with these parameters estimated from active shot records at Sakurajima. Secondly, we apply the passive method to the focal area of the 2008 Iwate-Miyagi Nairiku earthquake and Miyakejima volcano, Japan. These parameters in the focal area of the Iwate-Miyagi Nairiku earthquake are estimated to be 30 km and 0.02 s^{-1} at the 0.5-1 Hz band. In the case of Miyakejima, the scattering mean free paths are estimated to be 1.6 km at the 1-2 Hz band and 2.0 km at the 2-4 Hz band, respectively. The intrinsic absorption parameters are estimated to be 0.12 s^{-1} at the 1-2 Hz band and 0.16 s^{-1} at the 2-4 Hz band, respectively. The estimated scattering mean free paths at Sakurajima and Miyakejima were 2-3 orders shorter than those in non-volcanic regions.

In chapter 3, we conduct a time-lapse imaging of seismic scattering properties in a weak scattering regime using ordinary linear least-squares inversions. We apply seismic

interferometry to seismic ambient noise data in the northeast part of Japan between 2008 and 2012 during which we had two large earthquakes of the 2008 Iwate-Miyagi Nairiku earthquake and the 2011 Tohoku-Oki earthquake. About 5.7×10^{-4} km^{-1} of Δg value ($\Delta g/g_0$ = 5.7 %) is estimated around the epicenter of the 2008 Iwate-Miyagi Nairiku earthquake. Structural changes due to the large fault slip and/or the strong motion may have introduced such a large seismic scattering property change in the shallow medium to the south of the epicenter. We also detected significant seismic scattering property changes around some active volcanoes in Tohoku region associated with the 2011 Tohoku-Oki earthquake. The maximum change is estimated around the Bandai volcano and its Δg value is 3.6×10^{-4} km^{-1} ($\Delta g/g_0$ = 3.6 %). Significant seismic velocity changes and subsidences around active volcanoes in Tohoku region associated with the 2011 Tohoku-Oki earthquake have been reported by some previous studies. Our results also show that significant structural changes occurred in similar regions. In the southwest part of Tohoku region, strong seasonal seismic scattering property changes are detected. The maximum Δg value is estimated to be 3.0×10^{-4} km^{-1} ($\Delta g/g_0$=3.0 %) in winter. These regions are correlated with those of large precipitations.

In chapters 4 and 5, we develop imaging methods of seismic scattering property changes to extend their applicability. Firstly, in chapter 4, we apply sparse modeling to estimate the spatial distribution of seismic scattering property changes and succeeded in detecting large coseismic changes of seismic scattering property at the south of the epicenter of the 2008 Iwate-Miyagi Nairiku earthquake using 17 seismic stations. In general, it is difficult to conduct imagings from the small number of seismic stations. However, the sparse modeling enables us to conduct the imaging even from a small data set. The maximum value of Δg, a variation of scattering coefficient, at this region was estimated to be 0.032 km^{-1} ($\Delta g/g_0$ = 97 %). We also conduct the ordinary linear least-squares inversion with the ℓ^2 norm regularization, and confirm that the result from the sparse modeling and that from the ℓ^2 norm regularization are consistent. We explore the applicability of sparse modeling by reducing the number of seismic stations and confirm that we can retrieve the change regions from at least 5 stations which are deployed to surround the change regions.

In previous studies, the linear least-squares inversions have been used to estimate spatial distributions of seismic scattering property changes. However, it is not easy to apply the linear least-squares inversion in a multiple scattering regime. This is because the scattering at a change region of seismic scattering property is assumed to occur only once and the scattering mean free path is as small as about a few hundred meters to a few kilometers at some active volcanoes including Sakurajima and Miyakejima. Therefore,

we develop a method to estimate a region where seismic scattering property changed in a multiple scattering regime like volcanoes, and apply this method to the 2015 dike intrusion event at Sakurajima volcano. The estimated change region extended widely around active craters with 0.25 km^{-1} and 1.10 km^{-1} of Δg in the two periods of Apr. 1 - May 31 and Jul. 6 - Aug. 14, respectively, before the dike intrusion. The change region was located around the dike with 2.45 km^{-1} of Δg in the period of Aug. 16 - Sep. 15 after the dike intrusion.

In chapter 6, we discuss future developments of the space-time imaging of seismic scattering properties and structural monitoring with multi parameters.

In this thesis, we have developed a self-contained approach to the estimation of space-time changes of seismic scattering properties based on seismic interferometry. By applying the appropriate imaging method, we can locate significant seismic scattering changes both in a weak scattering regime and strong scattering regime. Moreover, the passive estimation of scattering and intrinsic absorption parameters and the sparse modeling will be useful to improve the applicability of the passive time-lapse imaging. By conducting imaging in various regions and comparing the results with other observations, relationships between seismic scattering changes and other changes will be understood. This should contribute to the monitoring of the dynamic Earth and the understanding of their physical mechanisms.

Contents

Chapter 1

Introduction

1.1 Estimation of scattering and intrinsic absorption parameters

Seismic scattering and intrinsic absorption parameters are measures of medium heterogeneities in the Earth. The small scale medium heterogeneities which are described by random velocity fluctuations cause scattering of seismic waves. Aki and Chouet [1975] introduced "scattering coefficient", which represents a scattering power per unit volume. On the other hand, the intrinsic absorption parameter represents energy loss per time caused by the conversion of elastic energy to heat or other forms of energy. The scattering and intrinsic absorption parameters have been estimated by many previous studies using data of natural earthquakes or active shots.

In the last few decades, some previous studies have estimated spatial distributions of the scattering coefficient assuming single scattering [e.g., *Nishigami*, 2000; *Matsumoto et al.*, 1999; *Asano and Hasegawa*, 2004]. For example, Asano and Hasegawa [2004] estimated the spatial distribution of the scattering coefficient of S-waves using aftershock seismograms of the 2000 M 7.3 western Tottori earthquake, and found the region of strong scattering along and around the fault zone. Multiple Lapse Time Window Analysis (MLTWA) have been widely used to estimate these eparameters from the data of natural earthquakes [e.g., *Fehler et al.*, 1992; *Hoshiba et al.*, 1993; *Carcolé and Sato*, 2010] or active shots [e.g., *Wegler and Lühr*, 2001; *Yamamoto and Sato*, 2010; *Prudencio et al.*, 2017]. Carcolé and Sato [2010] estimated the spatial distribution of scattering and intrinsic attenuation of S-waves in the lithosphere of Japan that reflects tectonic settings. The averaged scattering mean free path (the reciprocal of the scattering coefficient) of S-waves for all Japan was estimated to be about 100 km between 1 Hz and 16 Hz. On the other hand, much shorter scattering mean free paths have been reported at active volcanoes. For example, Wegler and Lühr [2001] estimated the mean free path of S-waves at Merapi volcano, Java to be about 100 m in the 4-20 Hz band using airgun shot records. Yamamoto and Sato [2010] estimated the scattering mean free path of S-waves at Asama volcano, Japan, to be about 1

km at the 8-16 Hz band using active shot records. The mean free paths at active volcanoes are 2-3 orders smaller than the mean values for all Japan obtained by Carcolé and Sato [2010].

These estimations of scattering and intrinsic absorption parameters need many natural earthquake data. Accordingly, this approach is difficult to apply at the regions of low seismicity. Active shot records can be used to estimate these parameters, but the number of regions where active seismic experiments are conducted is limited.

1.2 Imaging and monitoring of seismic scattering properties

Seismic scattering property changes cause waveform changes of seismograms [*Snieder et al.*,2002; *Snieder*, 2006]. Figure 1.1 is a schematic picture of the physical mechanism of waveform change. The seismic waves radiated from a source reach a receiver after some scatterings. If a change region of seismic scattering property appears in the medium, wave paths of seismic waves passing through the change region will be changed (blue and red lines). Such wave path changes due to the seismic scattering property change cause waveform changes [*Margerin et al.*, 2016]. Imaging of seismic scattering property changes have been developed in laboratory experiments [e.g., *Larose et al.*, 2010; *Planès et al.*, 2015; *Larose et al.*, 2015]. Larose et al. [2010] proposed a technique called "Locating a weak change using diffuse waves (LOCADIFF)". This technique uses the data of waveform changes on ultrasound records in MHz band and sensitivity kernels (spatial weighting functions). The previous studies have shown that we can locate a hole/crack in rock samples based on the LOCADIFF.

Seismic interferometry is a technique to estimate relative seismic velocity and seismic scattering property changes using cross-correlation functions (CCFs) of seismic ambient noise [e.g., *Shapiro and Campillo*, 2004; *Curtis et al.*, 2006]. In recent years, estimations of seismic velocity changes using seismic interferometry have been widely conducted by measuring changes of time shifts in CCFs [e.g., *Sens-Schönfelder and Wegler*, 2006; *Brenguier et al.*, 2008a; *Brenguier et al.*, 2014; *Wang et al.*, 2017; *Takano et al.*, 2017; *Hirose et al.*, 2017]. Although the number of the applications is fewer than that of seismic velocity changes, seismic scattering property changes associated with volcanic activities or earthquakes have been detected by some previous studies using seismic interferometry [e.g., *Obermann et al.*, 2013; *Obermann et al.*, 2014; *Hillers et al.*, 2015; *Machacca et al.*, 2019]. Obermann et al. [2013a] succeeded in detecting a seismic scattering property change asso-

ciated with the October 2010 eruption at Piton de la Fournaise, Reunion Island from the decoherence (1−(coherence)) of seismic ambient noise CCFs. This is the first study that succeeded in detecting seismic scattering property changes based on seismic interferometry as far as we know. They succeeded in detecting large decoherences about one week before the eruption, and located the region of a large seismic scattering property change around the crater. They explained that magma intrusion to the crater caused such pronounced decoherences. Obermann et al. [2014] found seismic scattering property changes associated with the 2008 Wenchuan, China, earthquake. They used two period bands of 1-3 s and 12-20 s, and detected a coseismic change of decoherence in the 1-3 s period band around the earthquake epicenter. Such a coseismic change of decoherence can be directly related to severe damages at shallow depths caused by the earthquake. They also detected pronounced decoherences due to heavy rainfalls in the rainy season in 2007 and 2008 at the 1-3 s period band in the region different from the focal area. Table 1.1 is a summary of the previous studies that conducted estimations of seismic scattering property changes using seismic interferometry.

One of the problems on the imaging of seismic scattering property change is that the number of applications is much fewer than that of seismic velocity changes. In case of seismic velocities, the effect of external environmental perturbations to seismic velocity changes have been also discussed by many previous studies: rainfall [e.g., *Sens-Schönfelder and Wegler*, 2006; *Tsai*, 2011; *Wang et al.*, 2017], thermoelastic stress [e.g., *Meier et al.*, 2010; *Hillers et al.*, 2015], ocean loading [e.g., *Wang et al.*, 2017], snow loading [e.g., *Hatovec-Ellis et al.*, 2014], and atmospheric pressure [*Silver et al.*, 2007]. Evaluating such meteorological effects should be helpful also for the estimations of seismic scattering property changes. In terms of seismic scattering property, increasing the number of applications should be important, too.

Although locating change regions of seismic velocities and seismic scattering properties is important for the structural monitoring, a large number of seismic stations are necessary to estimate spatial distributions of medium changes. For example, Obermann et al. [2013] used 19 broadband seismic stations that are deployed in the area with dimensions of about 15 km in the east-west and 10 km in the north-south directions. Obermann et al. [2014] used 114 seismic stations in the target area (29° to 32°N and 100° to 105°E). Conducting such estimations are not easy in the regions where only a small number of stations are set up.

Linear least-squares inversions using sensitivity kernels have been applied in the previous studies which estimated spatial distributions of seismic scattering property changes.

Sensitivity kernels that are the spatial-weighting functions are used to locate the spatially localized seismic scattering property changes [e.g., *Mayor et al.*, 2014; *Margerin et al.*, 2016]. In the linear least-squares inversions, it is assumed that the scattering at a change region of seismic scattering property occurs only once. Therefore, the size of small cells is set to be smaller than the scattering mean free path so that the scattering occurs only once within each small cell. Accordingly, the number of model parameters in the linear least-squares inversion increases especially in a multiple scattering regime, because some previous studies reported that the scattering mean free path ranges from about a few hundred meters to a few kilometers at some active volcanoes. Therefore, imaging of scattering property changes in a multiple scattering regime is still challenging.

1.3 Objectives

We develop a self-contained approach to estimate space-time changes of seismic scattering properties only from seismic ambient noise CCFs without any natural earthquakes and active shots. Figure 1.2 represents the workflow of imaging of seismic scattering properties. In the current framework, scattering and intrinsic absorption parameters have been estimated by using the "active" approach, and the "passive" approach has been applied from the imaging phase. In contrast, our self-contained approach enables us to estimate scattering and intrinsic absorption parameters and conduct time-lapse imaging of seismic scattering properties by using only seismic ambient noise CCFs. In chapter 2, we develop a passive estimation method of scattering and intrinsic absorption parameters and validate it by comparing results from our passive method and that from active shot records at Sakurajima volcano, Japan. Moreover, we apply our passive method at the focal area of the Mw 6.9 2008 Iwate-Miyagi Nairiku earthquake and at Miyakejima volcano, Japan, and estimate scattering and intrinsic absorption parameters in these regions. In chapter 3, we estimate spatio-temporal changes of seismic scattering properties in northeast part of Japan from 2008 to 2012. The target area is in a weak scattering regime, and we can conduct linear least-squares inversions using sensitivity kernels. We estimate spatial distributions of seismic scattering property changes associated with the 2008 Iwate-Miyagi Nairiku earthquake and the 2011 Tohoku-Oki earthquake. Moreover, we conduct estimations in quiet periods when no significant earthquake was observed, and compare the results with other geophysical observations. In chapter 4, we apply sparse modeling to the imaging of seismic scattering property changes related to the 2008 Iwate-Miyagi Nairiku earthquake. We also validate the applicability of the sparse modeling by changing the number of seismic stations and their configurations. In chapter 5, we develop a method

for the time-lapse imaging of seismic scattering properties in a multiple scattering regime. Applying this method, we estimate the regions of seismic scattering property changes associated with 2015 dike intrusion event at Sakurajima volcano. In chapter 6, we discuss future developments of the space-time imaging of seismic scattering properties and structural monitoring with multi parameters. Chapter 7 contains general conclusions.

Table 1.1 Previous studies that estimated spatial distributions of seismic scattering property changes using seismic interferometry.

Event	Interpretation	Reference
The 2008 Mw 7.9 Wenchuan earthquake	serious damages at shallow region	Obermann et al. [2014]
Heavy rainfalls in monsoon seasons of 2007 and 2008	change in rive load or flooding	Obermann et al. [2014]
Eruption in Oct. 2010 at Piton de la Fournaise	magma intrusion	Obermann et al. [2013a]
geothermal reservoir stimulation in Switzerland	fluid injection	Hillers et al. [2015]
Eruption in Apr. 2014 at Ubinas volcano, Peru	material weakening	Machacca et al. [2019]

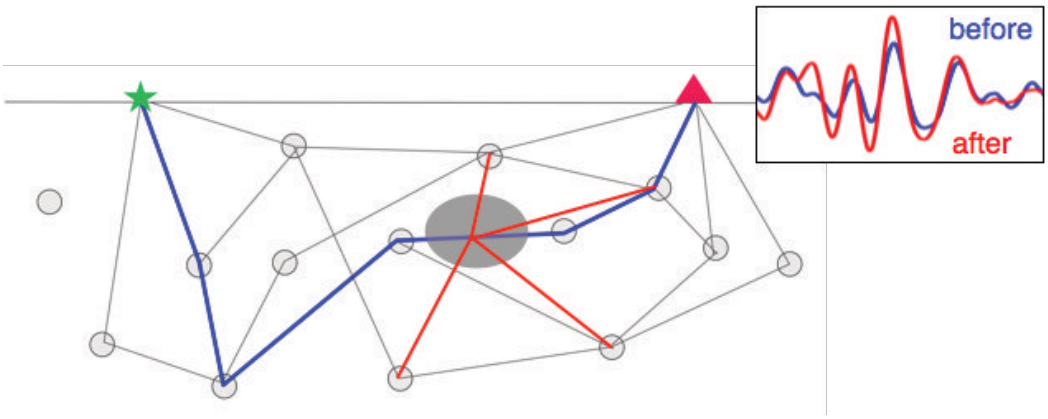

Figure 1.1 The schematic picture of mechanism of waveform changes. The grey ellipse represents the region of seismic scattering property change. Small gray circles are seismic scatterers. The top-right panel shows waveforms before (blue) and after (red) the change.

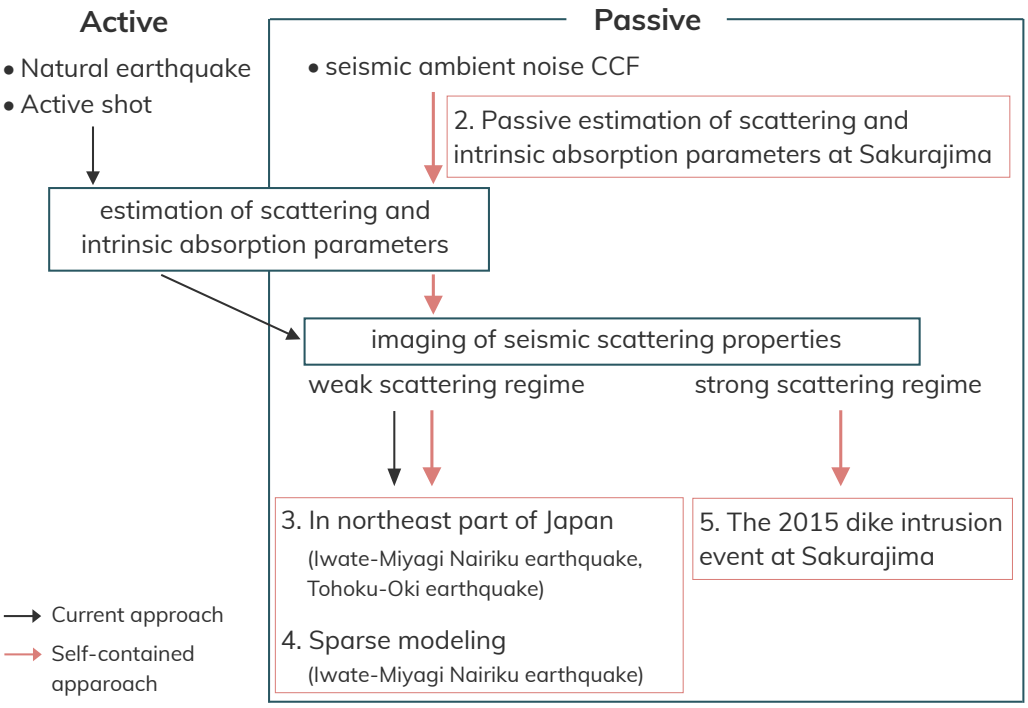

Figure 1.2 The workflow of imaging of seismic scattering properties. The black arrows represent the current imaging procedure. The pink arrows represent our new self-contained approach.

Chapter 2

Passive estimation of scattering and intrinsic absorption parameters using envelopes of seismic ambient noise CCFs

2.1 Introduction

As mentioned in chapter 1, estimating scattering and intrinsic absorption parameters from data of natural earthquakes or active shots is difficult to apply in regions with low seismicity or no active seismic experiment. Previous studies [e.g., *Stehly et al.*, 2006; *Tsai*, 2011; *Hanasoge*, 2013] have demonstrated that estimating attenuation from amplitudes of seismic ambient noise cross-correlation functions (CCFs) is generally difficult due to non-uniform source distributions. For example, Hanasoge [2013] calculated CCFs numerically for a ring of sources, uniform sources, and non-uniform sources, and showed that it is especially difficult to accurately extract attenuation information from ambient noise when the noise distribution is highly uneven. However, several previous studies have estimated values of attenuation using seismic ambient noise data by coping with the difficulty. Using coda wave part of seismic ambient noise auto-correlation functions, Wegler and Sens-Schönfelder [2007] estimated the coda attenuation factor. Liu et al. [2015] estimated total attenuation (the sum of scattering attenuation and intrinsic absorption) Q factors of Rayleigh waves, Q_R, using linear arrays in southern California. They estimated interstation Q_R values under stationary phase approximation [*Snieder*, 2004] and the Fresnel approximation from noise cross-spectrum functions. However, there is no previous study that separately estimated scattering and intrinsic absorption parameters from seismic ambient noise data as far as we know.

In this study, we develop a passive method for the estimation of scattering mean free path and intrinsic absorption parameter. We apply seismic interferometry using the temporal flattening technique [*Weaver*, 2011a] to seismic ambient noise data at Sakurajima volcano, at the southern rim of Aira caldera in the south of Kyushu, Japan. We estimate those parameters by modeling space-time distributions of envelopes of seismic ambient noise CCFs. Sakurajima is one of the most active volcanoes in Japan, and the number of

vulcanian-type eruptions, which occurred mainly at Showa crater, reached 835 in 2012, 883 in 2013 and 450 in 2014 [*Japan Meteorological Agency*, 2015]. To monitor the movement of subsurface magma at such a highly active volcano, active seismic experiments were conducted [*Tsutsui et al.*, 2016]. Hirose et al. [2017] already compared measurements of seismic wave speed changes inferred from seismic ambient noise CCFs and those from the active shot records, and showed they were consistent with each other. In this study, we validate the values of scattering and intrinsic absorption parameters from our passive method by comparing with those from the active shot records. This part was published as Hirose et al. [2019]. Moreover, we apply it to two other regions: the focal area of the 2008 Iwate-Miyagi Nairiku earthquake and Miyakejima volcano, Japan.

2.2 Development of a passive method by using data at Sakurajima

2.2.1 Data and method

At Sakurajima, three-component short-period seismometers with a natural frequency of 1 Hz have been deployed at 6 stations by Japan Meteorological Agency (Figure 2.1 (a)), and their signals are recorded at a sampling frequency of 100 Hz. We apply seismic interferometry to the seismic ambient noise data on the vertical, radial, and transverse components recorded in 2014.

Firstly, we filter the seismic ambient noise records at 0.5-1 Hz, 1-2 Hz, and 2-4 Hz bands by applying the 4th-order Butterworth filters. Transient signals are removed by identifying time windows with amplitudes twice larger than an hourly median amplitude level. Secondly, we apply the temporal flattening technique proposed by Weaver [2011a] to the seismic ambient noise data for reducing the effect of temporal fluctuations of noise levels. That is, we normalize each 1-hour long trace at each seismic station by a global noise amplitude level for that hour, where the global noise level is defined as the quadratic mean (square root of the mean square) of noise standard deviations at all stations. Note that one-bit normalization [e.g., *Larose et al.*, 2004] is not applied to the noise data, because relative amplitudes among the stations are not retained if such a strong non-linear operation is applied. In addition, we do not apply spectral whitening [e.g., *Shapiro et al.*, 2006; *Bensen et al.*, 2007] to avoid distorting amplitudes. Thirdly, we obtain daily CCFs (hereafter called DCCFs) on the vertical-vertical (ZZ), vertical-radial (ZR), vertical-transverse (ZT), radial-vertical (RZ), and transverse-vertical (TZ) components by calculating CCFs every 10 minutes and stacking each of them every day for 15 station pairs

from 6 stations. We average causal and acausal parts of each DCCF to reduce the effect of anisotropic noise source distributions [*Stehly et al.*, 2006]: We simply average causal and acausal parts of daily CCFs on the ZZ component and average causal part of ZR (ZT) and acausal part of RZ (TZ). Finally, these averaged DCCFs are stacked over one year to further reduce the effect of source anisotropy. Figure 2.1 (b) shows a record section of these one-year stacked CCFs (ZZ) at the 1-2 Hz band and particle motions on the radial-vertical plane in the time window around the direct Rayleigh wave arrival. The particle motions on the radial-vertical plane are retrograde, which means that Rayleigh waves are predominant on these stacked CCFs. Some wave packets with large amplitude are recorded before the direct Rayleigh wave arrivals. Most of the station pairs are opposite sides of the active crater, and those CCFs might be contaminated by volcanic tremors that occur beneath the crater. We compute mean squared (MS) envelopes by smoothing squared amplitudes with 4 s (0.5-1 Hz), 2 s (1-2 Hz), or 1 s (2-4 Hz) long time windows. They are normalized by the envelopes at 25 s in lapse time at the 0.5-1 Hz band and at 35 s at 1-2 Hz and 2-4 Hz bands for coda normalization. We use the sum of the MS envelopes over three components (ZZ, RZ & ZR, ZT & TZ) in the following analyses, and hereafter we simply call it observed energy density E_{obs}.

The best-fit values of the scattering mean free path ℓ and the intrinsic absorption parameter b ($b={}^{I}Q^{-1}\omega$) of Rayleigh wave are estimated by modeling the space-time distributions of energy densities with the 2-D radiative transfer theory. Here, ${}^{I}Q^{-1}$ is the reciprocal of the intrinsic Q factor and ω is the angular frequency. We use the 2-D radiative transfer equation to calculate synthesized energy densities [e.g., Shang and Gao, 1988; Sato, 1993]:

$$E_{syn}(r,t) = \frac{\mathrm{e}^{-ct\ell^{-1}}}{2\pi cr}\delta\left(t-\frac{r}{c}\right) + \frac{\mathrm{e}^{\ell^{-1}(\sqrt{c^2t^2-r^2}-ct)}}{2\pi\ell\sqrt{c^2t^2-r^2}}H\left(t-\frac{r}{c}\right). \tag{2.1}$$

Here c is the Rayleigh wave velocity (we fixed it to 1.15 km/s in the present study), r is the distance between source and receiver, ℓ is the scattering mean free path, and H is the Heaviside function. In this study, we also consider an intrinsic absorption parameter b. An energy density with the spatially homogeneous intrinsic absorption is obtained by multiplying e^{-bt} with the right-hand-side of equation (2.1). We calculate the sum of squared residuals (SSR) between observed and synthesized energy densities, E_{obs} and E_{syn}:

$$SSR = \sum_{i=1}^{6} \sum_{j=1}^{15} \Big(E_{obs}(t_i, j) - E_{syn}(t_i, j) \Big)^2. \tag{2.2}$$

Here, i is the number of time windows, and j is the number of station pairs. We use E_{obs} and E_{syn} in six time windows (8.5-9 s, 9-9.5 s, 9.5-10 s, 15-16 s, 17-18 s, and 21-22 s). To estimate both parameters, we use time windows from early, just after direct Rayleigh wave arrivals, (8.5-9 s, 9-9.5 s and 9.5-10 s) to late (15-16 s, 17-18 s, and 21-22 s) lapse times. The scattering mean free path is mainly determined by spatial gradients of the energy densities in the early lapse times which include direct and early coda parts of CCFs. The intrinsic absorption parameter controls how quickly energy levels decrease from the early to late lapse times. We determine the values of the parameters ℓ and b that minimize SSR by the grid search. The search range of ℓ is between 0.4-10 km with an increment of 0.4 km and that of b is between 0.00-0.40 s^{-1} with an increment of 0.01 s^{-1}.

2.2.2 Results

We estimate the scattering mean free path ℓ and intrinsic absorption parameter b of Rayleigh wave using 1-year stacked CCFs. These parameters are determined by modeling the space-time distributions of energy densities for all 15 station pairs with the 2-D radiative transfer theory. As shown in Figure 2.2, these 15 pairs have a wide range of azimuths, and hence the effect of anisotropic noise source distributions will be further reduced. Figures 2.3 (a), 2.4 (a), and 2.5 (a) show the results of the grid-search at 0.5-1 Hz, 1-2 Hz, and 2-4 Hz bands, respectively. The 95 % confidence intervals of the estimated ℓ and b values are 1.6-2.4 km and 0.04-0.06 s^{-1} at the 0.5-1 Hz, 1.6-2.0 km and 0.08-0.09 s^{-1} at the 1-2 Hz, and 1.6-3.2 km and 0.16-0.18 s^{-1} at the 2-4 Hz, respectively. Figures 2.3 (b), 2.4 (b), and 2.5 (b) show space-time distributions of observed energy densities (grey circles) at the 0.5-1 Hz, 1-2 Hz, and 2-4 Hz bands, respectively. The synthesized energy densities, shown by red solid curves, are calculated from the best-fit parameters at each frequency band. We also indicate the theoretical values without intrinsic absorption by dotted curves for comparison. As shown in Figure 2.3 (a) - Figure 2.5 (a), the value of b is determined more accurately than that of ℓ. To interpret this result, we compare space-time distributions of synthesized energy densities for three different values of scattering mean free paths and intrinsic absorption parameters. In Figure 2.6 (a), the synthesized energy densities from the best-fit value of the scattering mean free path at the 1-2 Hz band (1.6 km) are shown by red curves. Orange and green curves are synthesized energy densities

from $\ell = 0.53$ km (one-third of the best-fit value) and $\ell = 4.8$ km (three times of the best-fit value), respectively. As the scattering mean free path becomes small, the energy densities at large distance r become smaller due to multiple scattering. The spatial distribution of observed energy densities (grey circles) is a little bit fluctuated, and this leads to the weak constraint of the scattering mean free path. In Figure 2.6 (b), the synthesized energy densities from the best-fit value of intrinsic absorption parameter at the 1-2 Hz band (0.09 s^{-1}) are shown by red curves. Orange and green curves are synthesized energy densities from $b = 0.03$ s^{-1} (one-third of the best-fit value) and $b = 0.27$ s^{-1} (three times of the best-fit value), respectively. Values of b control decay rates of the observed and synthesized energy densities with lapse times. Accordingly, levels of the observed and synthesized energy densities at respective lapse times are found to be affected by the intrinsic absorption parameter. This is enhanced especially at late lapse times. Therefore, intrinsic absorption parameter is strongly constrained by the level of energy densities especially at late lapse times.

2.2.3 Validation of the method: comparison with the results using active shot records

To validate the results from our passive method, we compare them with those estimated from active shot records at Sakurajima. We use seismograms of the shot UR2E in 2013 (see Figure 2.1 (a)) recorded at 6 JMA stations. The source depth of the active shot is around 60 m, and hence we may compare the results of our passive method and those from the active shot. Velocity seismograms and MS envelopes at the 1-2 Hz band of the active shot are shown in Figures 2.7 (a) and (b), respectively. Seismograms have high signal to noise ratios even at seismic stations far from the shot point because of the dynamite charge of 200 kg. Particle motions on the radial-vertical plane just after the direct Rayleigh wave arrival are retrograde, which means that Rayleigh waves are predominant on active shot seismograms. Figures 2.7 (c) and (d) show the distribution of SSRs at the 1-2 Hz band and space-time distributions of energy densities, respectively. Here, we use E_{obs} and E_{syn} in the same six time windows as the estimations using seismic ambient noise CCFs. The 95 % confidence intervals were estimated to be 1.2 km and 0.09-0.11 s^{-1} at the 1-2 Hz band and 1.6-2.0 km and 0.14-0.16 s^{-1} at the 2-4 Hz band, respectively. The values estimated by our passive method and those estimated from active shot records are almost consistent with each other.

Our results suggest that we can estimate values of ℓ and b without active shot records or natural earthquakes. In our passive method, those parameters are estimated even at

the 0.5-1 Hz. On the other hand, the signal to noise level of active shot data is too low to measure ℓ and b at such a low-frequency range. Since frequency bands below 1 Hz are widely used in seismic interferometry analyses, our passive method may increase the applicability of the time-lapse imaging of seismic velocity and seismic scattering property using seismic ambient noise CCFs and sensitivity kernels.

2.2.4 Effects of spectral whitening and one-bit normalization

Spectral whitening technique and one-bit normalization have been widely used in seismic interferometry analyses for suppressing earthquakes and persistent monochromatic noise sources on seismic ambient noise CCFs. Here, we estimate values of ℓ and b using one-bit normalization and/or spectral whitening. Table 2.1 summarizes the results for four different procedures using (1) temporal flattening, (2) spectral whitening and temporal flattening, (3) one-bit normalization, and (4) spectral whitening and one-bit normalization. It is not possible to make a stable measurement of ℓ at the 0.5-1 Hz band in the procedure (4). The values of b from procedures (3) and (4) are significantly smaller than those from procedures (1) and (2) for all frequency bands (Figure 2.8).

Figure 2.9 (a) shows MS envelopes of CCFs for station pairs of V.SKRB-V.SKA2, V.SFT2-V.SKRB, and V.SKA2-V.SKD2. At the 0.5-1 Hz band, MS envelopes from spectral whitening and one-bit normalization (pink lines) for station pairs of V.SKRB-V.SKA2 and V.SFT2-V.SKRB are significant smaller than those from other three procedures. Figure 2.9 (b) shows space-time distributions of energy densities from the temporal flattening (blue circles) or from spectral whitening and one-bit normalization (pink circles) at the 0.5-1 Hz band. In the case of using spectral whitening and one-bit normalization, energy densities for station pairs with short inter-station distances are smaller than those of the temporal flattening case in early lapse times. Accordingly, the distribution of energy densities is almost spatially uniform not only in large lapse times but also in early lapse times. Such small spatial gradient of energy densities should lead the overestimation of ℓ. In addition, small energy densities for the station pairs with short inter-station distances in early lapse times cause a slow decrease of energy densities with time and result in the underestimation of b (see also Figure 2.6). In the temporal flattening, ambient noise amplitudes at each seismic station are normalized by global noise levels: relative amplitudes among different stations are retained. On the other hand, spectral whitening technique and one-bit normalization may introduce errors in relative amplitudes. This can explain the unreliable estimation results. Underestimations of attenuations have been also reported by numerical simulations [*Weaver*, 2011a] and real data analyses [*Zhang and*

Yang, 2013].

2.2.5 Estimation results from four different three-month periods data

Some previous studies pointed out that anisotropic noise source distributions can bias attenuation estimates from noise [e.g., *Tsai*, 2011; *Hanasoge*, 2013]. Therefore, we also estimate ℓ and b from CCFs stacked for four different three-month periods (Jan.-Apr., Apr.-Jun., Jul.-Sep., and Oct.-Dec. in 2014). Figure 2.8 shows the estimated values of these parameters for the four periods. The blue solid lines represent the results from temporal flattening. The best-fit values are stable in time: scattering mean free paths for four periods are estimated to be 2.0 km at 0.5-1 Hz band, 1.6 km-2.0 km at 1-2 Hz, and 2-4 Hz bands, respectively, and intrinsic absorption parameters are 0.04-0.05 s^{-1} at the 0.5-1 Hz band, 0.08-0.10 s^{-1} at the 1-2 Hz band, and 0.15-0.16 s^{-1} at the 2-4 Hz bands, respectively. These results indicate that our results are not significantly affected by anisotropy that would show up as temporal fluctuations of our estimates due to changes in the source distribution.

As mentioned in the Data and method section, temporal flattening effectively reduces temporal fluctuations of spatial variations of seismic ambient noise amplitudes, and this enables us to estimate scattering and intrinsic absorption parameters stably. Figure 2.10 shows temporal changes of hourly standard deviations of seismic ambient noise amplitudes at Sakurajima in 2014. Temporal fluctuations of spatial variations of ambient seismic noise amplitudes may hamper the stable estimations of parameters. We can confirm that the temporal fluctuations are significantly smaller in the case of temporal flattening than the other cases, which leads to the stable estimations of parameters.

2.3 Application of the method to two other regions

2.3.1 Application to the focal area of the Iwate-Miyagi Nairiku earthquake

We apply the passive method to the focal area of the 2008 Iwate-Miyagi Nairiku earthquake. The green squares in Figure 2.11 (a) represent 17 Hi-net stations maintained by the National Research Institute for Earth Science and Disaster Resilience (NIED). A three-component short-period seismometer with a natural frequency of 1 Hz is installed at each station. All the seismograms are recorded with a sampling frequency of 100 Hz. We apply the passive method to seismic ambient noise data at the 0.5-1 Hz band during the

year of 2007. We compute CCFs every 10 minutes and calculate DCCFs by stacking these 10-min CCFs every day for 136 pairs from the 17 stations. The 1-year-stacked CCFs are used to estimate scattering and intrinsic absorption parameters. Figure 2.11 (b) shows the result of grid-search. The search range of ℓ is between 5-200 km with an increment of 5 km, and that of b is between 0.00-0.10 s^{-1} with an increment of 0.01 s^{-1}. The best-fit value of ℓ is estimated to be 30 km and that of b was estimated to be 0.02 s^{-1}. Figure 2.11 (c) shows space-time distributions of observed (gray circles) and synthesized (red solid lines) energy densities. The scattering mean free path in the focal area of the Iwate-Miyagi Nairiku earthquake is 1 order larger than those at Sakurajima volcano. These estimated values are used in chapter 4.

2.3.2 Application to Miyakejima

We apply the passive method to Miyakejima volcano, Japan. The green and blue squares in Figure 2.12 (a) represent 5 seismometers maintained by JMA or NIED. A three-component short-period seismometer with a natural frequency of 1 Hz is installed at each station. All the seismograms are recorded with a sampling frequency of 100 Hz. We apply the passive method to seismic ambient noise data between Jan. 1 and Mar. 31 in 2012 at the 1-2 Hz and 2-4 Hz bands. We compute CCFs every 10 minutes and calculate DCCFs by stacking these 10-min CCFs every day for 10 pairs from the 5 stations. The 3-months-stacked CCFs are used to estimate scattering and intrinsic absorption parameters. Figures 2.12 (b) and (d) show the results of grid-search at the 1-2 Hz and 2-4 Hz bands, respectively. The search range of ℓ is between 0.4-10 km with an increment of 0.4 km and that of b is between 0.00-0.30 s^{-1} with an increment of 0.01 s^{-1}. The best-fit parameters are estimated to be 1.6 km and 0.12 s^{-1} at the 1-2 Hz band and 2.0 km and 0.16 s^{-1} at the 2-4 Hz band, respectively. Figures 2.12 (c) and (e) show space-time distributions of observed (gray circles) and synthesized (red solid lines) energy densities. The scattering mean free paths at Miyakejima are almost the same as those at Sakurajima.

2.4 Discussions

2.4.1 Compiling the two parameters estimated at different regions

As mentioned in chapter 1, scattering and intrinsic absorption parameters have been estimated by many previous studies using the data of natural earthquakes or active shot records. Figure 2.13 shows the estimated values of scattering and intrinsic attenuation factors at each frequency in various regions. Q_{sc}^{-1} is the scattering attenuation Q factor

($Q_{sc}^{-1} = vg_0/\omega$) and Q_I^{-1} is that of the intrinsic attenuation ($Q_I^{-1} = b/\omega$). Here, v is the wave speed and ω is the angular frequency. The gray shaded areas represent value ranges of Q_{sc}^{-1} and Q_I^{-1} of S-waves estimated by previous studies using MLTWA, and their study areas are non-volcanic regions [*Sato et al.*, 2012]. The red, pink, and orange squares on each panel represent the our results of Rayleigh waves at Sakurajima, the focal area of the Iwate-Miyagi Nairiku earthqauke, and Miyakejima. The blue and green squares represent the results at Asama volcano, Japan [*Yamamoto and Sato*, 2010] and at Stromboli volcano, Italy [*Prudencio et al.*, 2015], respectively. Their studies used active shot records for estimations. In terms of intrinsic attenuation, we cannot see such a significant difference between volcanic and non-volcanic areas. The estimated Q_{sc}^{-1} values at Sakurajima and Miyakejima are 2-3 orders larger than those in non-volcanic regions. These results are almost consistent with those at Asama and Stromboli suggesting that medium heterogeneities are strong at shallow parts of these active volcanoes. The estimated Q_{sc}^{-1} value in the focal area of the Iwate-Miyagi Nairiku earthquake is a bit larger than most of those values in other non-volcanic regions. In MLTWA, natural earthquakes which occurred at depths between several kilometers and several tens of kilometers are used. In contrast, the sources are located at/near the ground surface in the case of our passive method, and this means that estimated attenuation factors strongly reflect the medium heterogeneities at shallow regions. Thus, the estimated Q_{sc}^{-1} value from the passive method can be larger than those from MLTWA.

One of the advantages of our passive method is that the sources are always located at/near the ground surface. This can allow us to compare estimated values between various regions and measure temporal changes of attenuations at a target area. In the case of using natural earthquakes, a spatial bias of hypocenters can affect estimation results.

2.4.2 Note of our passive method

We also estimate scattering and intrinsic absorption parameters in the focal area of the Iwate-Miyagi Nairiku earthquake at the 0.125-0.25 and 0.25-0.5 Hz bands. Figure 2.14 shows the results of the grid-search in these frequency bands. The intrinsic absorption parameter are estimated to be 0.03-0.04 s^{-1} at the 0.125-0.25 Hz band and 0.02-0.03 s^{-1} at the 0.25-0.5 Hz band, respectively. In contrast, scattering mean free paths are not constrained in these frequency bands. As mentioned in the Data and method section, the scattering mean free path is mainly determined by spatial gradients of the energy densities in early lapse times which include direct and early coda parts of CCFs (see also Figure 2.6). In the case of the focal area of the Iwate-Miyagi Nairiku earthquake, the scattering

mean free paths at the 0.125-0.25 and 0.25-0.5 Hz bands might be longer than the size of the seismic network used in our estimations. This means that the spatial gradients of the energy densities can be almost flat within the seismic network, and this may lead to the weak constraint of the scattering mean free paths. Accordingly it is necessary to use a larger seismic network in such a weak scattering regime.

2.5 Conclusion

We have proposed a passive method to estimate scattering and intrinsic absorption parameters by using envelopes of seismic ambient noise CCFs. Applying the method to seismic ambient noise data at Sakurajima volcano, Japan, we estimated scattering mean free paths and intrinsic absorption parameters to be 1.6-2.4 km and 0.04-0.06 s^{-1} at 0.5-1 Hz, 1.6-2.0 km and 0.08-0.09 s^{-1} at 1-2 Hz, and 1.6-3.2 km and 0.16-0.18 s^{-1} at 2-4 Hz, respectively. The validity of these results was confirmed at the 1-2 Hz and 2-4 Hz bands by comparing with these parameters estimated from active shot records at Sakurajima. We confirmed that temporal flattening technique gives us better estimation results compared to the one-bit normalization and spectral whitening. This is because ambient noise amplitudes at each seismic station are normalized by global noise levels on the temporal flattening technique: the relative amplitudes among different stations are retained.

We also applied the passive method to the focal area of the 2008 Iwate-Miyagi Nairiku earthquake and Miyakejima volcano, Japan. The scattering mean free path and intrinsic absorption parameter in the focal area of the Iwate-Miyagi Nairiku earthquake were estimated to be 30 km and 0.02 s^{-1} at the 0.5-1 Hz band. The scattering mean free paths were not constrained at the 0.125-0.25 Hz and 0.25-0.5 Hz bands. In the case of Miyakejima, the scattering mean free paths were estimated to be 1.6 km at the 1-2 Hz band and 2.0 km at the 2-4 Hz band, respectively. The intrinsic absorption parameters were estimated to be 0.12 s^{-1} at the 1-2 Hz band and 0.16 s^{-1} at the 2-4 Hz band, respectively. The estimated scattering mean free paths at Sakurajima and Miyakejima were 2-3 orders larger than those in non-volcanic regions. On the other hand, there are no significant differences between volcanic and non-volcanic areas in the case of the intrinsic absorption parameters.

Our passive method is applicable even in regions of low seismicity and no active seismic experiment data, and hence, this method can be widely used to measure the degree of medium heterogeneities in various regions. Moreover, it will improve the applicability of the time-lapse imaging using sensitivity kernels.

Table 2.1 Best-fit values of scattering mean free path ℓ (km) and intrinsic absorption parameter b (s^{-1}) from four different procedures at 0.5-1 Hz, 1-2 Hz, and 2-4 Hz bands. Value ranges in brackets indicate 95 % confidence intervals.

Frequency band	Temporal flattening	Temporal flattening + Spectral whitening	One-bit normalization	One-bit normalization + Spectral whitening
0.5-1 Hz	2.0 km (1.6-2.4 km) 0.05 s^{-1} (0.04-0.06 s^{-1})	2.4 km (2.0-2.8 km) 0.05 s^{-1} (0.04-0.05 s^{-1})	3.6 km (2.4-6.0 km) 0.03 s^{-1} (0.02-0.04 s^{-1})	10.0 km (4.8-10.0 km) 0.00 s^{-1} (0.01-0.01 s^{-1})
1-2 Hz	1.6 km (1.6-2.0 km) 0.09 s^{-1} (0.08-0.09 s^{-1})	2.0 km (1.6-3.2 km) 0.10 s^{-1} (0.10-0.11 s^{-1})	1.6 km (1.6-2.4 km) 0.07 s^{-1} (0.07-0.08 s^{-1})	1.6 km (1.6-2.0 km) 0.10 s^{-1} (0.10 s^{-1})
2-4 Hz	2.0 km (1.6-3.2 km) 0.17 s^{-1} (0.16-0.18 s^{-1})	2.0 km (1.6-2.4 km) 0.16 s^{-1} (0.16 s^{-1})	2.8 km (2.0-4.4 km) 0.13 s^{-1} (0.13-0.14 s^{-1})	2.0 km (2.0-2.8 km) 0.14 s^{-1} (0.14-0.15 s^{-1})

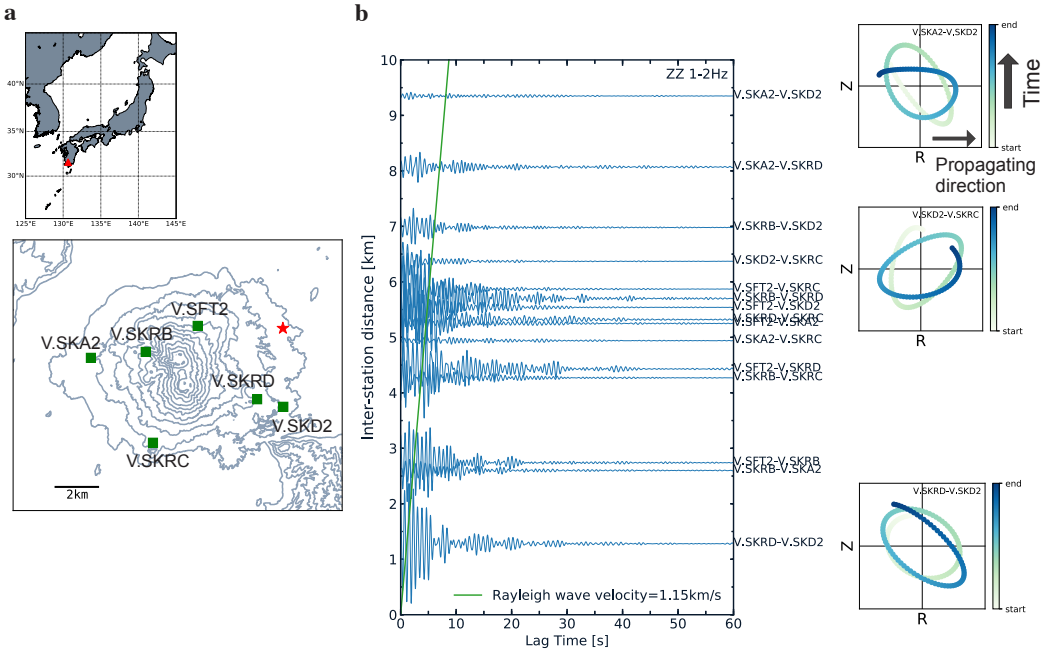

Figure 2.1 (a) Spatial distribution of seismometers (green squares) at Sakurajima volcano located in Kyushu island, Southwestern Japan (red triangle in the upper left panel). Gray contour lines show the topography of Sakurajima. The red star indicates the shot point of the active seismic experiment. (b) Record section of stacked CCFs on the vertical-vertical component at 1-2 Hz. Those CCFs are calculated using seismic ambient noise data in 2014. The green line indicates the arrival times of the direct Rayleigh wave whose velocity is assumed to be 1.15 km/s. Right 3 panels are the examples of particle motions on the radial-vertical plane around the direct Rayleigh wave arrivals for 3 station pairs.

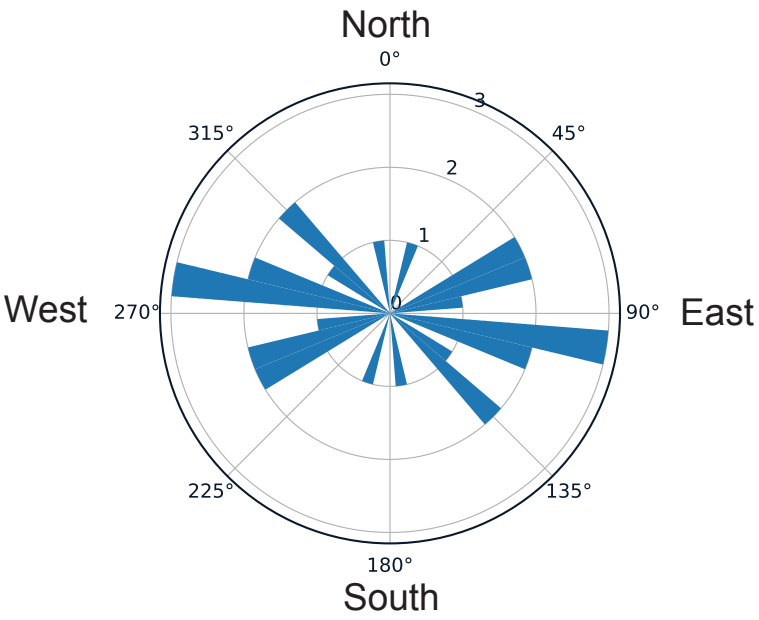

Figure 2.2 A histogram of azimuths for station pairs at Sakurajima volcano.

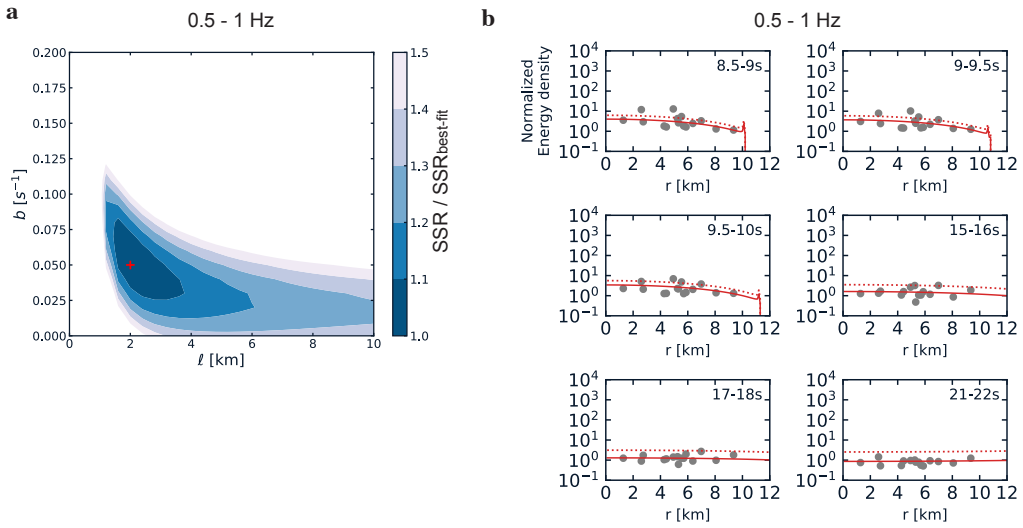

Figure 2.3 (a) Distribution of the sum of squared residuals (SSR) between observed and synthesized energy densities at the 0.5-1 Hz. Horizontal and vertical axes are the scattering mean free path ℓ and intrinsic absorption parameter b. The red cross indicates the point of the minimum SSR (best-fit), and SSRs on each grid point are normalized by the minimum one. (b) Spatial distributions of energy densities for 6 time windows in the same frequency band and period of time. Grey circles are observations which are calculated using envelopes of seismic ambient noise CCFs. The red solid curves are synthesized ones which are calculated by using 2-D radiative transfer equation and the best-fit values of the scattering mean free path and intrinsic absorption parameter. The red dotted curves are synthesized ones without intrinsic absorption.

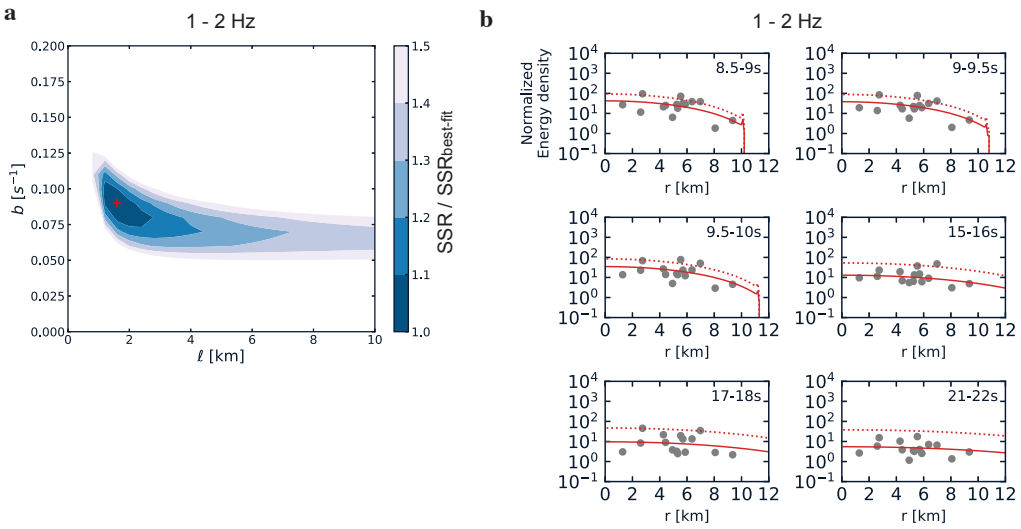

Figure 2.4 Similar to Figure 2.3 but at the 1-2 Hz band.

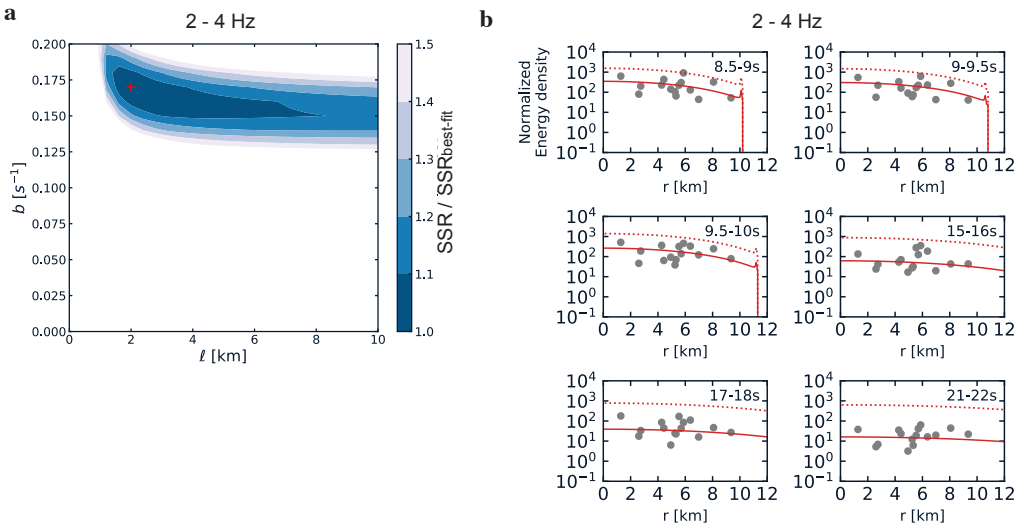

Figure 2.5 Similar to Figure 2.3 but at the 2-4 Hz band.

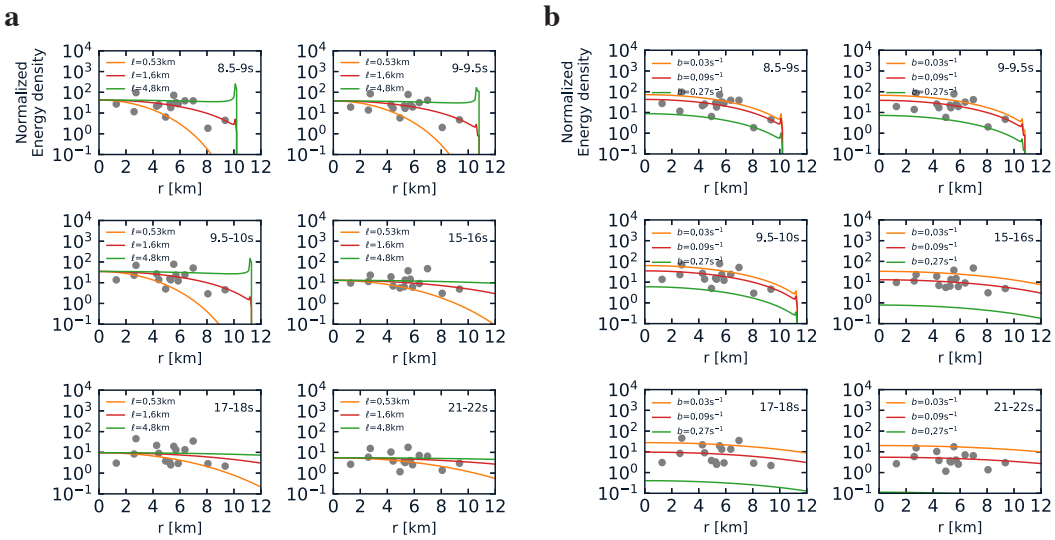

Figure 2.6 Comparison of spatial distributions of observed and synthesized energy densities for 6 time windows. Grey circles are observations which are calculated using envelopes of seismic ambient noise CCFs at the 1-2 Hz band, and three curves are synthesized ones. (a) Synthesized energy densities for three different scattering mean free paths are shown by orange, red, and green curves. The value of intrinsic absorption parameter is the same (0.09 s^{-1}) for all three curves. (b) Synthesized ones for three different intrinsic absorption parameters are shown by orange, red, and green curves. The scattering mean free path is the same (1.6 km) for all three curves.

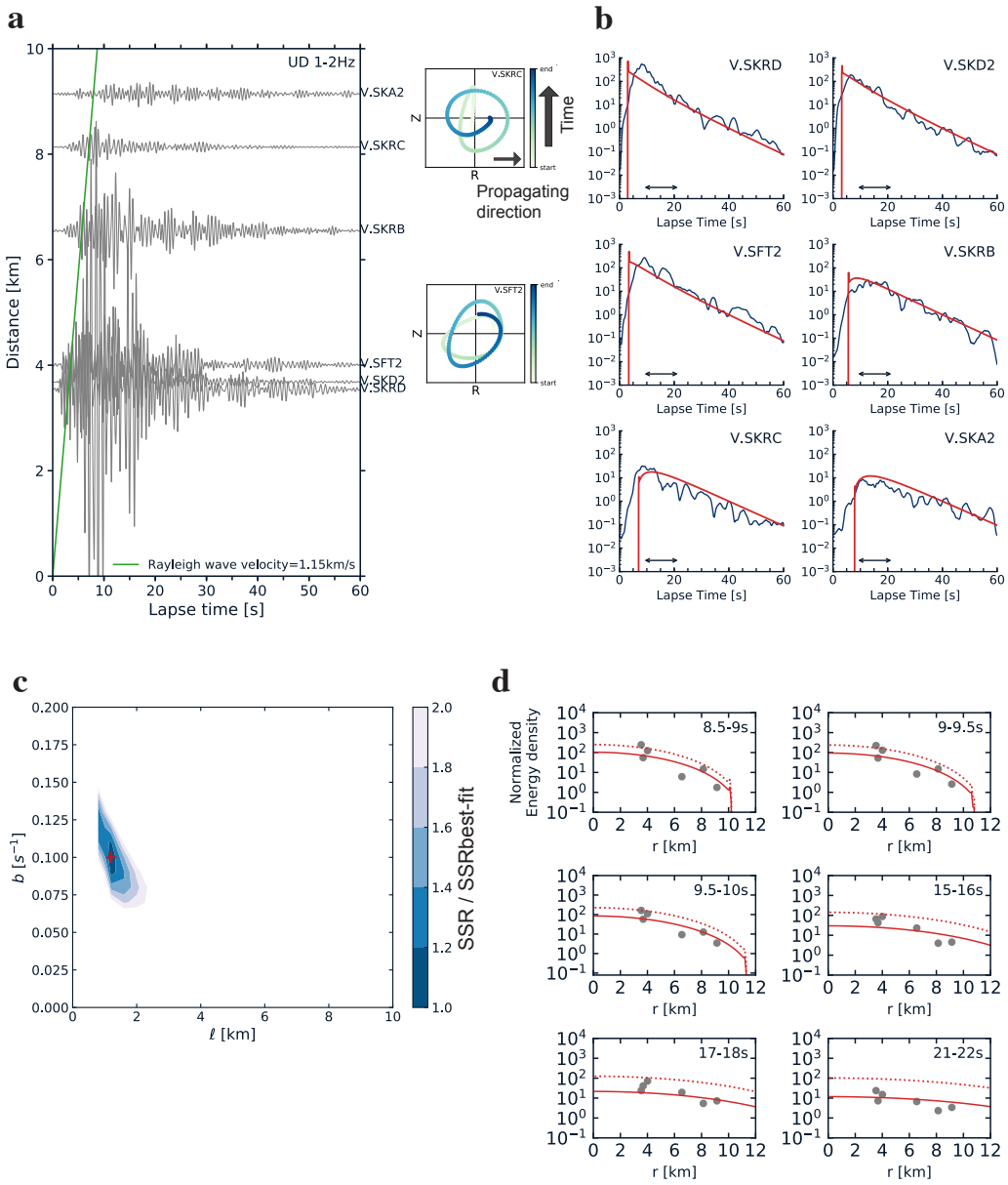

Figure 2.7 (a) Velocity seismograms from shot UR2E in 2013 for each seismic station on the vertical component at the 1-2 Hz band. Green straight line indicates direct Rayleigh wave arrival times. Two small panels right to the seismograms indicate particle motions on Radial-Vertical plane in the time windows around the direct Rayleigh wave arrival. (b) MS envelopes of active shot seismograms which are summed over the three components (blue lines). Red lines are the best-fit envelopes. The range of lapse time used in our study is shown by black arrows. (c) Distributions of SSRs in the grid-search at the 1-2 Hz band. (d) Spatio-temporal distributions of observed energy densities at the 1-2 Hz band.

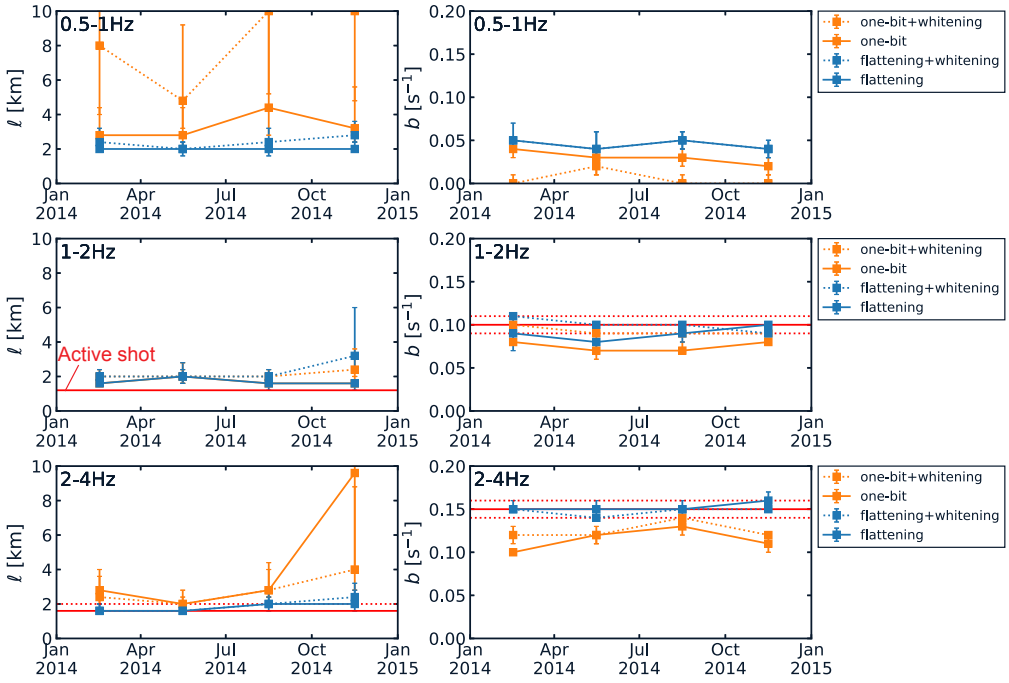

Figure 2.8 Estimated values of the scattering mean free paths and intrinsic absorption parameters by 4 different data analysis procedures in 4 different time periods. Blue and orange squares and lines indicate that temporal flattening technique or one-bit normalization is applied, respectively. Dash lines indicate that spectral whitening is applied in addition to these time-domain-normalizations. Error bars correspond to 95 % confidence intervals. Red solid and dotted lines indicate the best-fit values and those of 95 % confidence intervals estimated by using active shot records.

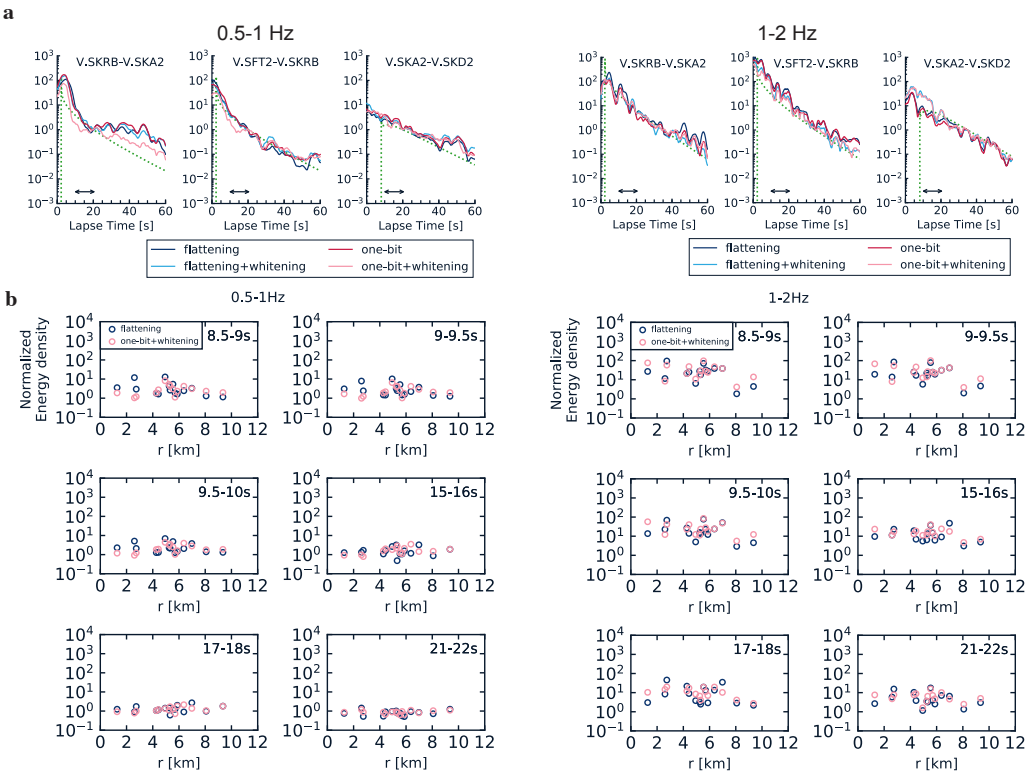

Figure 2.9 (a) Examples of MS envelopes of CCFs for four different procedures at the 0.5-1 Hz (left three panels) and the 1-2 Hz (right three panels) bands. Green dotted lines are the best-fit envelopes from the temporal flattening technique. (b) Spatial distributions of energy densities for 6 time windows in cases of using temporal flattening or spectral whitening and one-bit normalization at the 0.5-1 Hz and 1-2 Hz bands.

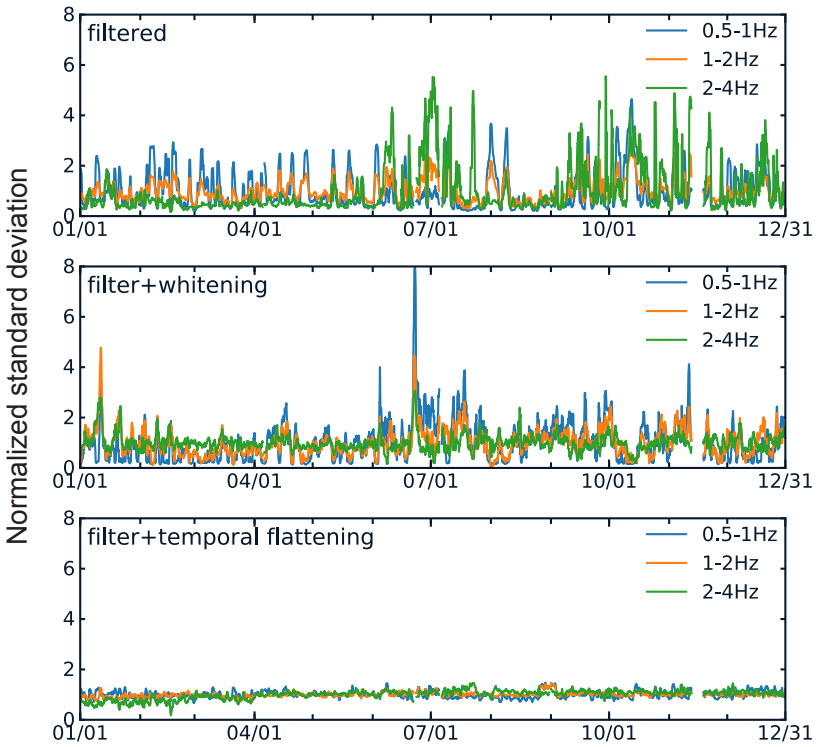

Figure 2.10 Time fluctuations of standard deviations of seismic ambient noise amplitudes on the vertical component at 6 seismic stations in 2014. These standard deviations are normalized by their annual means and a moving average with a time window length of 1 day is applied. Top panel shows time fluctuations after applying band-pass filters. Middle and bottom panels show those of after applying spectral whitening and temporal flattening to band-pass filtered seismic ambient noise data, respectively.

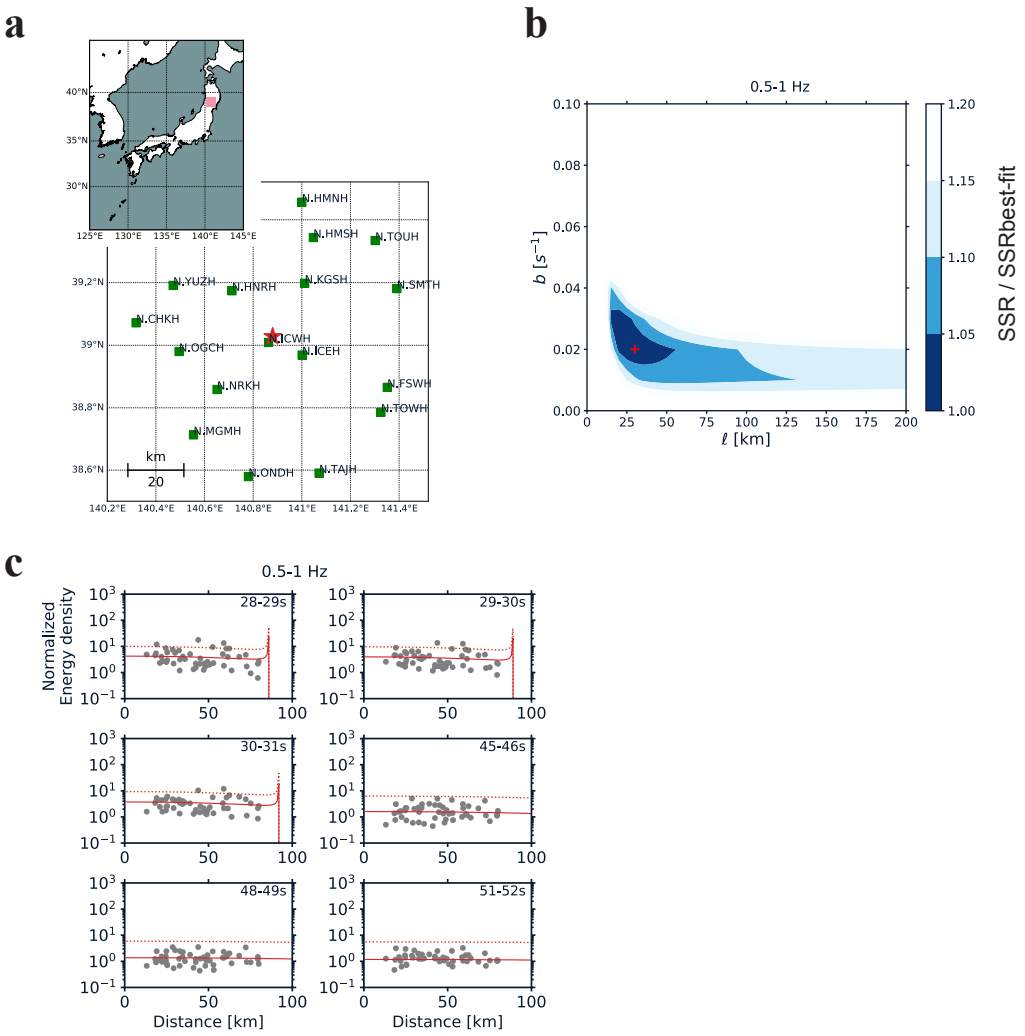

Figure 2.11 (a) Locations of 17 Hi-net stations (green squares) and the epicenter of the 2008 Iwate-Miyagi Nairiku earthquake (red star). (b) Distribution of sum of squared residuals (SSR) between the observed and synthesized energy densities at the 0.5-1 Hz band. (c) Spatial distributions of energy densities for 6 time windows.

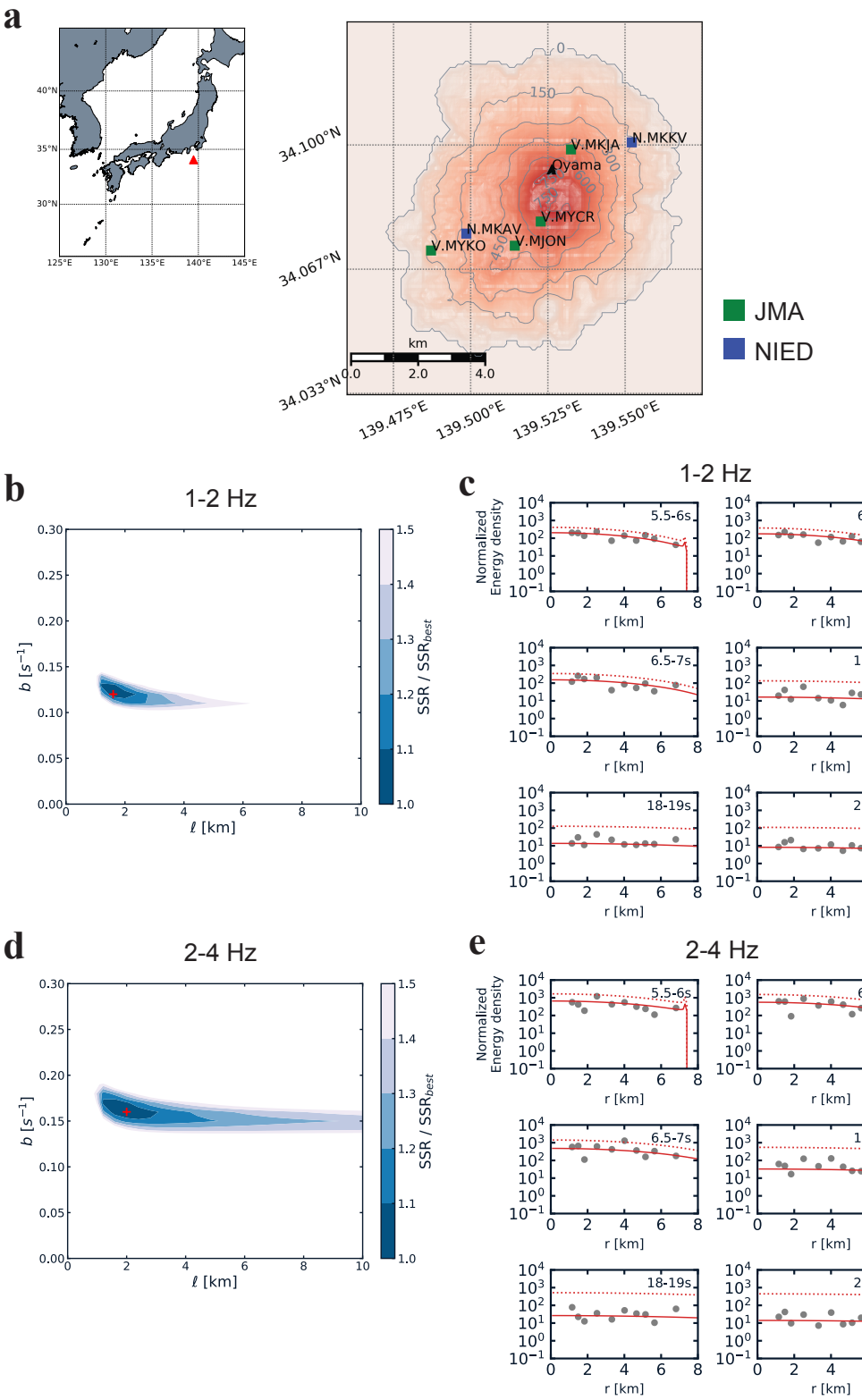

Figure 2.12 (a) Locations of 5 seismic stations (green and blue squares). (b) Distribution of sum of squared residuals (SSR) between the observed and synthesized energy densities at the 1-2 Hz band. (c) Spatial distributions of energy densities for 6 time windows at the 1-2 Hz band. (d) Similar to (b) but at the 2-4 Hz band. (e) Similar to (c) but at the 2-4 Hz band.

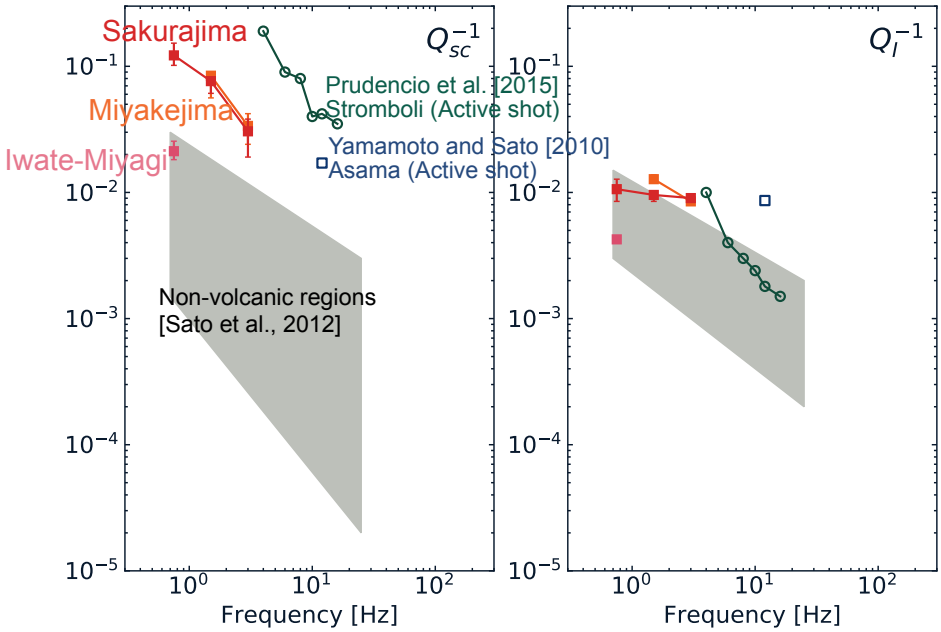

Figure 2.13 Scattering and intrinsic attenuation factors Q_{sc}^{-1} (left) and Q_I^{-1} (right) of S-waves in various regions. The gray shaded areas represent value ranges of Q_{sc}^{-1} and Q_I^{-1} in non-volcanic regions [*Sato et al.*, 2012]. Blue squares and green circles represent estimated values at Asama [*Yamamoto and Sato*, 2010] and Stromboli [*Prudencio et al.*, 2015], respectively. Note that our results at Sakurajima (red squares and lines), Iwate-Miyagi (pink), and Miyakejima (orange) are those attenuation factors of Rayleigh waves.

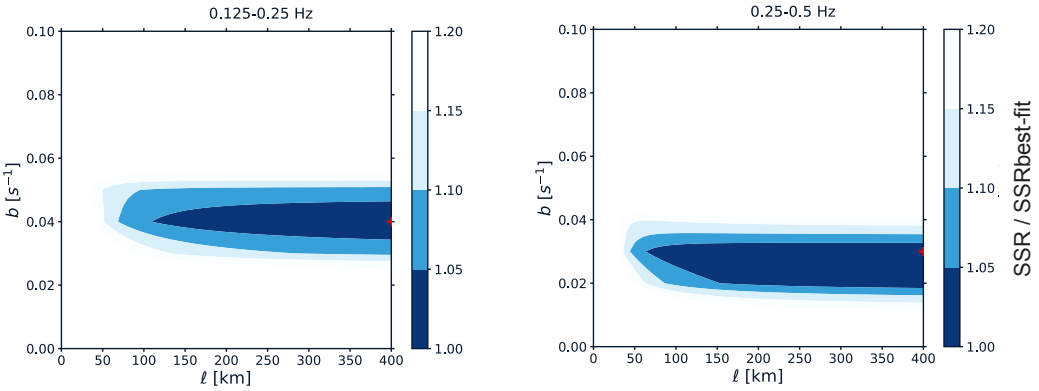

Figure 2.14 Estimation results of scattering and intrinsic absorption parameters around the focal area of the Iwate-Miyagi Nairiku earthquake at the 0.125-0.25 Hz and 0.25-0.5 Hz bands. Each panel represents the distribution of SSRs between the observed and synthesized energy densities at the 0.125-0.25 Hz (left) and 0.25-0.5 Hz (right) bands, respectively.

Chapter 3

Time lapse imaging of seismic scattering properties in a weak scattering regime: Analysis for the northeast part of Japan during 2008-2012

3.1 Introduction

In recent years, spatial distributions of seismic scattering property changes associated with volcanic activities and earthquakes have been estimated using seismic ambient noise CCFs and linear least-squares inversions [e.g., *Obermann et al.*, 2013; *Obermann et al.*, 2014; *Hillers et al.*, 2015; *Machacca et al.*, 2019]. Obermann et al. [2013] succeeded in detecting changes in seismic scattering property around the crater of the October 2010 eruption at Piton de la Fournaise, Reunion Island. Obermann et al. [2014] conducted a time-lapse imaging of seismic scattering properties during 2 years around the focal area of the 2008 Wenchuan, China, earthquake. They detected changes of seismic scattering property associated with the earthquake and monsoon seasons by using seismic ambient noise CCFs at the 1-3 s period band. They interpreted that the coseismic changes can be directly related to severe damages at shallow depths caused by the mainshock and many aftershocks. They also attributed seismic scattering property changes in the monsoon seasons to local effects around the river (change in river load or flooding). Although seismic interferometry is useful for the time-lapse imaging of seismic scattering properties, the number of the applications is only a few yet.

The 2008 Mw 6.9 Iwate-Miyagi Nairiku earthquake occurred on 14 June 2008 (Japan Standard Time) in the central part of Tohoku region, northeast Japan. The depth of the hypocenter was approximately 6 km and the focal mechanism of the main shock was a reverse fault type. The hypocenter of this earthquake is located among the dense seismic network, Hi-net, which is operated by the National Research Institute for Earth Science and Disaster Resilience (NIED). Strong ground motions were recorded by KiK-net accelerometers that were deployed near the epicenter: the peak ground acceleration

(PGA) reached approximately 4,000 gal [*Aoi et al.*, 2008]. Spatial distributions of seismic velocity changes have been estimated by some previous studies using seismic interferometry [e.g., *Takagi et al.*, 2012; *Hobiger et al.*, 2012; *Hobiger et al.*, 2014; *Wang et al.*, 2017]. However, there is no previous study that estimated the spatial distribution of seismic scattering property changes associated with this earthquake. The 2011 Mw 9.0 Tohoku-Oki earthquake occurred on 11 March 2011 (Japan Standard Time) off the east coast of Japan. The depth of the hypocenter was approximately 24 km and the focal mechanism of the main shock was a thrust type. Many previous studies reported significant seismic velocity changes associated with the earthquake [e.g., *Nakata and Snieder*, 2011; *Takagi and Okada*, 2012; *Brenguier et al.*, 2014; *Nakahara*, 2015; *Sawazaki et al.*, 2015]. However, there is no previous study that estimated the spatial distribution of seismic scattering property changes in the case of the Tohoku-Oki earthquake, too.

We estimate spatio-temporal changes of seismic scattering properties in the northeast part of Japan (Tohoku region) from 2008 to 2012 by computing decoherences (waveform changes) of seismic ambient noise CCFs. Dense and wide distribution of the high-sensitivity seismograph network (Hi-net) allows us to conduct time-lapse imaging of seismic scattering property in a wide area of the northeast part of Japan.

3.2 Data and method

3.2.1 Data and calculation procedure of seismic ambient noise CCFs

We use seismograms recorded at 121 Hi-net stations that are maintained by NIED (green squares in Figure 3.1 (a)). A three-component short-period seismometer with a natural frequency of 1 Hz is installed at each station. All the seismograms are recorded with a sampling frequency of 100 Hz. We apply seismic interferometry to seismic ambient noise data on the vertical component during the periods from 2008 to 2012. To improve the temporal stability of noise records before correlation, we apply one-bit normalization [e.g., *Larose et al.*, 2004], which removes some irregular events and preserves the phase of the signal during this period. In the frequency domain, spectral whitening in the band from 0.08 Hz to 2.0 Hz can decrease the influence of persistent monochromatic noise sources [e.g, *Shapiro et al.*, 2006; *Bensen et al.*, 2007]. We compute CCFs every hour at 0.125-1 Hz band and calculate daily CCFs (hereafter called DCCFs) by stacking these hourly CCFs every day for 7260 station pairs from 121 stations. The obtained DCCFs are considered to be Green's functions recorded at one of a station pair from a virtual source at the other

station of the pair. Figure 3.1 (b) is a record section of CCFs at 0.125-1 Hz band. These CCFs are computed by stacking DCCFs over 5 years. Rayleigh waves which propagate with a velocity of about 3 km/s are clearly retrieved. In this study, we use these 5-years-stacked CCFs as reference CCFs (hereafter called RCCFs). Figure 3.2 shows temporal changes of daily coherence values over 5 years for 2 station pairs (N.HMNH-N.ONDH and N.ADTH-N.TSTH). Each blue bar represents a coherence between a RCCF and a 60-days stacked CCF. The significant decoherences were detected associated with the 2008 Iwate-Miyagi Nairiku earthquake (red vertical lines) for the station pair of N.HMNH-N.ONDH, which crosses around the epicenter. In the case of the station pair of N.ADTH-N.TSTH, there was no significant decoherence related to the 2008 Iwate-Miyagi Nairiku earthquake, but a clear decoherence was detected associated with the 2011 Tohoku-Oki earthquake.

3.2.2 Imaging method of seismic scattering property changes

As mentioned in chapter 1, a seismic scattering property change causes waveform changes. Hence, we firstly compute decoherence (1−(coherence)) values. As shown in Figure 3.2, coherence levels before the earthquake are different from different station pairs. For example, the coherences are not high even before the earthquake for the station pair N.HMNH-N.ONDH whose inter-station distance is long. Therefore, we use differences of coherence values before and after the earthquake to focus on the coseismic change of decoherences: Firstly, we compute decoherence values between the RCCF and each 60-days-stacked CCF. Secondly, we subtract the decoherence value before the earthquake from the value after the earthquake:

$$dc_{12}^{obs}(t) = |dc_2^{obs}(t) - dc_1^{obs}(t)|. \tag{3.1}$$

Observed decoherence values for the two periods ($dc_1^{obs}(t)$ and $dc_2^{obs}(t)$) are measured by sliding 16 s long time windows from 64 s after the direct Rayleigh wave arrival time to 112 s after the direct Rayleigh wave arrival time without overlapping. In this study, we use later coda part of CCFs to reduce the effect of the temporal changes of noise sources. As shown in Figure 3.1, Rayleigh waves are predominant in our seismic ambient noise CCFs. The penetration depth (a quarter of the wavelength) of Rayleigh waves that are used in our analysis is about 6 km, and hence the observed decoherences are especially sensitive to structural changes down to this depth. We also compute synthesized decoherence values using the following relationship [e.g., *Larose et al.*, 2015; *Margerin et al.*, 2016]:

$$dc_{12}^{syn}(t) = \frac{c\Delta g_{12}}{2} K_{dc}(\mathbf{x}, t; \mathbf{x_R}, \mathbf{x_S}). \tag{3.2}$$

Here, $dc_{12}^{syn}(t)$ is a synthsized decoherence value at a lag time t, c is Rayleigh wave velocity (3 km/s, in this study), Δg_{12} is a variation of the scattering coefficient (inverse of the scattering mean free path) between the Period 1 and 2, and $K_{dc}(\mathbf{x}, t; \mathbf{x_R}, \mathbf{x_S})$ is a decorrelation kernel [*Margerin et al.*, 2016]. $\mathbf{x}$, $\mathbf{x_S}$, and $\mathbf{x_R}$ are the locations of a change region, source, and receiver, respectively. Higher order terms ($(\Delta g_{12})^2, (\Delta g_{12})^3$...) are neglected by assuming scattering in the change region occurs only once. The decorrelation kernel is the spatial weighting function for locating seismic scattering property changes and is defined as follows:

$$K_{\mathrm{dc}}\left(\mathbf{x}, t; \mathbf{x_R}, \mathbf{x_S}\right) = \int_0^t \int_{S^d} \int_{S^d} \frac{I\left(\mathbf{x_R}, t - t'; \mathbf{x}, \mathbf{n}\right) f\left(\mathbf{n}, \mathbf{n}'\right) I\left(\mathbf{x}, t', \mathbf{n}'; \mathbf{x_S}\right) dt' dn' dn}{I\left(\mathbf{x_R}, t; \mathbf{x_S}\right)}. \tag{3.3}$$

Here, $I\left(\mathbf{x}, t', \mathbf{n}'; \mathbf{x_S}\right)$ is a specific intensity. This represents the energy flux along a direction $\mathbf{n}'$ at $\mathbf{x}$ at the lapse time of t' (see also Figure 3.3 (a)). $I\left(\mathbf{x_R}, t - t'; \mathbf{x}, \mathbf{n}\right)$ represents the intensity at $\mathbf{x_R}$ at the lapse time of $t - t'$ which is radiated from $\mathbf{x}$ along the direction $\mathbf{n}$ (see also Figure 3.3 (b)). $f\left(\mathbf{n}, \mathbf{n}'\right)$ is a phase function which represents a scattering in the change region. $I(\mathbf{x_R}, t; \mathbf{x_S})$ represents total intensity which represents all energy transportations from the source to the receiver at the lapse time of t (see also Figure 3.3 (c)). By using reciprocity and assuming the isotropic scattering in the change region ($f\left(\mathbf{n}, \mathbf{n}'\right) = 1/S^d$), we obtain the following relationship by integrating the numerator of equation (3.3) over all directions:

$$K_{\mathrm{dc}}\left(\mathbf{x}, t; \mathbf{x_R}, \mathbf{x_S}\right) = \frac{\int_0^t I(\mathbf{x_R}, t - t'; \mathbf{x}) I(\mathbf{x}, t'; \mathbf{x_S}) dt'}{I(\mathbf{x_R}, t; \mathbf{x_S})}. \tag{3.4}$$

Here, $I(\mathbf{x}, t'; \mathbf{x_S})$ is the energy propagator from the source to the change region, and $I(\mathbf{x_R}, t - t'; \mathbf{x})$ is that from the change region to the receiver. As mentioned above, Rayleigh waves are predominant in seismic ambient noise CCFs. Therefore, energy propagators $I(\mathbf{x_R}, t; \mathbf{x_S})$, $I(\mathbf{x}, t'; \mathbf{x_S})$, and $I(\mathbf{x_R}, t - t'; \mathbf{x})$ are calculated using the 2-D radiative transfer model for scalar waves assuming isotropic scattering and source radiation in an infinite medium are used in this study [e.g., *Shang and Gao*, 1988; *Sato*, 1993]. The energy propagator is described as follows:

$$I(r,t) = \frac{\mathrm{e}^{-ctg_0}}{2\pi cr}\delta\left(t-\frac{r}{c}\right) + g_0\frac{\mathrm{e}^{g_0(\sqrt{c^2t^2-r^2}-ct)}}{2\pi\sqrt{c^2t^2-r^2}}H\left(t-\frac{r}{c}\right). \tag{3.5}$$

Here, r is the distance between source and receiver, g_0 is the total scattering coefficient, and H is the Heaviside function. In our study, we also consider an intrinsic absorption parameter b. An energy propagator for the spatially homogeneous intrinsic absorption is obtained by multiplying e^{-bt} with the right-hand-side of Equation (3.5). To calculate sensitivity kernels, the values of scattering coefficient and intrinsic absorption parameter in a study area are necessary. The target area of this study extends widely, about 500 km in the north-south and about 250 km in the east-west directions, and some previous studies reported strong regional dependence of those parameters in Japan [e.g., *Hoshiba*, 1993; *Carcolé and Sato*, 2010]. Such spatial nonuniformity of scattering coefficient and intrinsic absorption parameter makes the calculation of sensitivity kernels practically difficult in terms of a calculation cost. Although scattering mean free paths at the frequency band lower than 0.5 Hz are not yet determined, they will be more than 100 km (see also Figure 2.14). In the present study, we fix the scattering mean free path and intrinsic absorption parameter over the study area to 100 km and 0.04 s^{-1}, respectively. Figure 3.4 shows an example of the sensitivity kernel for the station pair of N.ICEH-N.KMYH. On the sensitivity kernel, there are two peaks around two seismic stations. This means that if a change region of seismic scattering is located close to the stations, large decoherences should occur.

We apply the linear least-squares inversion using the following equation to estimate Δg values:

$$\mathbf{d} = \mathbf{G}\mathbf{m}, \tag{3.6}$$

$$d_i = dc_i^{obs}, G_{ij} = \frac{c\Delta s}{2}K_{ij}, m_j = \Delta g_j. \tag{3.7}$$

$\mathbf{d}$ is a data vector of which each component d_i corresponds to an observed decoherence value for each station pair and lag time. $\mathbf{G}$ is a matrix of which each component G_{ij} corresponds to the sensitivity kernel K_{ij} for station pair i in cell j that is evaluated at each lag time and is weighted by the surface area of the cells Δs and Rayleigh wave velocity c. $\mathbf{m}$ is a model vector, for which each component m_j contains the Δg for each small cell j. In this study, we divide the study area into 355 small cells with a size of $0.15^\circ \times 0.15^\circ$

and estimate Δg values for all small cells (Figure 3.5). As mentioned in chapter 1, the size of small cells should be set to be smaller than the scattering mean free path so that the scattering occurs only once within each small cell to linearize inverse problems. We estimate the model vector $\mathbf{m}$ by using an ordinary linear least-squares inversion with ℓ^2 norm regularization which minimizes the following objective function:

$$F = \frac{1}{2}||\mathbf{d} - \mathbf{G}\mathbf{m}||_2^2 + \lambda||\mathbf{m}||_2. \tag{3.8}$$

The first term of equation (3.8) is the sum of squared residuals (SSRs) between observed and synthesized decoherence values. The second term is the ℓ^2 norm of a model vector and λ is a hyperparameter. Here, the optimal value of λ is determined by using a trade-off curve between the first and second terms of the right-hand side of equation (3.8).

3.3 Results

In this study, we use station pairs whose inter-station distances are shorter than 100 km (after the Iwate-Miyagi Nairiku earthquake; Jun. 15 2008 - Mar. 8 2011) or 150 km (after the Tohoku-Oki earthquake; Mar. 12 2011 - Nov. 10 2011). Moreover, we select decoherence values according to signal-to-noise ratios (SNRs) of 60-days-stacked CCFs. A Root-Mean-Square (RMS) amplitude of a CCF from -195 s to -190 s and +190 s and +195 s in lag times is defined as a noise level. The RMS amplitude of a CCF for each 16 s long time window is defined as a signal level. We only use decoherence values from time windows whose SNRs are larger than 2.0 (Jun. 15 2008 - Mar. 8 2011) or 2.5 (Mar. 12 2011 - Nov. 10 2011). Figures 3.6-3.8 show spatial distributions of Δg values for respective 60-days long time periods since the 2008 Iwate-Miyagi Nairiku earthquake. Just after the Iwate-Miyagi Nairiku earthquake, the region with a large Δg value is estimated around the epicenter of the main shock, and its Δg value is 5.7×10^{-4} km^{-1} ($\Delta g/g_0 = 5.7$ %) at a maximum (Figure 3.6 (a)). In the following two time periods (Figures 3.6 (b) and (c)), such regions of large changes are not estimated. The maximum Δg values in these periods are 1.3×10^{-4} km^{-1} and 1.4×10^{-4} km^{-1}, respectively. This indicates that the large seismic scattering property change around the epicenter already recovered.

Just after the Tohoku-Oki earthquake (Figure 3.7 (i)), regions of large seismic scattering property changes are located around some active volcanoes in Tohoku region (black triangles): The maximum Δg is estimated around Bandai volcano, and its value is estimated to be 3.6×10^{-4} km^{-1} ($\Delta g/g_0 = 3.6$ %). Moreover, 3.4×10^{-4} km^{-1} and 3.1×10^{-4} km^{-1} of

Δg values are estimated at the south of Iwate volcano and at the east of Naruko volcano. In the case of the 2008 Iwate-Miyagi Nairiku earthquake, the large seismic scattering property change around the epicenter disappeared after 60 days from the mainshock. On the other hand, in the case of the 2011 Tohoku-Oki earthquake, the regions of large seismic scattering property changes around the active volcanoes still remained after 60 days from the mainshock: The maximum change is located to the west of the Kurikoma volcano in the period between May 12 and Jul. 11 in 2011 (Figure 3.8 (a)). In the next period (Jul. 12 and Sep. 10 in 2011; right panel in Figure 3.8 (b)), the maximum change is located to the west of the Bandai volcano. The maximum Δg value in these periods is 2.5×10^{-4} km^{-1}.

Figures 3.9 (a) and (b) show the observed and synthesized decoherence values for all station pairs and lag times in time periods just after the Iwate-Miyagi Nairiku earthquake (Jun. 15 - Aug. 14 in 2008) and the Tohoku-Oki earthquake (Mar. 12 - May 11 in 2011). Synthesized decoherence values are calculated using the estimated model parameters and decorrelation kernels. The observed decoherences show spiky-shaped variations, and synthesized ones cannot necessarily explain such spiky-shaped parts. However, synthesized decoherences capture the whole features of observed ones.

3.4 Discussions

3.4.1 Recovery tests

To check the reliability of our inversion results, we conduct recovery tests. Figure 3.10 (a) and (b) show input models of the recovery tests. We input Δg value of 0.001 km^{-1} ($\Delta g/g_0$=10 %) to only four small cells around the epicenter of the Iwate-Miyagi Nairiku earthquake or around the Bandai volcano. Input Δg values for the other small cells are zero. Firstly, we compute synthesized decoherence values for this input model using equation (3.2). Secondary, we add noises to these synthesize decoherences:

$$dc_i^{syn'}(t) = dc_i^{syn}(t) + \varepsilon_i. \tag{3.9}$$

Here, $dc_i^{syn}(t)$ is the synthesized decoherence value from the input model for a station pair i. ε_i is the noise term and is sampled from a gaussian distribution $\varepsilon_i \sim N(0, \sigma_i^2)$, which is defined for each station pair. We compute coherence values between a RCCF and 60-days-stacked CCFs during 5 years, and calculate a variance of these coherence values for each station pair. Here, we do not use 60-days-stacked CCFs just after the Iwate-Miyagi

Nairiku earthquake and the Tohoku-Oki earthquake. We use the variance as σ_i^2 for each station. Thirdly, we estimate a spatial distribution of Δg values using $dc_i^{syn'}(t)$ as input data. We repeat the same estimation for 50 times with changing $dc_i^{syn'}(t)$.

Figures 3.10 (c) and (d) show the estimation results for each input model. The input change regions are almost recovered. The Δg values shown in Figure 3.10 (c) are averaged for 50 estimations. The Δg value around the epicenter of the Iwate-Miyagi Nairiku earthquake is estimated to be $8.1\times10^{-4}\pm1.4\times10^{-5}$ km^{-1}, and this value is 81 % of the input value (0.001 km^{-1}). The Δg value around the Bandai volcano is estimated to be $8.0\times10^{-4}\pm2.1\times10^{-5}$ km^{-1}, and this value is 80 % of the input value. Figure 3.10 (e) shows the histogram of estimated Δg values around the epicenter of the Iwate-Miyagi Nairiku earthquake. The red line represents the input Δg value at this small cell. These estimated Δg values are always smaller than the input value. The maximum and minimum value of estimated Δg values are 7.8×10^{-4} km^{-1} and 8.4×10^{-4} km^{-1}, respectively. Figure 3.10 (f) shows the histogram of estimated Δg values around the Bandai volcano. The maximum and minimum estimated Δg values are 7.6×10^{-4} km^{-1} and 8.5×10^{-4} km^{-1}, respectively.

The results of those recovery tests indicate that the regions of large seismic scattering property changes, which are estimated around the epicenter of the 2008 Iwate-Miyagi Nairiku earthquake and around the Bandai volcano, are reliable.

3.4.2 Comparison with other observations

In some previous studies, seismic velocity reductions related to the 2008 Iwate-Miyagi Nairiku earthquake were detected by seismic interferometry analyses [e.g., *Takagi et al.*, 2012; *Hobiger et al.*, 2012; *Hobiger et al.*, 2014; *Wang et al.*, 2017]. Takagi et al. [2012] reported about 0.3-0.4 % of Rayleigh wave velocity decreases at the southern part of the fault zone in the 0.25-0.5 Hz band. Hobiger et al. [2012] detected about 0.6 % velocity decreases at a maximum in the 0.5-1 Hz band around the south of the epicenter. These previous studies compared seismic velocity changes with peak ground acceleration (PGA), and concluded that such large seismic velocity decreases were caused by the strong ground motion. A large coseismic slip at the south of the epicenter was detected by GNSS observations [e.g., *Ohta et al.*, 2008; *Iinuma et al.*, 2009]. Figure 3.11 (a) shows spatial distribution of Δg values around the focal area of the 2008 Iwate-Miyagi Nairiku earthquake. The gray rectangles in Figure 3.11 (a) represent the fault planes estimated by Ohta et al. [2008]. The slip amounts were estimated to be 1.8 m for the northern fault plane and 3.5 m for the southern one, respectively. The region of the largest Δg overlaps with the southern fault planes, suggesting a possibility that the large fault slip caused seismic

scattering property changes. Suzuki et al. [2010] estimated the fault slip distribution by waveform inversions using strong-motion data recorded at K-NET and KiK-net stations. The maximum slip was estimated to be 6.2 m for the area approximately 10 km to the south of the main shock, and this region is well consistent with the region of the largest Δg. The region of large slip extended from about 1 km to 6 km at depth. The penetration depth (a quarter of the wavelength) of Rayleigh waves that are used in our analysis is about 6 km. This result also supports our interpretation that a large structural change due to the large slip might have caused seismic scattering property changes. Figure 3.11 (b) shows the spatial distribution of PGAs observed at K-NET and KiK-net stations. An accelerometer located near the epicenter recorded a strong motion of approximately 4,000 gal [*Aoi et al.*, 2008], and that is consistent with the region of large seismic scattering property changes. The change region of large seismic scattering property changes includes Kurikoma volcano. The crustal fluid will exist beneath the active volcano, and it can have caused the seismic scattering property changes. Moreover, landslides occurred around Kurikoma volcano associated with the earthquake. Such an area of material weakness can be related to the seismic scattering property changes.

In the case of the 2011 Tohoku-Oki earthquake, the change regions of large seismic scattering properties were located around active volcanoes in Tohoku region. Figure 3.12 shows the spatial distribution of PGAs. The region of large PGAs extends near the eastern coastline, and this distribution is not consistent with that of the region of large seismic scattering property changes. Therefore, we interpret that significant seismic scattering property changes associated with this earthquake have not been caused by strong ground motion. Brenguier et al. [2014] succeeded in detecting about 0.1 % seismic velocity decreases along the volcanic front associated with the Tohoku-Oki earthquake by using seismic interferometry. They interpret that dynamic stress changes related to the passing of seismic waves caused such coseismic velocity reductions as related to the mechanical weakening of the pressurized crust. Our results of spatial distributions of seismic scattering property changes are more localized in the vicinities of some active volcanoes than the results of Brenguier et al. [2014]. Significant volcanic subsidences associated with the 2011 Tohoku-Oki earthquake were detected by analyses of interferometric synthetic aperture radar (InSAR) data [*Takada and Fukushima*, 2013]. The amount of these subsidences were 5-15 cm with horizontal dimensions of up to 15-20 km. They were interpreted that magmatic and hot plutonic bodies beneath the volcanoes had deformed and subsided in response to stress changes associated with the earthquake. Our results and the results of these previous studies suggest that significant structural changes occurred beneath active

volcanoes in Tohoku region associated with the 2011 Tohoku-Oki earthquake.

There are many possible causes of seismic scattering property changes associated with the 2008 Iwate-Miyagi Nairiku earthquake and the 2011 Tohoku-Oki earthquake. It is still difficult to identify the cause of seismic scattering property changes. Estimating space-time changes of seismic scattering properties for various earthquakes and volcanic activities is important to improve our understanding of seismic scattering property changes.

3.4.3 Spatial distributions of seismic scattering property changes in quiet periods

As we can see in Figures 3.6-3.8, regions of large seismic scattering property changes are also estimated in some time periods when no large earthquakes occurred. Figures 3.13 (a) and (c) show the spatial distributions of Δg values in the period of Dec. 16 2009 - Feb. 14 2010 and Nov. 7 2010 - Jan. 6 2011, respectively. In these periods, regions of large seismic scattering property changes were estimated at the southwest part of Tohoku region. The maximum value of Δg in those periods are about 3.0×10^{-4} km^{-1} ($\Delta g/g_0$=3.0 %). This value is about 83 % of that of just after the 2011 Tohoku-Oki earthquake. We compare the spatial distributions of Δg values in those periods with precipitations. Figures 3.13 (b) and (d) show the spatial distributions of precipitations in the same periods. In winter seasons, precipitations during 60 days in the southwest part of Tohoku region become over 1000 mm due to heavy snowfalls. Figures 3.13 (e) shows standard deviations of monthly precipitations over 5 years. Seasonal variations are especially strong in the southwest part of Tohoku region. The regions of large seasonal precipitations are almost consistent with the regions of large seismic scattering property changes. In other region, Obermann et al. [2014] detected significant seismic scattering property changes at the south of the focal area of the 2008 Wenchuan, China, earthquake in monsoon seasons. They interpreted that change in river load or flooding by heavy rainfalls caused the seismic scattering property changes.

Except for the significant seismic scattering property changes in the southwest part of Tohoku region, we can find seismic scattering property changes in the northern part and eastern part of Tohoku region (Figures 3.13 (a) and (c)). Those change regions are estimated in many time periods. Figures 3.14 (a) and (b) show spatial distributions of mean and standard deviation of Δg values over 5 years. We compute these values of each 60-days-long period. Δg values in the time periods just after the 2008 Iwate-Miyagi Nairiku earthquake (Jun. 15 - Aug. 14 in 2008) and the 2011 Tohoku-Oki earthquake (Mar. 12 - May 11 in 2011) are not used for the calculations of mean and standard

deviation values. Therefore, those figures indicate background Δg values during 5 years and seasonal variations, respectively. The mean Δg values in the north part of Tohoku region and in the east part of Tohoku region are about 1.4×10^{-4} km^{-1} ($\Delta g/g_0 = 1.4$ %) at a maximum. On the other hand, the standard deviations of Δg values in this region are quite smaller than that in the southwest part of Tohoku region. This means that seismic scattering property changes in the northern part of Tohoku region are not seasonal changes like those in the southwest part of Tohoku region, suggesting that possible causes of the seismic scattering changes in these two regions are different. Regarding seismic velocities, the effects of external environmental perturbations have been reported by many previous studies: rainfall [e.g., *Sens-Schönfelder and Wegler*, 2006; *Meier et al.*, 2010; *Tsai*, 2011], thermoelastic stress [e.g., *Meier et al.*, 2010; *Hillers et al.*, 2015], ocean loading [e.g., *Wang et al.*, 2017], snow loading [e.g., *Hatovec-Ellis et al.*, 2014], and atmospheric pressure [*Silver et al.*, 2007]. Evaluating such meteorological effects will be important for interpreting seismic scattering property changes as well.

3.5 Conclusion

Applying seismic interferometry to the seismic ambient noise data in the northeast part of Japan at the 0.125-1 Hz band, we estimated spatio-temporal changes of seismic scattering properties from 2008 to 2012 using linear least-squares inversions with sensitivity kernels. We succeeded in detecting large seismic scattering property changes around the epicenter of the 2008 Iwate-Miyagi Nairiku earthquake. The maximum Δg value was 5.7×10^{-4} km^{-1} ($\Delta g/g_0 = 5.7$ %). Structural changes due to the large fault slip and/or the strong ground motion may have introduced the large seismic scattering property change in the shallow medium to the south of the epicenter. We also detected significant seismic scattering property changes around some active volcanoes in Tohoku region associated with the 2011 Tohoku-Oki earthquake. The maximum change was estimated around Bandai volcano and its Δg value was 3.6×10^{-4} km^{-1} ($\Delta g/g_0 = 3.6$ %). Significant seismic velocity changes and subsidences around active volcanoes in Tohoku region associated with the 2011 Tohoku-Oki earthquake have been reported by some previous studies. Our results also suggest that significant structural changes occurred beneath active volcanoes in Tohoku region associated with the 2011 Tohoku-Oki earthquake. In the southwest part of Tohoku region, strong seasonal seismic scattering property changes were detected. The maximum Δg value was estimated to be 3.0×10^{-4} ($\Delta g/g_0$=3.0 %) in winter. These regions were correlated with those of large precipitations. Evaluating such a meteorological effect on seismic scattering property changes should be important to interpret results of

time-lapse imagings.

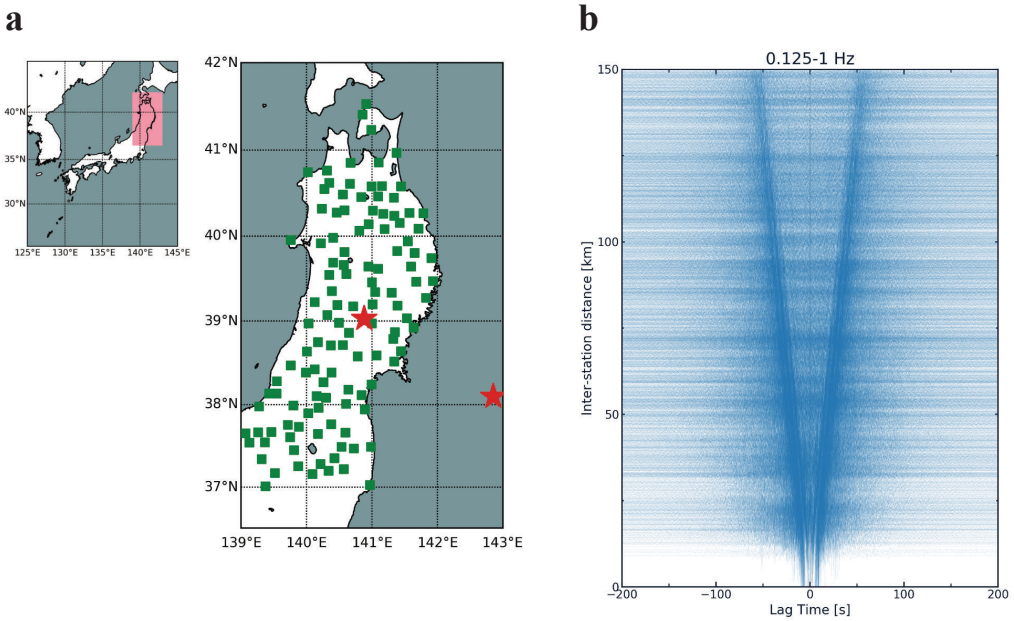

Figure 3.1 (a) Locations of 121 Hi-net stations (green squares). The epicenter of the 2008 Iwate-Miyagi Nairiku earthquake is indicated by the red star at the center of the figure and that of the 2011 Tohoku-Oki earthquake is indicated by the red star at the right of the figure. (b) Record section of seismic ambient noise CCFs in the 0.125-1 Hz band. These CCFs are computed by stacking daily CCFs over 5 years (2008-2012).

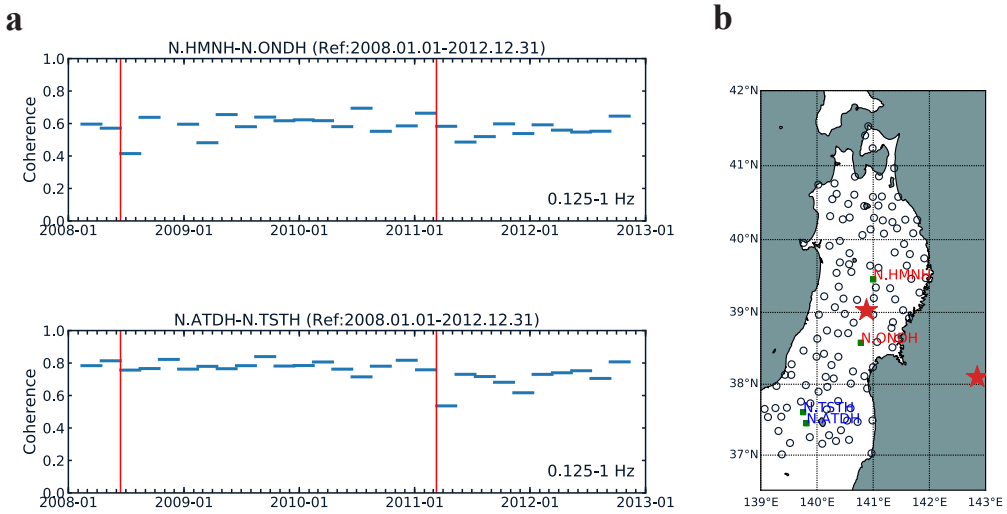

Figure 3.2 (a) Temporal changes of coherences for station pairs of N.HMNH-N.ONDH (top) and N.ATDH-N.TSTH (bottom). Each blue horizontal bars represent a coherence between a RCCF (5-years-stacked CCF) and 60-days-stacked CCF. The red vertical lines represent the times of the 2008 Iwate-Miyagi Nairiku earthquake and the 2011 Tohoku-Oki earthquake. (b) Locations of seismic stations that are used in (a).

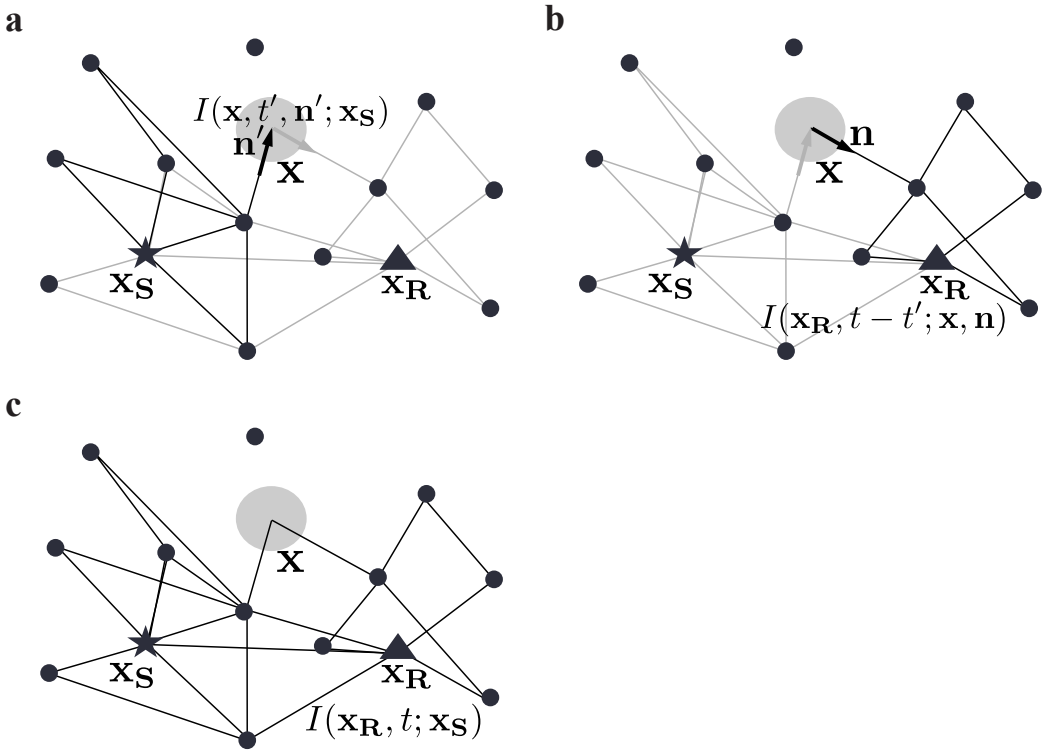

Figure 3.3 Schematic illustration of each intensity in equation (3.3). The black circles represents scatterers. The gray ellipses represent change regions of seismic scattering properties. (a) Specific intensity $I(\mathbf{x}, t', \mathbf{n}'; \mathbf{x_S})$. (b) Intensity $I(\mathbf{x_R}, t - t'; \mathbf{x}, \mathbf{n})$. (c) Total intensity $I(\mathbf{x_R}, t; \mathbf{x_S})$.

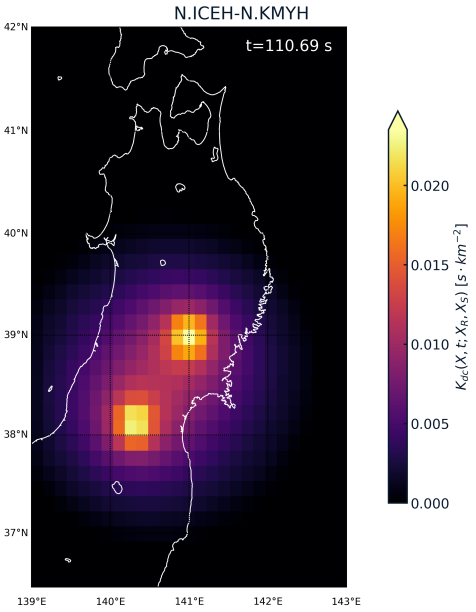

Figure 3.4 An example of the decorrelation kernel for the station pair of N.ICEH-N.KMYH at 110.69 s in lag time. The kernel is calculated assuming the scattering mean free path and intrinsic absorption parameter of Rayleigh wave to be 100 km and 0.04 s^{-1}, respectively.

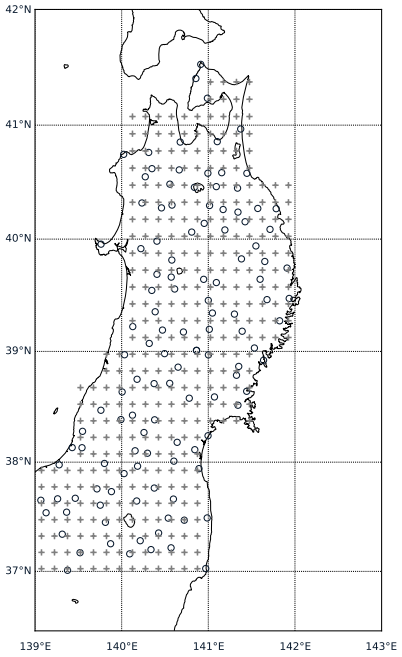

Figure 3.5 Distributions of grid points for linear-least squares inversions (gray crosses). The interval between each grid point is 0.15°. The open circles represent Hi-net stations used in this study.

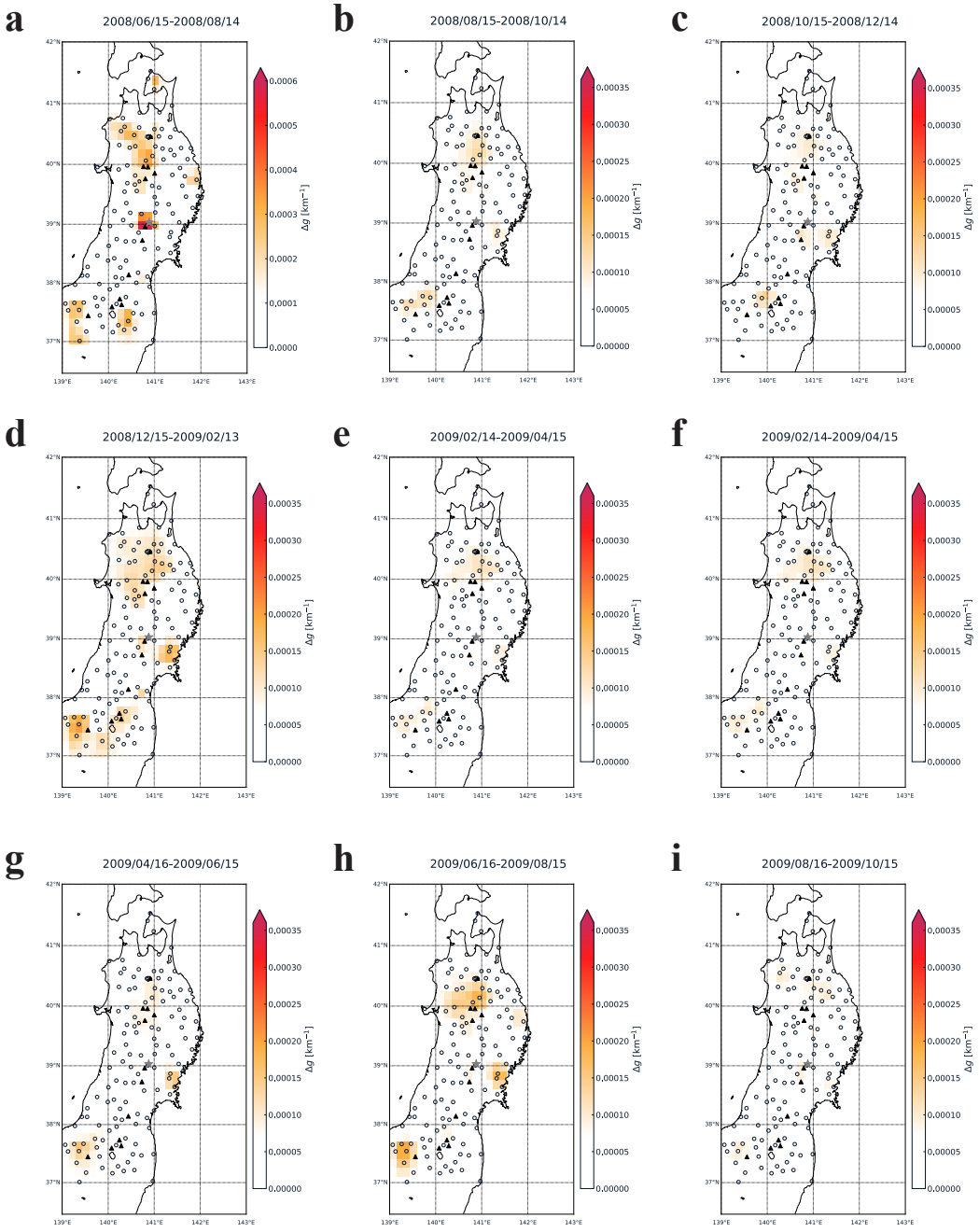

Figure 3.6 Spatial distributions of Δg values for nine 60-days-long periods since the 2008 Iwate-Miyagi Nairiku earthquake. Solid and open circles on each panel represent active volcanoes and Hi-net stations in the Tohoku region, respectively.

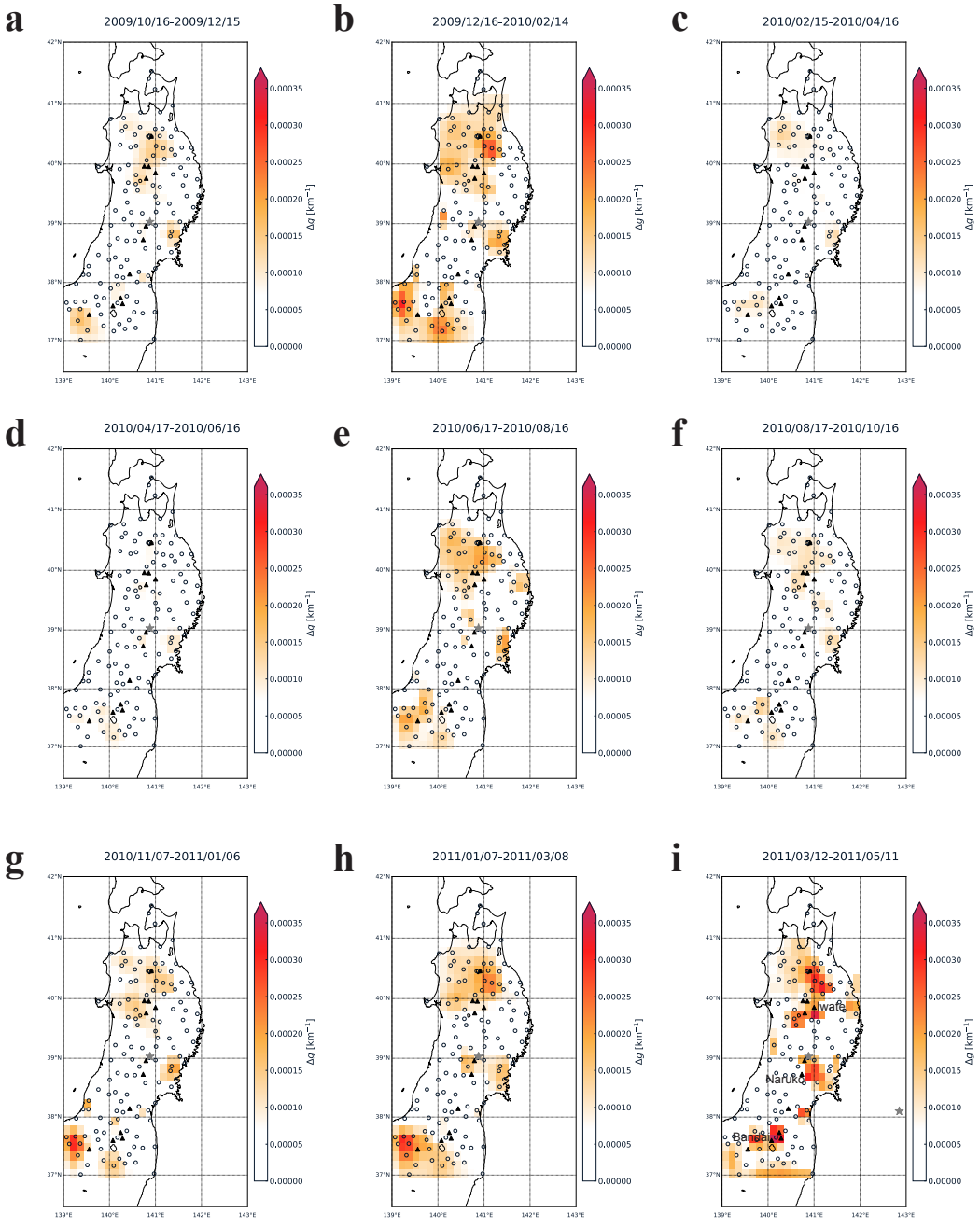

Figure 3.7 Spatial distributions of Δg values for the next nine periods.

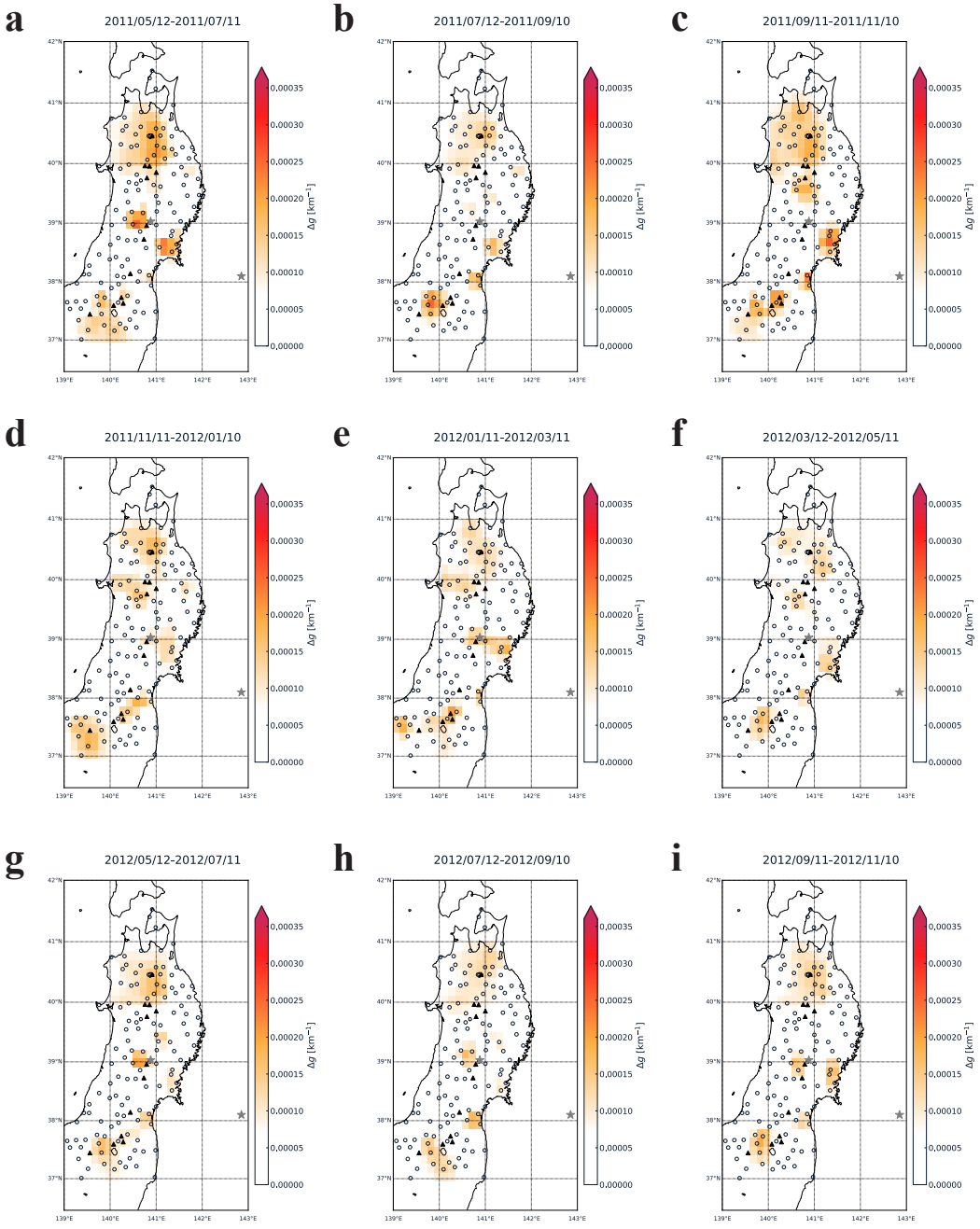

Figure 3.8 Spatial distributions of Δg values for the next nine periods.

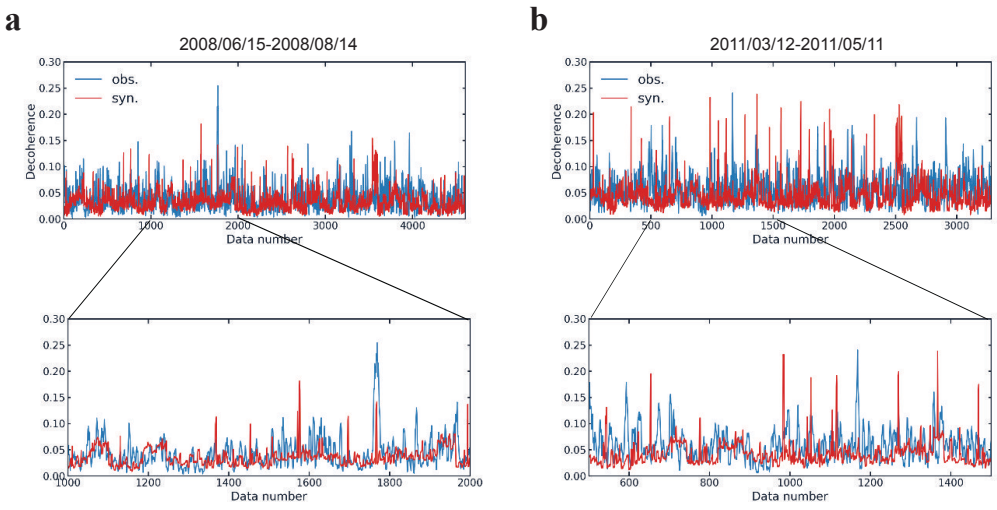

Figure 3.9 (a) Observed (blue) and synthesized (red) decoherence values for all station pairs and lag times in the period of Jun. 15 - Aug. 14 in 2008 (just after the 2008 Iwate-Miyagi Nairiku earthquake). The synthesized decoherence values are computed using estimated Δg values and decorrelation kernels. (b) Those in the period of Mar. 12 - May 11 in 2011 (just after the 2011 Tohoku-Oki earthquake).

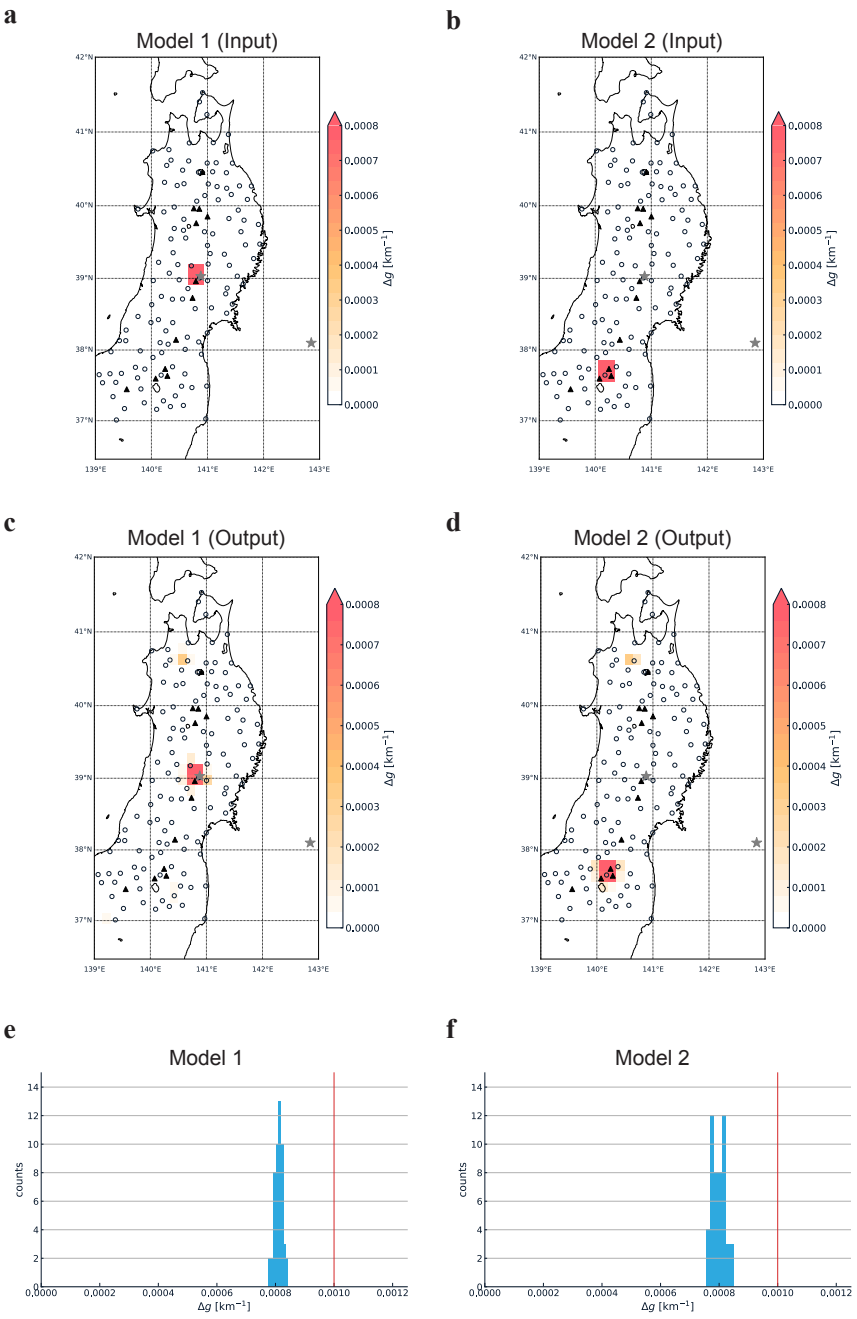

Figure 3.10 (a) Input model of the recovery tests. Δg value of 0.001 km^{-1} ($\Delta g/g_0$=10 %) is input to only four small cells around the epicenter of the Iwate-Miyagi Nairiku earthquake. Input Δg values for the other small cells are zero. (b) Input model which is inputted Δg value of 0.001 km^{-1} to four small cells around the Bandai volcano. (c)-(d) The result of the recovery tests for each input model. Δg values shown in the figure are averaged for 50 estimations. (e)-(f) The histogram of estimated Δg values for each input model. These Δg values are averaged ones for the four small cells. The red vertical line represents the input Δg value (0.001 km^{-1}) to these small cells.

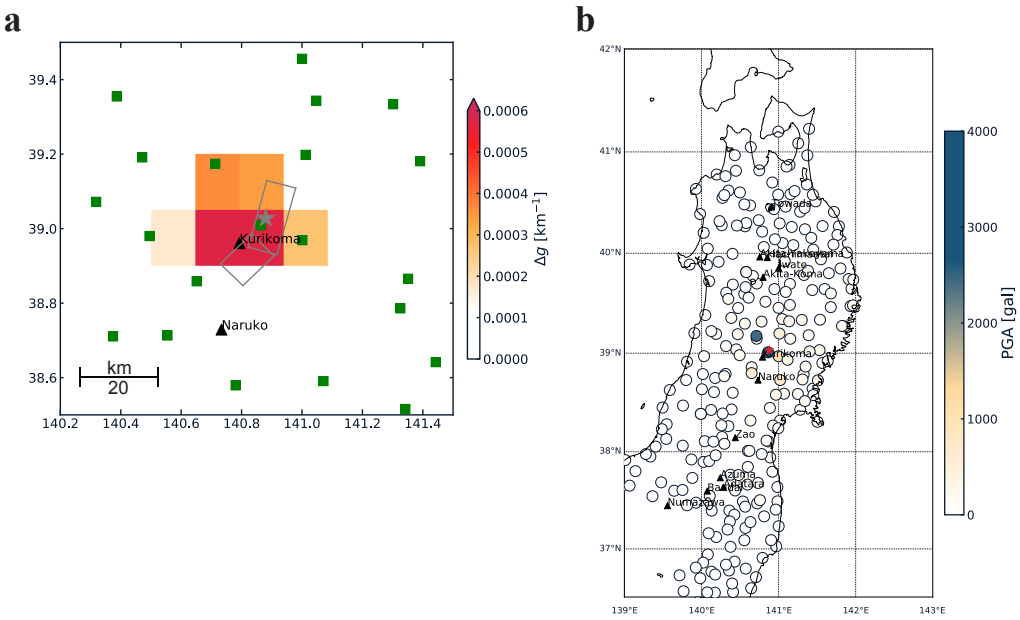

Figure 3.11 (a) Spatial distribution of Δg values around the focal area of the 2008 Iwate-Miyagi Nairiku earthquake. The two subfaults estimated by Ohta et al [2008] are shown by the gray rectangles. (b) Peak ground acceleration (PGA) associated with the 2008 Iwate-Miyagi Nairiku earthquake observed at K-NET and KiK-net stations. The PGA is the maximum amplitude of the three-component vector.

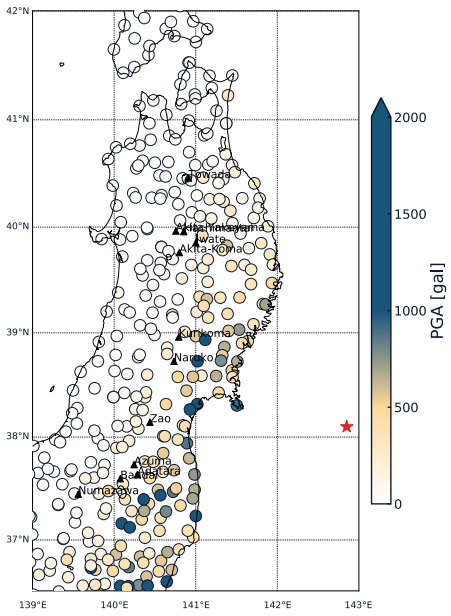

Figure 3.12 PGA associated with the 2011 Tohoku-Oki earthquake.

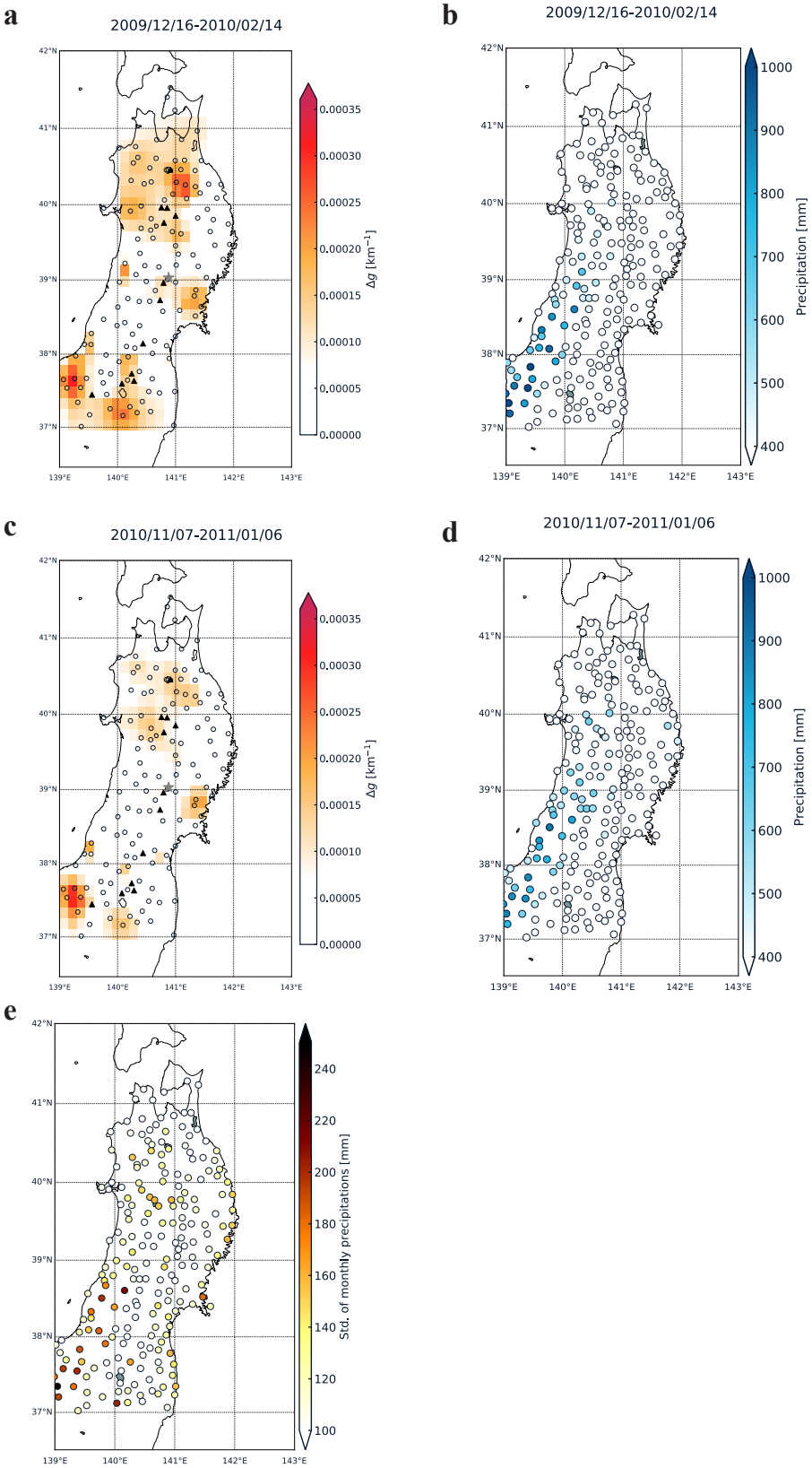

Figure 3.13 (a) Spatial distribution of Δg values in the period of Dec. 16 2009 - Feb. 14 2010. (b) Precipitations during the same period of (a). (c) Spatial distribution of Δg values in the period of Nov. 7 2010 - Jan. 6 2011. (d) Precipitations during the same period of (c). (e) Standard deviations of monthly precipitations over 5 years.

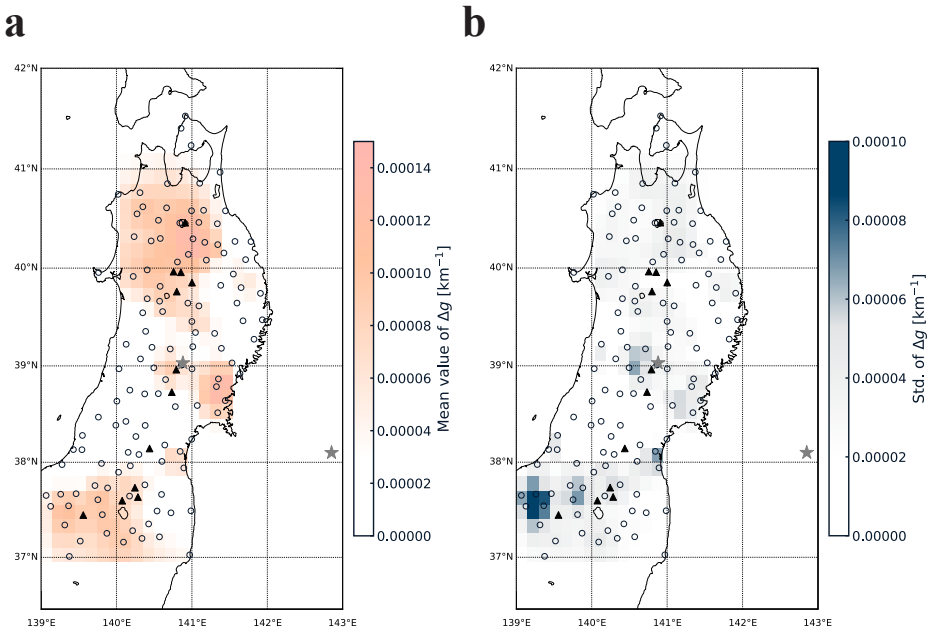

Figure 3.14 (a) Spatial distribution of mean Δg values over 5 years. (b) Spatial distribution of standard deviation of Δg values over 5 years. On the calculations of mean and standard deviation values, Δg values in the time periods just after the 2008 Iwate-Miyagi Nairiku earthquake (Jun. 15 - Aug. 14 in 2008) and the 2011 Tohoku-Oki earthquake (Mar. 12 - May 11 in 2011) are not used.

Chapter 4

Sparse modeling of seismic ambient noise CCFs for time-lapse imaging in a weak scattering regime: Application to the 2008 Iwate-Miyagi Nairiku, Japan, earthquake

4.1 Introduction

In recent years, spatial distributions of seismic scattering property changes associated with volcanic activities or earthquakes have been estimated using seismic ambient noise CCFs and linear least-squares inversions [e.g., *Obermann et al.*, 2013; *Obermann et al.*, 2014; *Hillers et al.*, 2015; *Machacca et al.*, 2019]. We also estimated spatio-temporal changes of seismic scattering properties in the northeast part of Japan in chapter 3. Although locating change regions of seismic velocities and seismic scattering properties is important for the structural monitoring, a large number of seismic stations are necessary to estimate spatial distributions of medium changes. For example, Obermann et al. [2013] used 19 broadband seismic stations that are deployed in the area with about 15 km in the east-west and 10 km in the north-south directions. Obermann et al. [2014] used 114 seismic stations in the target area (29° to 32°N and 100° to 105°E). Conducting such estimations is not easy in the regions where only a small number of stations are set up.

Sparse modeling is a technique that enables us to determine model parameters from a small data set by imposing ℓ^1 norm regularization [*Tibshirani*, 1996]. The ℓ^1 norm regularization approaches have been applied in reflection seismology problems in the last four decades [e.g., *Claerbout and Muir*, 1973; *Santosa and Symes*, 1986]. In recent years, these techniques have been used for locating seismic sources or geodetic inversions [e.g., *Yao et al.*, 2011; *Evans and Meade*, 2012; *Nakata et al.*, 2016]. Yao et al. [2011] located the distribution of source powers during the rupture of the 2011 Tohoku-Oki, Japan, earthquake from teleseismic P-waves recorded by an array of stations in the United States. Their estimation results of the source power distribution at the 0.5-1 and 0.2-0.5 Hz bands shared similar features as back-projection results by other previous studies that revealed

dominant seismic energy radiation in the down-dip. They also confirmed that the source power distributions at the 0.1-0.2 and 0.05-0.1 Hz bands were almost consistent with slip inversion results from seismic data and geodetic data that revealed dominant large-slip patches close to the trench. Evans and Meade [2012] estimated spatial distributions of coseismic slip and postseismic afterslip associated with the 2011 Tohoku-Oki earthquake using Global Navigation Satellite System data and the sparse modeling. They compared results from the sparse modeling with those from the damped least squares inversion, and showed that the sparse modeling recovered more compact and sharply varying slip distributions than those from the damped least squares inversion. They concluded that such a sharp image allows quantitative assessments of the spatial relationship between coseismic slip and the rest of the earthquake cycle. There are such previous studies that applied the sparse modeling for locating seismic sources or geodetic inversions, however, there seems no previous study which applied this technique to estimate the spatial distribution of seismic scattering property changes.

The 2008 Mw 6.9 Iwate-Miyagi Nairiku earthquake occurred on 14 June 2008 (Japan Standard Time) in the central part of Tohoku region in northeast Japan. We already estimated spatial distributions of seismic scattering property changes associated with this earthquake in chapter 3 and succeeded in detecting large seismic scattering property changes around the epicenter of the main shock from the data of 121 seismic stations. In this chapter, we conduct the imaging of scattering property using sparse modeling with only 17 seismic stations. An ordinary linear least-squares inversion with ℓ^2 norm regularization is also applicable to the data from 17 seismic stations. Hence, we can directly compare results from sparse modeling and those from the linear least-squares inversion with the ℓ^2 norm regularization. Moreover, we can explore the applicability of the sparse modeling by changing the numbers and distributions of seismic stations.

4.2 Data and method

4.2.1 Calculation procedure of seismic ambient noise CCFs

We use seismograms recorded at 17 Hi-net stations maintained by NIED which are shown by green squares in Figure 4.1 (a). A three-component short-period seismometer with a natural frequency of 1 Hz is installed at each station. All the seismograms are recorded with a sampling frequency of 100 Hz. We apply seismic interferometry to the seismic ambient noise data on the vertical component during the years of 2007 and 2008. Firstly, we filter seismic ambient noise records at the 0.5-1 Hz band and select 10 minute-long data

having amplitudes of smaller than 10 times the average Root-Mean-Square amplitude of seismic ambient noise recorded in 2007. Secondly, we apply temporal flattening technique [*Weaver*, 2011] and spectral whitening [e.g., *Shapiro et al.*, 2006; *Bensen et al.*, 2007] for suppressing the influence of earthquakes and persistent monochromatic noise sources on seismic ambient noise CCFs. Thirdly, we compute CCFs every 10 minutes and calculate daily CCFs (hereafter called DCCFs) by stacking these 10-min CCFs every day for 136 pairs from 17 stations. The obtained DCCFs are considered to be Green's functions recorded at one of a station pair from a virtual source at the other station of the pair. Figure 4.1 (b) is a record section of CCFs at the 0.5-1 Hz band. These CCFs are computed by stacking DCCFs over 1 year in 2017. The wave packets of Rayleigh waves whose propagating speed is about 3 km/s can be seen. In this study, we use these 1-year-stacked CCFs as reference CCFs (hereafter called RCCFs). Figure 4.2 shows temporal changes of coherence values over 2 years for 4 station pairs (N.ICEH-N.NRKH, N.OGCH-N.ICEH, N.HMSH-N.SMTH, and N.OGCH-N.TAJH). These coherence values are computed between the RCCF and 10-days stacked CCFs with sliding 10-days-long time windows by 1 day. Those coherence values are average ones for negative and positive lag times, from 16 s after the direct Rayleigh wave arrival time to 64 s after the direct Rayleigh wave arrival time (48 s long). Large decoherences were detected associated with the Iwate-Miyagi Nairiku earthquake (red lines). The pink solid lines represent mean coherence values before the earthquake (Jan. 1 2007 - Jun. 13 2008), and pink dashed lines represent the mean coherence minus three times standard deviations (3σ). The station pairs N.ICEH-N.NRKH and N.OGCH-N.ICEH show sharp decoherences associated with the earthquake. Moreover, the coherences gradually increased after the earthquake, and recovered to around the mean coherences within one month after the earthquake. In contrast, we cannot find such significant decoherences for the station pairs of N.HMSH-N.SMTH and N.OGCH-N.TAJH, which do not cross around the epicenter or both of stations are located far from the epicenter.

4.2.2 Imaging method of seismic scattering property changes

A seismic scattering property change causes waveform changes. We firstly calculate observed decoherence values. As shown in Figure 4.2, the coherence levels before the earthquake are different from different station pairs. For example, the coherences are not good even before the earthquake for the station pair of N.OGCH-N.TAJH whose inter-station distance is long. Therefore we use differences of coherence values before and after the earthquake to focus on the coseismic change of decoherences: we compute decoherence

values between RCCFs and stacked CCFs in 1 May 2008 - 13 Jun. 2008 (hereafter called Period I) and in 15 Jun. 2008 - 31 Jul. 2008 (Period II), respectively. Absolute values of differences of decoherence values in Period I and Period II are computed as follows:

$$dc_{12}^{obs}(t) = \left| dc_2^{obs}(t) - dc_1^{obs}(t) \right|. \tag{4.1}$$

Observed decoherence values for the two periods ($dc_1^{obs}(t)$ and $dc_2^{obs}(t)$) are measured by sliding a 16 s long time windows from 16 s after the direct Rayleigh wave arrival time to 64 s after the direct Rayleigh wave arrival time without overlapping. This is because Obermann et al. [2016] calculated the lapse-time-dependence of energy partition ration between body waves and surface waves, and they pointed out that surface waves were predominant until eight times the mean free time in lapse time. We also calculate synthesized decoherence values using the following relationship [e.g., *Larose et al.*, 2015; *Margerin et al.*, 2016]:

$$dc_{12}^{syn}(t) = \frac{c\Delta g_{12}}{2} K_{dc}(\mathbf{x}, t; \mathbf{x_R}, \mathbf{x_S}). \tag{4.2}$$

Here, $dc_{12}^{syn}(t)$ is a synthsized decoherence value at a lag time t, c is Rayleigh wave velocity (c is fixed to 3 km/s in this study), Δg_{12} is a variation of the scattering coefficient (inverse of the scattering mean free path) between Period I and II, and $K_{dc}(\mathbf{x}, t; \mathbf{x_R}, \mathbf{x_S})$ is a decorrelation kernel [*Margerin et al.*, 2016]. $\mathbf{x}$, $\mathbf{x_S}$, and $\mathbf{x_R}$ are the locations of a change region, source, and receiver, respectively. The decorrelation kernel is the spatial weighting function for locating seismic scattering property changes and is calculated using the following equation:

$$K_{\mathrm{dc}}(\mathbf{x}, t; \mathbf{x_R}, \mathbf{x_S}) = \frac{\int_0^t I(\mathbf{x_R}, t - t'; \mathbf{x}) I(\mathbf{x}, t'; \mathbf{x_S}) dt'}{I(\mathbf{x_R}, t; \mathbf{x_S})}. \tag{4.3}$$

Here, $I(\mathbf{x_R}, t; \mathbf{x_S})$ is an energy propagator based on the 2-D radiative transfer model for scalar waves which assumes isotropic scattering and source radiation in an infinite medium [e.g., *Shang and Gao*, 1988; *Sato*, 1993] (see equation (2.1)). To calculate sensitivity kernels, the values of scattering coefficient and intrinsic absorption parameter in the study area are necessary. The mean free path (inverse of the scattering coefficient) and the intrinsic absorption parameter in the focal area of the Iwate-Miyagi Nairiku earthquake were estimated to be 30 km and 0.02 s^{-1} at the 0.5-1 Hz band as shown in chapter 2. Figure 4.3 shows an example of a sensitivity kernel for the station pair of N.OGCH-N.ICEH. On

the sensitivity kernel, there are two peaks around two seismic stations. This means that if a change region of seismic scattering is located close to the station, large decoherences should occur.

We apply a linear least-squares inversion using the following equation to estimate Δg values:

$$\mathbf{d} = \mathbf{G}\mathbf{m}, \tag{4.4}$$

$$d_i = dc_i^{obs}, G_{ij} = \frac{c\Delta s}{2} K_{ij}, m_j = \Delta g_j \tag{4.5}$$

$\mathbf{d}$ is a data vector of which each component d_i corresponds to observed decoherence values for each station pair and lag time. $\mathbf{G}$ is a matrix of which each component G_{ij} corresponds to the sensitivity kernel K_{ij} for the station pair i in the cell j that is evaluated at each lag time and is weighted by the surface area of the cells Δs, and Rayleigh wave velocity c. $\mathbf{m}$ is a model vector of which each component m_j contains the Δg for the small cell j. In this study, we estimate the model vector $\mathbf{m}$ which minimizes the following objective function:

$$F = \frac{1}{2}||\mathbf{d} - \mathbf{G}\mathbf{m}||_2^2 + \lambda||\mathbf{m}||_1. \tag{4.6}$$

The first term of the right-hand side of equation (4.6) is the sum of squared residuals (SSRs) between observed and synthesized decoherence values. The second term of the right-hand side is the ℓ^1 norm of a model vector and λ is a hyperparameter. The optimization using ℓ^1 norm regularization [e.g., *Tibshirani*, 1996] is also called "Sparse modeling". In sparse modeling, most of the model parameters are estimated to be zero. This means that we can reduce the number of the model parameters, and hence we can estimate a model vector from a small data set. Figures 4.4 (a) and (b) are schematic pictures for the sparse modeling and ℓ^2 norm regularization in a 2-D case, respectively. The blue ellipses represent the contours of the SSRs and the red diamond and circle represent the constraint of the ℓ^1 norm and ℓ^2 norm, respectively. The minimum point of the objective function (green star) is the intersection of the ellipse and the diamond/circle. In the case of sparse modeling, the diamond region is more likely to produce an intersection that has one component of the solution is zero. This is because diamonds are convex so that it is easier to intersect with an ellipse at an apex.

In the ℓ^1 norm regularization, the second term of the right-hand side of equation (4.6) is nondifferentiable. Therefore we use the Iterative Shrinkage Thresholding Algorithm (ISTA) [e.g., *Beck and Teboulle*, 2009] and minimize the objective function by repeating the following procedure:

$$\mathbf{m}_{k+1} = S_\gamma(\mathbf{m}_k - \gamma \nabla f(\mathbf{m}_k)). \tag{4.7}$$

$\mathbf{m}_k$ is the estimated model vector on the k-th iteration. f is the first term of the R-H-S of equation (4.6), and it is the differentiable function ($\nabla f(\mathbf{m}_k) = \mathbf{G}^T(\mathbf{G}\mathbf{m}_k - \mathbf{d})$). $\mathbf{m}_k - \gamma \nabla f(\mathbf{m}_k)$ (in the bracket of S_γ) is a gradient descent, and γ (>0) is a step size. The ISTA will converge when the step size $\gamma \in (0, 1/L]$ is used [e.g., *Parikh and Boyd*, 2013]. Here, L is a Lipschitz constant. A maximum eigenvalue of the matrix $\mathbf{G}^T\mathbf{G}$ is used as the Lipschitz constant L in the ISTA [e.g., *Beck and Teboulle*, 2010]. On the ISTA, most of the model parameters are kept to be zero due to the following soft-thresholding function (Figure 4.4 (c)):

$$S_\gamma(v) = \begin{cases} v - \gamma\lambda & , v \geq \gamma\lambda \\ 0 & , 0 < v < \gamma\lambda \end{cases} \tag{4.8}$$

where v is a real number. In this study, the initial model vector is set to zero-vector because we have no prior information about the spatial distribution of seismic scattering property changes. The model parameters are kept to be positive during iterations. The soft-thresholding function returns zero in the case of $0 < v < \gamma\lambda$. Accordingly, we can estimate a sparse model vector that minimizes equation (4.6).

4.3 Results

Before conducting imagings, we select decoherence values according to signal-to-noise ratios (SNRs) of CCFs. A Root-Mean-Square (RMS) amplitude of a CCF from -100 s to -90 s and +90 s and +100 s in lag times is defined as a noise level. A RMS amplitude of a CCF for each short time window is defined as a signal level. We only use decoherence values from time windows whose SNRs are larger than 1.5. In this study, we use 406 observed decoherence values. We divide the study area into 63 small cells with a size of $0.15° \times 0.15°$ and estimate Δg values for all small cells. Figure 4.5 (a) shows the estimated spatial distribution of Δg values using sparse modeling. The region with the largest Δg value is estimated at the south of the epicenter of the main shock, and its value is 0.032 km^{-1}

($\Delta g/g_0 = 97$ %). The red line in Figure 4.5 (b) represents estimated Δg values for the small cells. In this case, only 6 small cells have non-zero values, and this indicates that the sparse modeling works well. Figure 4.5 (c) shows observed and synthesized decoherence values for all station pairs and lag times. Synthesized decoherence values are calculated using the estimated model parameters and decorrelation kernels (equation (4.2)). Synthesized decoherences almost explain observed ones. As shown in equation (4.6), we consider both of the SSRs (data fitness) and the ℓ^1 norm (sparsity of the model), and the ℓ^1 norm term is weighted by a hyper-parameter λ. The value of λ affects estimated Δg values. The top panel of Figure 4.6 shows its effect: Pink lines on the top panel represent estimated Δg values for the small cells. The middle panel shows the numbers of non-zero model parameters. For a large λ, only sparsity of a model is considered, and accordingly all model parameters become zero or nearly equal zero. We determine the optimal value of λ by calculating the modified Bayesian information criterion (BIC) proposed by Wang and Leng [2009]:

$$BIC = \ln\left(\frac{SSR}{n}\right) + |S| \times \frac{\ln(n)}{n} \times \ln(\ln(p)). \tag{4.9}$$

Here, n is the number of the data, $|S|$ is the number of the non-zero model parameters (degree of freedom), and p is the number of the model parameters. The bottom panel of Figure 4.6 shows BIC for all λ. In our case, the BIC becomes the minimum for λ=6.3, and we use this value.

4.4 Discussions

4.4.1 Comparison with the results from the linear least-squares inversion with ℓ^2 norm regularization

We also estimate the spatial distribution of seismic scattering property changes from an ordinary linear least-squares inversion with the ℓ^2 norm regularization which has been widely used to solve linear inverse problems. In the case of the Iwate-Miyagi Nairiku earthquake, we have enough seismic stations. Therefore we can compare the results from the sparse modeling with those from the ℓ^2 norm regularization.

Figure 4.7 (a) shows the spatial distribution of Δg values. Here, we used the proximal gradient method to estimate the Δg values. The region of large Δg values is located around the epicenter of the main shock, and this result is well consistent with the result from the sparse modeling. The maximum Δg value is about 0.012 km^{-1} ($\Delta g/g_0 = 36$

%) at the small cell which is located to the south of the epicenter. Estimated Δg values from the ℓ^2 norm regularization are smaller than those from the sparse modeling: the maximum value of Δg from the ℓ^2 norm regularization is about 37 % of that from the sparse modeling. This is because the number of the small cell with non-zero values is 33 in the case of the ℓ^2 norm regularization (Figure 4.7 (b)). As shown in Figure 4.7 (c), the synthesized decoherence values roughly explain observed decoherence ones. However, the synthesized decoherences from the sparse modeling can better explain the observed ones, especially spiky-shaped parts. This can be because the estimated Δg value from the sparse modeling is more sharply large at the south of the epicenter than that from the ℓ^2 norm regularization.

As discussed in chapter 3, the regions of large seismic scattering property changes are well consistent with the regions of large slip and strong ground motion. Also, the crustal fluid will exist beneath the active volcano, and it can have caused the seismic scattering property changes. Moreover, landslides occurred around Kurikoma volcano associated with the earthquake. Such an area of material weakness can be related to the seismic scattering property changes.

4.4.2 Recovery tests

To check the reliability of our inversion results, we conduct recovery tests. Figure 4.8 (a) shows the input model of the recovery tests. We input Δg value of 0.033 km^{-1} ($\Delta g/g_0$=100 %) to only one small cell at the south of the epicenter. Input Δg values for the other small cells are zero. Firstly, we compute synthesized decoherence values for this input model using equation (4.2). The blue line in Figure 4.8 (b) represents the synthesize decoherence values. Secondary, we add noises to these synthesize decoherences:

$$dc_i^{syn'}(t) = dc_i^{syn}(t) + \varepsilon_i. \tag{4.10}$$

Here, $dc_i^{syn}(t)$ is the synthesized decoherence value from the input model for a station pair i. ε_i is the noise term and is sampled from a gaussian distribution $\varepsilon_i \sim N(0, \sigma_i^2)$, which is defined for each station pair. We compute coherence values between a RCCF and 10-days-stacked CCFs between Jan. 1 2017 and Jun. 13 2008 and calculate a variance of these coherence values for each station pair. We use 10 times variance as σ_i^2 for each station pair. The red line in Figure 4.8 (b) is an example of the synthesized decoherences with noise. Thirdly, we estimate a spatial distribution of Δg values using $dc_i^{syn'}(t)$ as input data. We repeat the same estimation for 50 times with changing $dc_i^{syn'}(t)$.

Figure 4.8 (c) shows the estimation results from sparse modeling. The input change region at the south of the epicenter is recovered. The Δg values shown in Figure 4.8 (c) are averaged for 50 estimations. The Δg value at the south of the epicenter is estimated to be 0.027±0.003 km^{-1}, and this value is 82 % of the input value (0.033 km^{-1}). Figure 4.8 (e) shows the histogram of estimated Δg values from the sparse modeling at the south of the epicenter. The red line represents the input Δg value at this small cell. The estimated Δg values are always smaller than the input value. The maximum and minimum value of estimated Δg values are 0.032 km^{-1} and 0.019 km^{-1}, respectively. Figure 4.8 (g) shows sum of estimated Δg values (blue line) and the number of non-zero model parameters (orange line) for all 50 estimations resulting from the sparse modeling. The sum of estimated Δg values are 0.034±0.002 km^{-1} on average, and this value is almost the same as the input value. Non-zero model parameters were estimated at 6 small cells on average, however, estimated Δg values at the other cells are significantly small compared to that of at the south of the epicenter.

Figure 4.8 (d) shows the estimation results from ℓ^2 norm regularization. The input change region at the south of the epicenter is also recovered. The mean Δg value at the south of the epicenter is estimated to be 0.025±0.003 km^{-1}, and this value is 76 % of the input value (0.033 km^{-1}). Figure 4.8 (f) shows the histogram of estimated Δg values from the ℓ^2 norm regularization at the south of the epicenter. Figure 4.8 (h) shows sum of estimated Δg values and the number of non-zero model parameters for all 50 estimations resulting from the ℓ^2 norm regularization. The sum of estimated Δg values are 0.039±0.002 km^{-1} on average, and this value is a bit larger than the input value. In the case of ℓ^2 norm regularization, non-zero model parameters were estimated at 12 small cells on average, and this will cause the overestimation of total estimated Δg value.

The results of the recovery tests indicates that our results, the region of large seismic scattering property changes is estimated at the south of the epicenter, should be reliable.

4.4.3 Applicability of sparse modeling

To validate the applicability of sparse modeling with a smaller data set, we estimate spatial distributions of seismic scattering property changes by changing combinations of used stations.

Firstly, we divide the study area into 4 regions around the epicenter and conduct estimations. Figure 4.9 shows the results. We use 4 different seismic arrays which are composed of seismic stations in the northern part (Array 1), southern part (Array 2), eastern part (Array 3), and western part (Array 4), respectively. Although large seismic

scattering property changes are estimated at the south of the epicenter for the Arrays 2 and 4, such change regions are not estimated for the Arrays 1 and 3. This should be because the Arrays 2 and 4 include station pairs which cross around the south of the epicenter. As shown in Figure 4.2, the station pairs of N.ICEH-N.NRKH (top panel) and N.OGCH-N.ICEH (second panel) which cross the south of the epicenter show significant decoherences related to the earthquake. On the other hand, the Arrays 1 and 3 are mainly composed of the station pairs which do not cross around the south of the epicenter. Most of these station pairs do not show significant decoherences related to the earthquake; For example, the station pairs of N.HMSH-N.SMTH (third panel in Figure 4.2) and N.OGCH-N.TAJH (bottom panel in Figure 4.2) do not show clear coherence drops. Those results indicate that we need station pairs which cross the south of the epicenter to detect the significant seismic scattering property change related to the Iwate-Miyagi Nairiku earthquake. We also conduct estimations using the same 4 seismic arrays and the ℓ^2 norm regularization. Figure 4.10 shows the results. In the case of the ℓ^2 norm regularization, the change regions at the south of the epicenter are not estimated significantly for all 4 arrays. Although both of the sparse modeling and ℓ^2 norm regularization cannot reproduce the results from all 17 stations by using those 4 seismic arrays, the results from the sparse modeling are slightly better than those from the ℓ^2 norm regularization.

Secondly, we use other arrays and check how many seismic stations are needed to reproduce the result from all 17 stations: The left-top panel of Figure 4.11 shows the result from 3 seismic stations close to the epicenter (Array 5). The result from this seismic array still cannot retrieve the result from all 17 stations. The right-top panel of Figure 4.11 shows the result from 5 seismic stations that are deployed to surround the epicenter at close range (Array 6). The large seismic scattering property change at the south of the epicenter is sharply retrieved for the Array 6, and the maximum value of Δg is the same as that from all 17 stations (0.032 km^{-1}). This suggests that if seismic stations are deployed to surround the change region and near the epicenter, we can retrieve the change region from only 5 stations in the case of the Iwate-Miyagi Nairiku earthquake. For comparison, we also conduct estimations using the ℓ^2 norm regularization. Figure 4.12 shows the estimation results. In the result from the Array 6, the maximum value of Δg is estimated to be 0.0075 km^{-1}. The result from all 17 stations is 0.012 km^{-1}, and hence 5 seismic stations are not enough to retrieve the result from all 17 stations in the case of the ℓ^2 norm regularization. When we use the ℓ^2 norm regularization, we need 15 stations to retrieve the result from all 17 stations (Array 9). The Arrays 7 and 8 are composed of 5 and 12 seismic stations that are located far from the epicenter, respectively. Although

there are some station pairs which cross around the change region at the south of the epicenter, no significant change region of seismic scattering property is estimated both in the cases of the sparse modeling and ℓ^2 norm regularization. Those results indicate that seismic stations near the change region are important to retrieve it, and this is not retrieved well from only seismic stations far from the change region even if station pairs cross around this region.

To confirm that, we compare sensitivity kernels for different inter-station distances. Figure 4.13 shows cross-sections of sensitivity kernels for inter-station distances of 30 km and 60 km. In this study, we compute decoherence values by sliding a 16 s long time window from 16 s after the direct Rayleigh wave arrival time to 64 s after the direct Rayleigh wave arrival time without overlapping. Decoherence values are calculated at later lapse times for station pairs with long inter-station distances. The two sensitivity kernels that are shown in Figure 4.13 are computed at a lapse time of 40 s after direct Rayleigh wave arrivals. As mentioned in the Data and method section, there are two peaks around the two stations, and this is the reason why seismic stations near the change region are important to retrieve the change region. As shown in Figure 4.13, the peak values of the two sensitivity kernels are not significantly different from each other. On the other hand, we can find that the values of the sensitivity kernels in the region between two stations are significantly different: That for the station pair with an inter-station distance of 30 km is about 1.7 times larger than that for the station pair with an inter-station distance of 60 km. This means that the station pair with a long inter-station distance is less sensitive to a seismic scattering property change in a region between two stations. Accordingly, for the estimation of the spatial distribution of Δg values using sensitivity kernels, it should be better to use seismic stations near the change region and station pairs with short inter-station distances. In other words, important data on the estimation is limited and the other data is redundant.

4.5 Conclusion

We used sparse modeling to estimate the spatial distribution of seismic scattering property changes and succeeded in detecting large coseismic seismic scattering property changes at the south of the epicenter of the 2008 Iwate-Miyagi Nairiku earthquake. The maximum value of Δg, a variation of scattering coefficient, at this region was estimated to be 0.032 km^{-1} ($\Delta g/g_0 = 97$ %). We also conducted the ordinary linear least-squares inversion with the ℓ^2 norm regularization. The result from the sparse modeling and that from the ℓ^2 norm regularization were consistent. Finally, we explored the applicability of

sparse modeling by reducing the number of seismic stations. We confirmed that we can retrieve the change regions from only 5 stations which are deployed to surround the change regions for this case. Moreover, we found that the station pairs with long inter-station distances do not strongly affect the estimation result even if these pairs cross around the change regions in short range. This is because the value of sensitivity kernels is small for a station pair with a long inter-station distance. This means that the important station pairs for the estimation are limited and the other pairs are redundant. The sparse modeling will be useful to estimate the spatial distribution of seismic scattering property changes from the small data set.

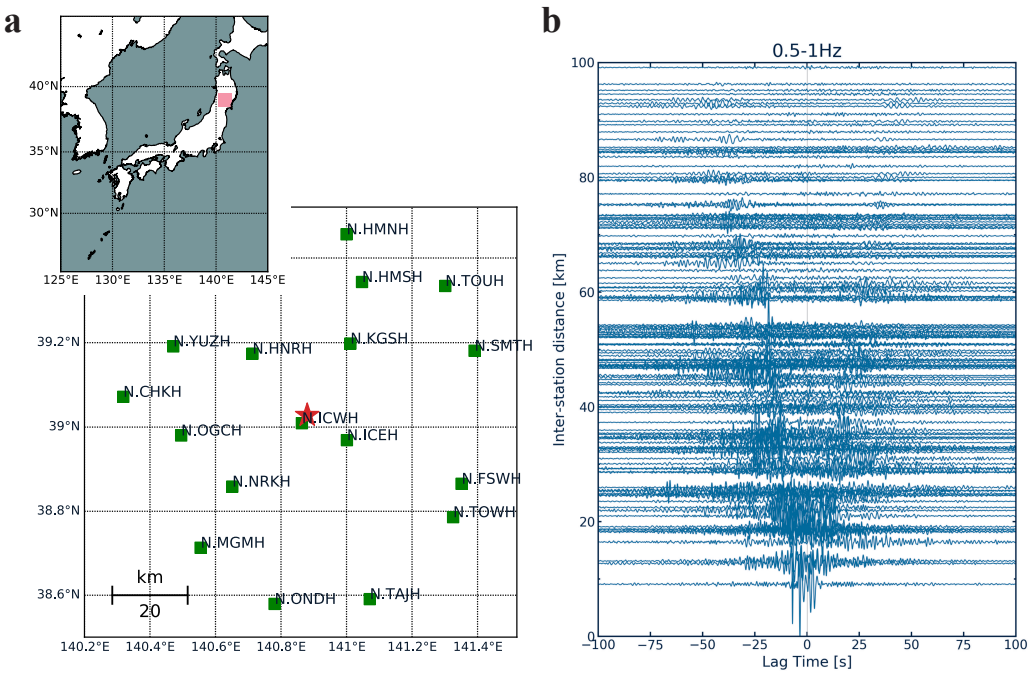

Figure 4.1 (a) Locations of 17 Hi-net stations (green squares) and the epicenter of the 2008 Iwate-Miyagi Nairiku earthquake (red star). (b) Record section of seismic ambient noise CCFs in the 0.5-1 Hz band. These CCFs are computed by stacking daily CCFs over 1 year in 2007.

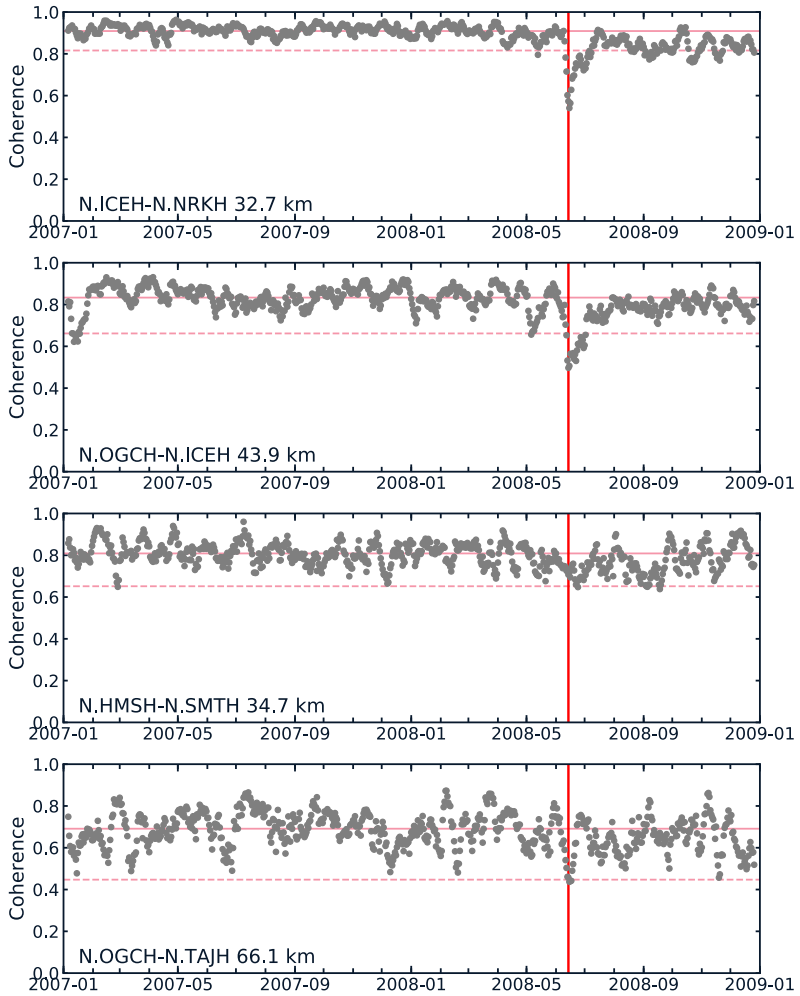

Figure 4.2 Temporal changes of coherences over 2 years for 4 station pairs of N.ICEH-N.NRKH (top), N.OGCH-N.ICEH (second), N.HMSH-N.SMTH (third), and N.OGCH-N.TAJH (bottom). Coherence values are computed between the CCF stacked over 1 year in 2007 and 10-days stacked CCFs by sliding 10-days-long time windows by 1 day. The red lines represent the date of the Iwate-Miyagi Nairiku earthquake. The pink solid lines represent mean coherence values before the earthquake (Jan. 1 2007 - Jun. 13 2008), and dashed ones represent the mean coherence minus three times standard deviations (3σ) of coherence values.

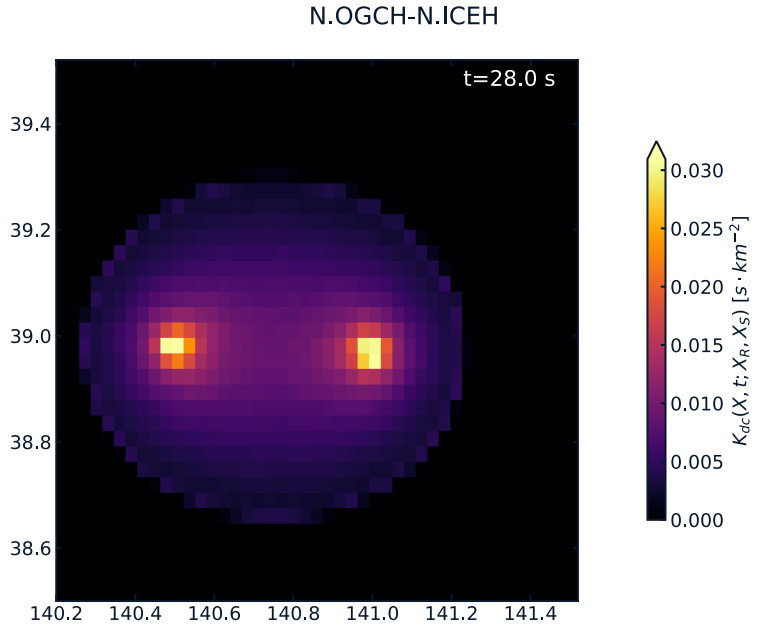

Figure 4.3 An example of the decorrelation kernel for the station pair of N.OGCH-N.ICHE at 28 s in lag time. The kernel is calculated assuming the scattering mean free path and intrinsic absorption parameter of Rayleigh wave to be 30 km and 0.02 s^{-1}, respectively. These parameters are estimated from envelopes of seismic ambient noise CCFs (see chapter 2).

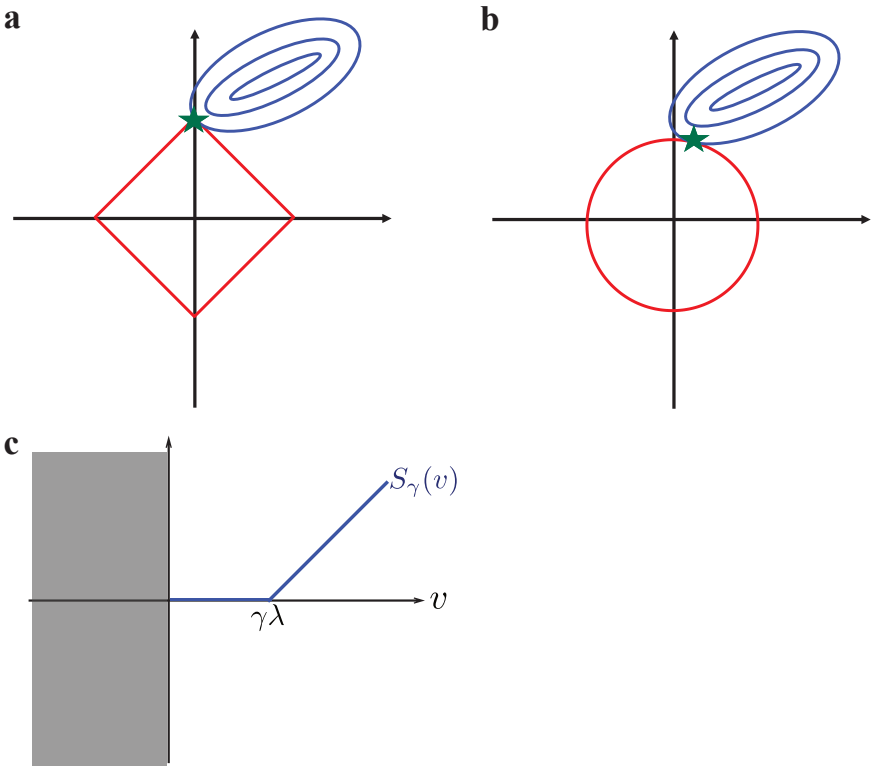

Figure 4.4 (a) Schematic picture for the sparse modeling. The red diamond represents ℓ^1 norm regularization term. The blue contours represent the sum of squared residuals. The green star is an optimal point. (b) That for the ℓ^2 norm regularization. The red circle represents ℓ^2 norm regularization term. (c) An example of the soft-thresholding function. $\gamma\lambda$ is a threshold value.

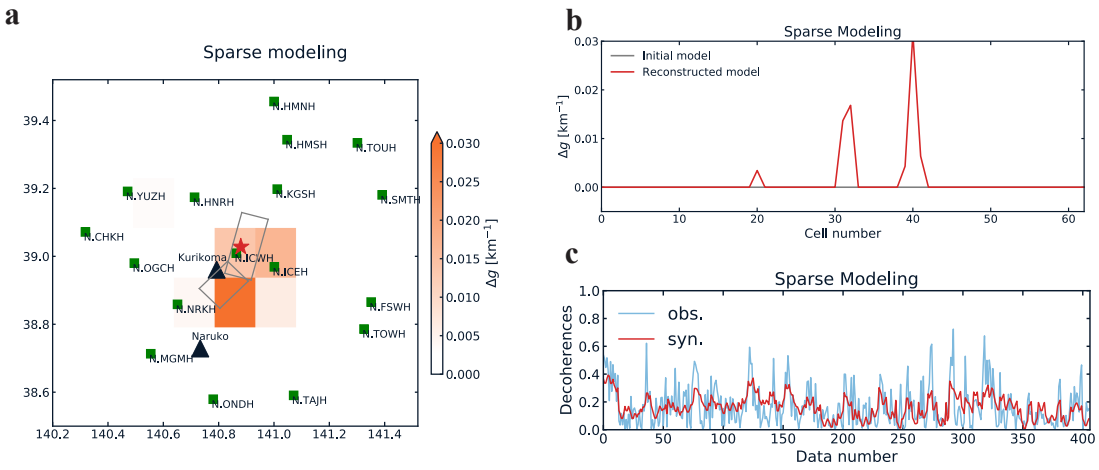

Figure 4.5 (a) Spatial distribution of Δg values inferred from the sparse modeling. The red star represents the epicenter. The two subfaults estimated by Ohta et al [2008] are shown by the gray rectangles. (b) The initial (gray) and estimated (red) models. All of the initial model parameters are fixed to zero. (c) Observed (blue) and synthesized (red) decoherence values for all station pairs and lag times.

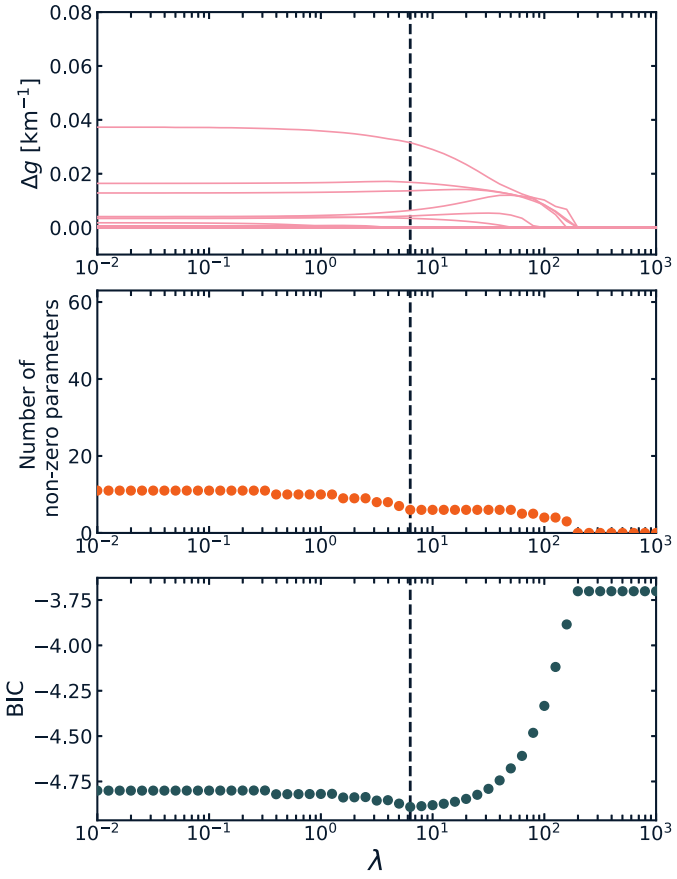

Figure 4.6 (top) Δg values for all small cells and λ. (middle) The number of non-zero estimated model parameters for each λ. (bottom) BIC values for each λ. The black dashed lines on each panel represent the value of λ with the minimum BIC.

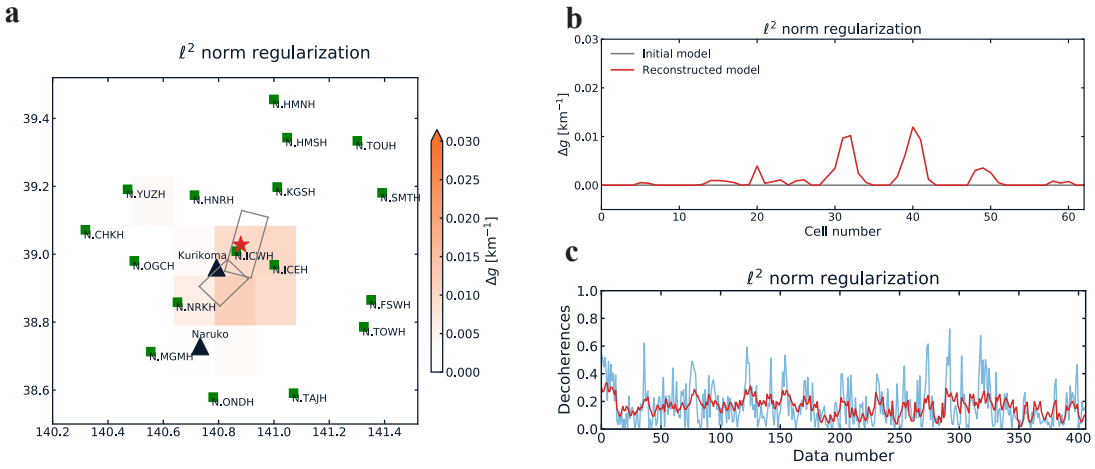

Figure 4.7 (a) Spatial distribution of Δg values inferred from the ℓ^2 norm regularization. (b) The initial (gray) and estimated (red) models. (c) Observed (blue) and synthesized (red) decoherence values for all station pairs and lag times.

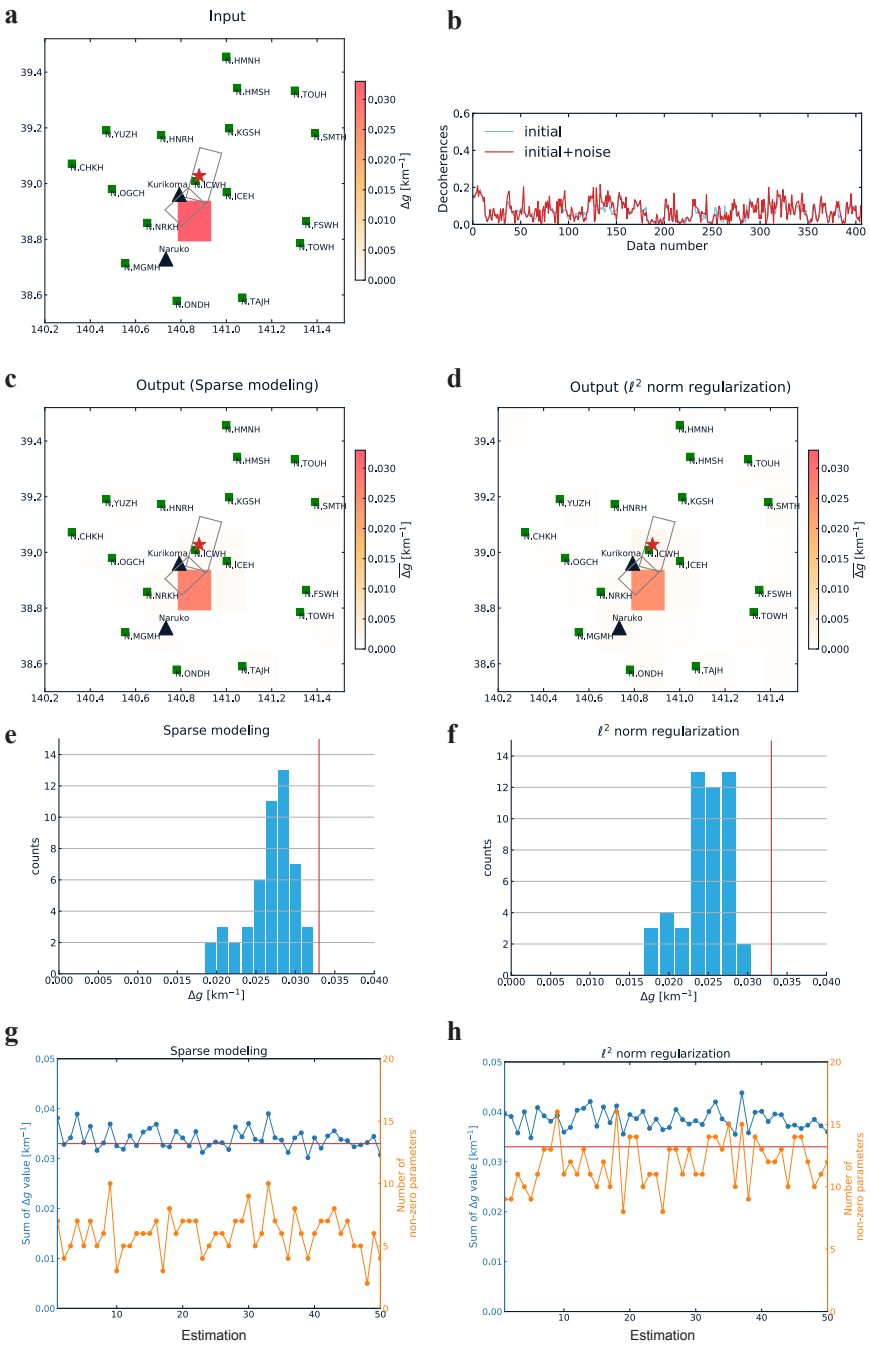

Figure 4.8 (a) Input model of the recovery tests. Δg value of 0.033 km^{-1} ($\Delta g/g_0$=100 %) is input to only one small cell at the south of the epicenter. Input Δg values for the other small cells are zero. (b) An example of synthesized decoherences. The blue line represents the decoherences calculated from the input model shown in (a). The red one represents the decoherences after adding noises to the blue one, and these decoherences are used in the recovery tests. (c) The result of the recovery tests using sparse modeling. Δg values shown in the figure are averaged for 50 estimations. (d) The result of the recovery tests using ℓ^2 norm regularization. (e) The histogram of estimated Δg values for the small cell at the south of the epicenter for 50 estimations with the sparse modeling. The red vertical line represents the input Δg value (0.033 km^{-1}) to this small cell. (f) Similar to (e) but from the ℓ^2 norm regularization. (g) Sum of estimated Δg values (blue) and the number of non-zero model parameters (orange) for all 50 estimations resulting from the sparse modeling. The red line represents input Δg value, 0.033 km^{-1}. (h) Similar to (g) but from the ℓ^2 norm regularization.

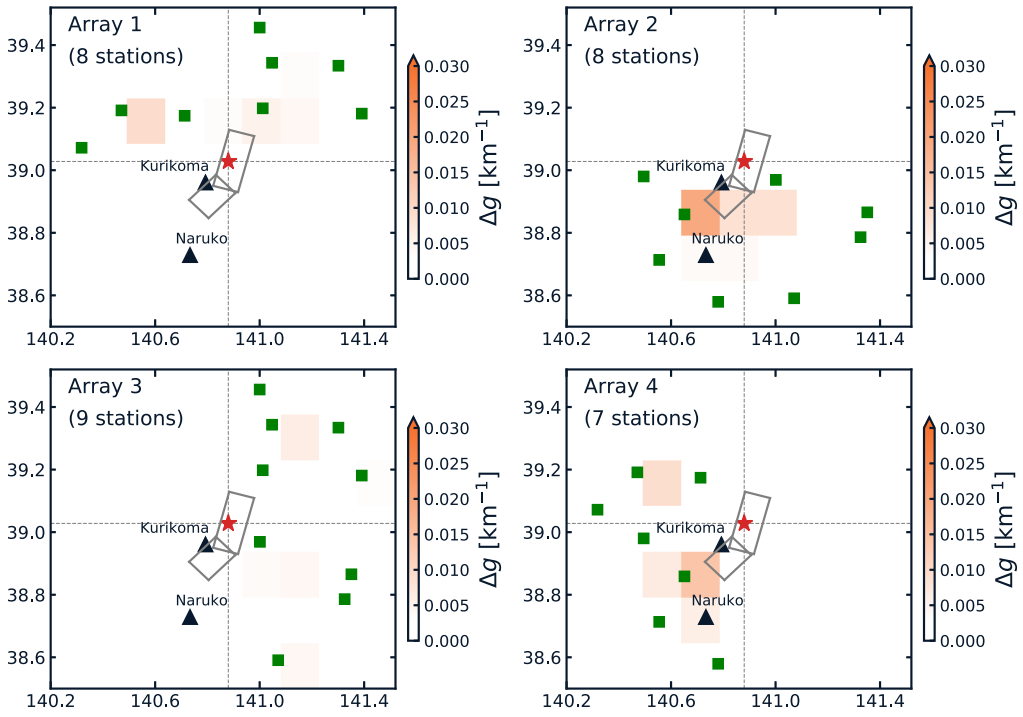

Figure 4.9 Spatial distributions of Δg values obtained for 4 different distributions of seismic stations using the sparse modeling. The study area is divided into 4 areas as indicated by vertical and horizontal dashed lines in each panel. Those 4 seismic arrays are composed of seismic stations in the northern part (Array 1), southern part (Array 2), eastern part (Array 3), and western part (Array 4), respectively.

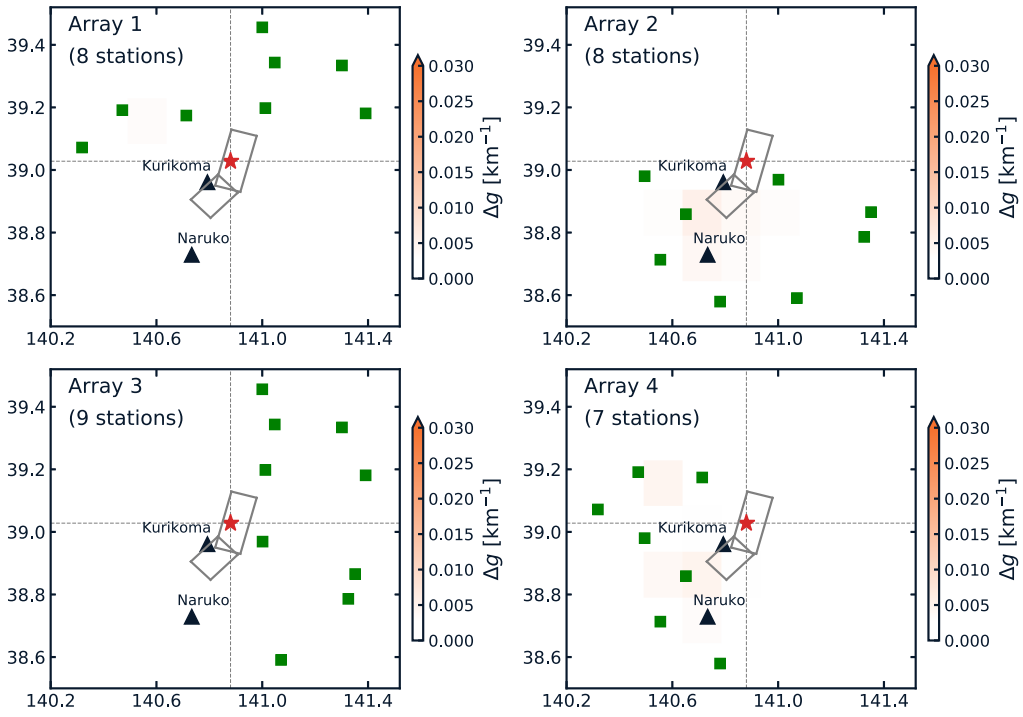

Figure 4.10 Similar to Figure 4.9 but from the ℓ^2 norm regularization.

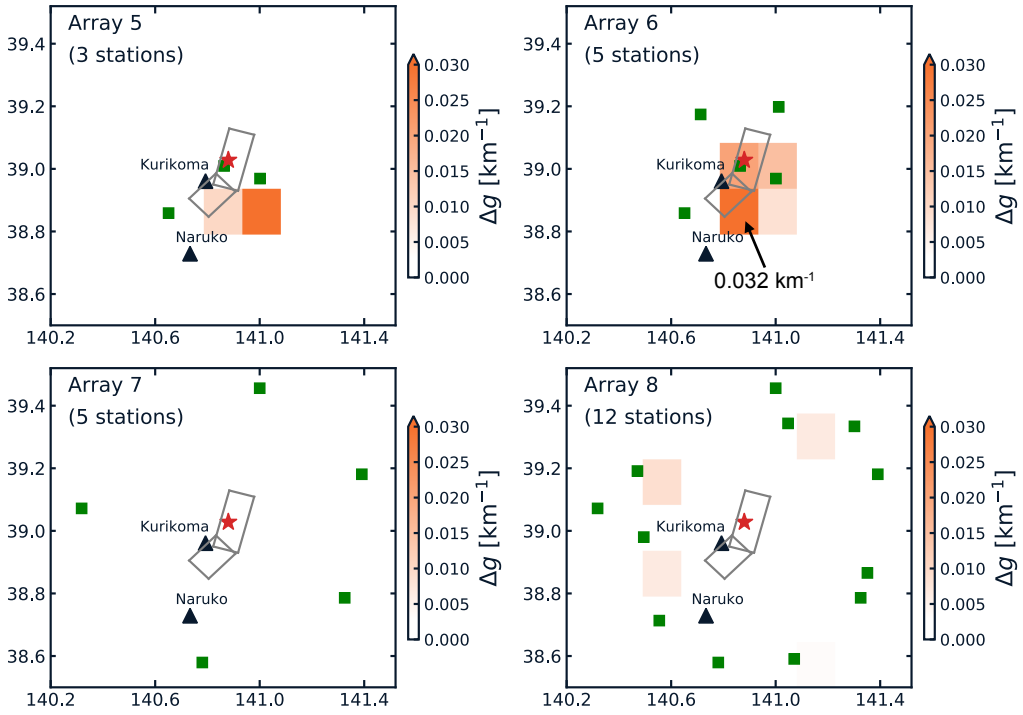

Figure 4.11 Spatial distributions of Δg values obtained for 4 different distributions of seismic stations (Arrays 5-8) using the sparse modeling. The Arrays 5 and 6 are composed of the three and five seismic stations closest to the epicenter, respectively. The Arrays 7 and 8 are composed of 5 and 12 seismic stations that are located far from the epicenter, respectively.

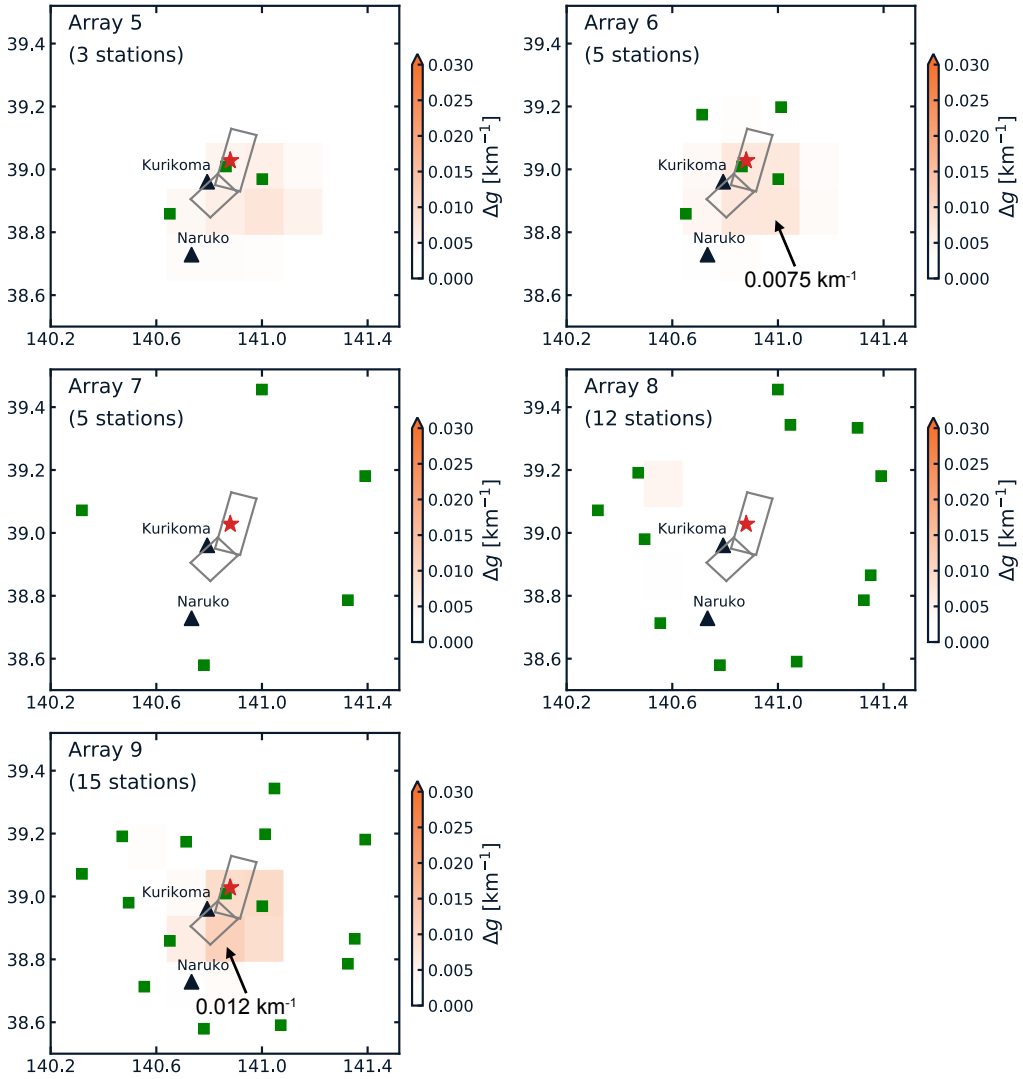

Figure 4.12 Similar to Figure 4.11 but from the ℓ^2 norm regularization. The Array 9 is composed of 15 seismic stations closest to the epicenter.

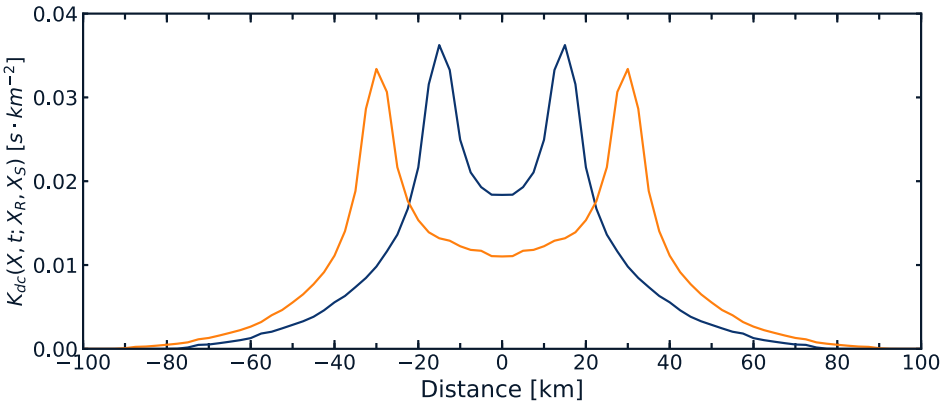

Figure 4.13 Examples of cross-sections of sensitivity kernels for 2 different inter-station distances. Blue and orange solid lines represent the kernels for the station pairs whose inter-station distance are 30 km and 60 km, respectively. They are calculated at a lapse time of 40 s after the direct Rayleigh wave arrivals.

Chapter 5

Time lapse imaging of seismic scattering properties in a strong scattering regime: Application to the 2015 dike intrusion event at Sakurajima volcano, Japan

5.1 Introduction

In recent years, spatio-temporal changes of seismic scattering properties associated with volcanic activities or earthquakes have been estimated from seismic interferometry analyses [e.g., *Obermann et al.*, 2013a; *Obermann et al.*, 2014; *Hillers et al.*, 2015; *Machacca et al.*, 2019]. We also estimated spatial distributions of seismic scattering property changes associated with the 2008 Iwate-Miyagi Nairiku earthquake and the 2011 Tohoku-Oki earthquake in chapters 3 and 4. Those analyses were conducted in weak scattering regimes: The values of the scattering mean free path, a parameter controlling sensitivity kernels, are fixed at 50 km in Obermann et al. [2013], 60 km (1-3 s period band) and 500 km (12-20 s period band) in Obermann et al. [2014], respectively. We used scattering mean free path of 100 km (0.125-1 Hz band) in chapter3 and 30 km (0.5-1 Hz band) in chapter 4. However, as mentioned in chapter 2, the scattering mean free path ranges from about a few hundred meters to a few kilometers at some active volcanoes. For example, Wegler and Lühr [2001] estimated the mean free path of S-waves at Merapi volcano, Java to be about 100 m in the 4-20 Hz band using airgun shot records. Yamamoto and Sato [2010] estimated the mean free path of S-waves in the 8-16 Hz band to be about 1 km using active shot records at Asama volcano, Japan. In chapter 2, we directly compared the values of the mean free path of Rayleigh waves that were obtained from envelopes of seismic ambient noise CCFs and active shot seismograms at Sakurajima volcano, Japan. The estimated values from both of the data were about 1.2-2.0 km at the 1-2 Hz band and 1.6-3.2 km at the 2-4 Hz band. These values are smaller by 1 to 3 orders than those of Earth's crust [*Sato et al.*, 2012]. As mentioned in chapter 1, we need to divide a study area into small cells whose size is smaller than a scattering mean free path for conducting a

linear least-squares inversion. For example, the number of the small cells in a region whose scattering mean free path is 1km will be 10 times larger than a region whose scattering mean free path is 1km. Therefore, more seismic stations are necessary for imagings in a multiple scattering regime.

Sakurajima is one of the most active volcanoes in Japan which is located at the southern rim of Aira caldera in the south of Kyushu, Japan. The volcano is well known to frequently erupt with Vulcanian style in these decades, and the volcanic activities have been monitored by various observations: seismic and geodetic measurements as well as volcanic gas observations [*Iguchi et al.*, 2013]. The explosions occurred mainly at Showa crater from 2012, and the annual numbers reached 835 in 2012, 883 in 2013 and 450 in 2014 [*Japan Meteorological Agency*, 2015].

A dike intrusion event took place on 15 August 2015 (around 11:00 local time) at Sakurajima. Noticeable changes of seismicity were detected just before the dike intrusion: Volcano-tectonic (VT) earthquakes started at about 7:00 local time. Moreover, significant changes of tilt and strain signals at stations located within a few kilometer distance from the active craters began around 8:00 local time [*Hotta et al.*, 2016a]. Geodetic analyses were conducted to estimate parameters of the dike. For example, Morishita et al. [2016] located the dike beneath Minami-dake crater at depths between 400-1200 m below sea level from analyses of interferometric synthetic aperture radar data. Hotta et al. [2016a] also analyzed GNSS and tilt data, and estimated parameters of the dike as follows: the length is 2.3 km, the width is 0.6 km, the strike is 34°, the dip is 74°, and the opening is 1.97 m.

In this study, we apply seismic interferometry to seismic ambient noise records at Sakurajima and estimate seismic scattering property changes associated with the dike intrusion event in 2015. The scattering mean free path estimated to be about a few kilometers as shown in chapter 2, and hence we need to consider multiple scatterings in locating change region of scattering property (hereafter, called change region). We firstly calculate temporal changes of coherence for each station pair. And then, we estimate parameters of the change region.

5.2 Data and method

5.2.1 Data processing

We use 6 three-component short-period (1 s) seismometers at Sakurajima that are operated by JMA (Figure 5.1). The sampled frequency is at 100 Hz. We apply seismic

interferometry to seismic ambient noise data on the vertical component for the period from 2012 to 2015. As mentioned in chapter 2, the scattering and intrinsic absorption parameters at Sakurajima were estimated in the 1-2 Hz band. Therefore, we use ambient noise records filtered in the 1-2 Hz band. We choose 10 minute-long data having the maximum amplitude of smaller than 10 times of the RMS amplitude of ambient seismic noise recorded in 2012. We apply one-bit normalization [e.g., *Larose et al.*, 2004] and spectral whitening [e.g., *Shapiro et al.*, 2006; *Bensen et al.*, 2007] for suppression of the influence of earthquakes and persistent monochromatic noise sources on seismic ambient noise CCFs. Finally, CCFs are calculated every 10 minutes and daily CCFs (hereafter called DCCFs) are obtained by stacking the 10-min CCFs every day for 15 station pairs from these 6 stations. The obtained DCCFs are considered to be the Green's function recorded at one of a station pair from a virtual source at the other station of the pair.

Waveforms of CCFs changed largely just before and after the dike intrusion. Figure 5.2 shows stacked CCFs for five periods in 2015 (from the top to bottom: Jan. 1 - Mar. 31, Apr. 1 - May 31, Jul. 6 - Aug. 14, Aug. 16 - Sep. 15, and Sep. 16 - Oct. 31) for station pairs V.SKRB-V.SKD2 and V.SFT2-V.SKRC which cross around the dike. The similarity of waveforms between the first and second periods (Jan. - Mar. and Apr. - May) are high for both station pairs. In contrast, we can see significant changes in the CCFs calculated after July 2015 at lapse times of, for example, around -10 s for both station pairs and around +12 s for V.SKRB-V.SKD2. Such large waveform changes from July 2015 suggest that seismic scattering property has already changed largely before the dike intrusion. Figure 5.3 (a) shows temporal changes of daily coherence values (black and grey circles) during 4 years for two station pairs of V.SKRB-V.SKD2 and V.SKRB-V.SKA2. We calculated reference CCFs (RCCFs) by stacking DCCFs in 2012 and 2013, and daily coherence values are calculated between RCCFs and DCCFs for the lag time range between -15.36 and +15.36 s. Red vertical lines indicate the time of the dike intrusion. Apparent decoherences due to some failure of a seismometer in V.SKRB was detected after the dike intrusion from November in 2015, and coherences in this period are shown by grey circles. Daily coherence values between January in 2012 and March in 2015 remain high (around 0.8) except for some time periods, and a gradual decoherence was detected from April in 2015. Such a gradual decoherence was detected for most of the station pairs, which suggest that a seismic scattering property change occurred widely at Sakurajima volcano. From July 2015, a larger decoherence took place especially for station pairs crossing around the dike, and such a large decoherence was not detected for the station pair of V.SKRB-V.SKA2 whose path does not cross around the dike. This means that seismic scattering

properties changed largely around the dike. Coherence values do not recover within 2015. Figure 5.3 (b) shows coherence matrixes of DCCFs between January 2012 and October 2015 for the same station pairs. For the station pair of V.SKRB-V.SKD2, coherences between DCCFs in Jul. - Oct. in 2015 are always lower than 0.7. This indicates that waveforms of DCCFs changed day by day.

5.2.2 Estimation method of parameters of a change region

In the 1-2 Hz band, the scattering mean free path and intrinsic absorption parameter of Rayleigh waves at Sakurajima were estimated to be 1.2 km and 0.10 s^{-1}, respectively, by modeling space-time distributions of seismic energy from an active shot as shown in chapter 2. As mentioned in chapter 1, the number of model parameters in the linear least-squares inversion increases in such a multiple scattering regime, because we need to divide the study area into small cells whose linear dimensions are smaller than the mean free path. Insteadly, we propose the following approach under multiple scattering regime: Firstly, we assume a change region with square-shape which is characterized by the following 4 parameters: length (km), location (Easting, Northing) (km), and Δg (km^{-1}). Here, g_0 is the scattering coefficient of the background medium that is equivalent to the reciprocal of the scattering mean free path ℓ, and Δg means a variation of the scattering coefficient. Then, the scattering coefficient in the change region is $g_0+\Delta g$. The details of parameter settings are shown in Table 5.1. Secondly, we apply Direct Simulation Monte Carlo method [*Yoshimoto*, 2000] to calculate seismogram envelopes before and after the change, respectively. The Monte Carlo simulations are performed in 2-D because we assume Rayleigh wave. The Rayleigh wave velocity is fixed at 1.15 km/s. In the Monte Carlo simulations, we calculate energy densities at each seismic station every 0.04 s between 0 s and 15.36 s in lapse time. Thirdly, we calculate synthesized decoherence values. The decoherence value is defined as [e.g., *Planès et al.*, 2014; *Margerin et al.*, 2016]:

$$dc^{syn}(t) \approx 1 - \frac{2\left\langle u_1(t)u_2(t)\right\rangle}{I_1(t)+I_2(t)} \approx \frac{\left\langle \left(u_2(t)-u_1(t)\right)^2 \right\rangle}{I_1(t)+I_2(t)}, \tag{5.1}$$

where $u_{1,\,(2)}$ represent the wavefield acquired in a reference and current periods, respectively. $I_{1,(2)}(t) = \left\langle u_{1,(2)}(t)^2 \right\rangle$ are energy densities in a reference and current periods, respectively. The brackets represents an ensemble average over a short time window whose center time is t. We compute decoherence values by using the following relationship [*Margerin et al.*, 2016]:

$$dc^{syn}(t) \approx \frac{\left|I_2(t) - I_1(t)\right|}{I_1(t) + I_2(t)}. \tag{5.2}$$

Finally, we determine the best-fit parameters of the change region so as to minimize the following objective function:

$$F = \sum_{i=1}^{N} \sum_{t} \left| dc_i^{obs}(t) - dc_i^{syn}(t) \right| + \alpha \left(1 - \frac{1}{N} \sum_{i=1}^{N} CC_i \right) \tag{5.3}$$

where $dc^{obs}(t)$ is the observed decoherence value, i is a combination of the source, the receiver, and positive or negative side of a CCF. N is its total number (N=30 in our case). The first term of equation (5.3) is a sum of absolute values of residuals between the observed and the modeled decoherences. We use ℓ^1 norm to reduce the effect of outliers. The second term is a constraint term which evaluates the similarity of time series of the observed and modeled decoherences. α is a weighting value, and CC_i is a correlation coefficient between time series of observed and modeled decoherences. By adding the constraint term, we can avoid the saturation of estimated values of the length. We search the best-fit model which minimizes F with changing α. The appropriate α is determined by a trade-off curve (L-curve) of the first term and the second term. We stack DCCFs over a reference and target periods, respectively, and calculate observed decoherence values $dc^{obs}(t)$ by sliding a 2.56 s long short time window by every 2.56 s between -15.36 s and 0 s and between 0 and +15.36 s in lag time. Obermann et al. [2016] calculated the lapse-time-dependence of energy partition ration between body waves and surface waves, and pointed out that surface waves were predominant until eight times the mean free time in lapse time. We hence use CCFs between -15.36 s and + 15.36 s in lag time to reduce the contamination of body waves. We do not calculate decoherence values before the direct Rayleigh wave arrival.

5.3 Results

We estimate the parameters of the change regions for four periods of time called Period I (Apr. 1 - May 31; reference period: Jan. 1 - Mar. 31), Period II (Jul. 6 - Aug. 14; Apr. 1 - Jul. 5), Period III (Aug. 16 - Sep. 15; Jul. 6 - Aug. 14), and Period IV (Sep. 16 - Oct. 31; Aug. 16 - Sep. 15). Reference CCFs are computed by stacking DCCFs over the reference periods. We checked daily coherence values and defined these four periods which do not include significant decoherences. The data on August 15

(the day of the dike intrusion) is not used to avoid a contamination by VT earthquakes. Figure 5.4 is a schematic illustration of Monte Carlo Simulations for each period. Each panel shows a spatial distribution of scattering coefficient. We assume that the scattering coefficient in the study area is spatially uniform (g_0) before Period I (top-left panel), and calculate energy density in the reference period $I_1(t)$. Energy density in the current period $I_2(t)$ is calculated by assuming that the scattering coefficient in a change region increases from g_0 to $g_0+\Delta g_1$ (bottom-left panel). We calculate synthesized decoherence $dc^{syn}(t)$ using $I_1(t)$ and $I_2(t)$, and estimate parameters of the change region in the Period I. In the Period II, energy density $I_1(t)$ is calculated with the change region estimated in the Period I. Energy density $I_2(t)$ is calculated with the change region in the Period I (scattering coefficient: $g_0+\Delta g_1$) and a new change region in the Period II (scattering coefficient: $g_0+\Delta g_2$) (bottom-center panel). Change regions in the Period II, Period III, and Period IV are estimated by repeating such procedures.

Figure 5.5 (a) shows temporal changes of coherences during these four periods for the station pair V.SKRB-V.SKD2. A gradual decoherence took place in the Period I, and coherence drops occurred from the Period II to Period IV. Figure 5.5 (b) shows an estimated change region for each period. The best-fit value of Δg is 0.25 km^{-1} in the Period I, and the change region extends widely around Kita-dake and Minami-dake. In the period II, the value of Δg increase to 1.10 km^{-1}, and it is significantly larger than that in the Period I. In the Period III, the size of the change region becomes a little smaller and that is located around the dike. The best-fit values of Δg is 2.45 km^{-1} in this period, which indicates that seismic scattering properties changed greatly associated with the dike intrusion. The value of Δg is estimated to be 1.55 km^{-1} in the Period IV, about 1-2 months after the dike intrusion. The best-fit parameters in respective periods are shown in Table 5.2.

We perform jackknife tests for estimating errors. Decoherence values are calculated for each station pair, the causal part of CCF, and the acausal part of CCF. Therefore there are 30 combinations (15 pairs $\times$ 2 parts) of the source and the receiver, and the part of CCF. In the jackknife tests, we estimated parameters of change regions using decoherence values for 29 combinations, and performed estimations 30 times with changing an unused combination. The ranges between 5 percentile and 95 percentile obtained from the jackknife tests are shown in the brackets in Table 5.2. The range of the length in the Period I and Period II are 4.0-4.5 km and 4.0-4.25 km, respectively. On the other hand, that becomes smaller, 3.0-3.5 km, in the Period III. This indicates that seismic scattering property changed widely at Sakurajima in the Period I and Period II, then located around

the dike in the Period III.

Figures 5.6 (a) and (b) show decoherence values at each lag time for 6 station pairs in the Period I and Period III, respectively. Blue and red circles represent observed and synthesized decoherence values, respectively. Closed and open circles represent decoherence values in the causal part and acausal part, respectively. The change region extends widely around Kita-dake and Minami-dake in the Period I, and observed and synthesized decoherence values are almost consistent with each other for many station pairs in this period. On the other hand, the change region becomes smaller and gets closer around the dike in the Period III. In this period, observed and synthesized decoherence values are almost consistent for the station pairs of V.SKRB-V.SKD2, V.SKA2-V.SKRD, and V.SFT2-V.SKD2, which cross around the change region. Calculations are a little smaller than observations, especially for the station pairs of V.SKRD-V.SKRC and V.SKRB-V.SKRC. These station pairs cross south or west of Sakurajima. In this study, we assume only one change region, however, we will be able to explain decoherence values for these station pairs by putting two or three more change regions west of Sakurajima.

5.4 Discussions

5.4.1 Forward modeling using prior information

We have assumed a square-shaped change region so far to reduce the number of model parameters. This is because the number of station pairs, 15 pairs in our case, is not enough to consider complicated models. In the case of Sakurajima, the geometries of the dike were estimated by geodetic analyses [*Morishita et al.*, 2016; *Hotta et al.*, 2016a]. Hence, observed and synthesized decoherences might match better by using the information about the geometry of the dike. Here, we conduct forward modeling as follows: We fix location and the azimuth of the rectangular change region to the center of the dike and 34°, which is the same as the strike of the dike. We change only 3 parameters: the length (km), width (km), and value of Δg (km^{-1}). The length should be always larger than the width.

Figure 5.7 (a) shows the best-fit model of the forward modeling in the Period III. The length, width, and Δg of the best-fit model are 4.5 km, 3.5 km, and 2.2 km^{-1}, respectively. The sum of absolute values of residuals for the best-fit model is 26.26 and the mean value of the correlation coefficient between the observed and modeled decoherences is 0.10. Those of the best-fit model with the square-shaped change region are 27.56 and 0.21, respectively. The Akaike's Information Criterions (AICs) for the rectangular change region and the square-shaped change region are 175.86 and 180.91, respectively.

Therefore the rectangular change region is considered as a better model. Figure 5.7 (b) shows observed and synthesized decoherence values for 6 station pairs shown in Figure 5.6. The rectangular change region can explain observed decoherences for the station pair of V.SKRD-V.SKRC crossing the south of Sakurajima, because the change region extends to the south of Sakurajima. This makes the sum of the absolute value of the residuals smaller than that of the square-shaped change region. This result suggests that the region where seismic scattering property changed distributes widely North-South along the dike. On the other hand, we cannot explain observed decoherence values for the station pair V.SKRB-V.SKRC, which crosses the west of Sakurajima, even if we assume the rectangular change region.

Although the observed and synthesized decoherences do not match well for some station pairs, the sum of the absolute value of residuals for all station pairs is reduced by assuming the rectangular change region which considers the geometry of the dike. Such prior information is important for the imaging of the change region in the case that the number of seismometers is not enough to constrain complex models.

5.4.2 Comparison with other observations

Seismic scattering is sensitive to a structural change whose scale is comparable to a wavelength. To understand mechanisms of temporal changes of decoherences, we compare them with seismic velocity changes, areal strain changes, and SO_2 flux changes. Figures 5.8 (a) and (b) show temporal changes of coherences and relative seismic velocities (dv/v) for a station pair of V.SKRB-VSKD2, respectively. We use Moving Window Cross-Spectral technique [*Poupinet et al.*, 1984] to compute relative velocity changes. Delay times are calculated by sliding a 2.56 s long short time window by every 0.64 s. Reference CCFs are computed by stacking DCCFs over 2012 and 2013, and DCCFs in lag times between -10 and +10 s are used for the linear regression. Coherence values outside of this time window are not high, hence we use this lag time range for the measurement of velocity changes. Seismic velocities keep decreasing between January and June 2015. On the other hand, we cannot estimate values of relative velocity changes stably due to large decoherences after July 2015, and they are shown by gray dots. Although Obermann et al. [2013a] and Obermann et al. [2014] estimated spatio-temporal changes both of seismic velocity and scattering property, we could not estimate velocity changes stably from one month before the dike intrusion. This indicates that measuring not only seismic velocity but also scattering property changes is important for monitoring. Figure 5.8 (c) shows areal strain changes at Sakurajima. We use three GNSS stations of Geospatial Information Authority

of Japan (GSI) at Sakurajima (blue circles in Figure 5.1 indicate these locations). Using the daily coordinates of the three stations (Sakurajima, Kagoshima2, and Kagoshima3), we calculate areal strains. In the calculation, we remove offsets in the daily coordinates due to the replacement of GNSS antennas at Kagoshima2 and Kagoshima3 on October 26, 2012, by using the difference between the median values calculated from 10 days before and 10 days after the day of the antenna change. The areal strain of zero amplitude is set to be the average value during the three years between 2012 and 2014. Note that we apply a median filter with a time window length of 10 days to the data to remove outliers. Areal strains show periodic fluctuations between 2012 and 2014 and an expansion from January 2015. The expansion from January 2015 is interpreted to be caused by an increase of magma supply from the deeper magma chamber located to the north of Sakurajima to the shallower magma chamber beneath Kita-dake [*Hotta et al.*, 2016b]. The seismic velocity decrease starting from January 2015 is well correlated with this expansion. We calculate standard deviations of areal strain values between 2012 and 2014, and red dash lines in Figure 5.8 (c) indicate $\pm 3\sigma$ of areal strain changes. Areal strain values become larger than $+3\sigma$ from April or May 2015. Such a substantial expansion might have opened cracks at the shallow part of Sakurajima. According to JMA, [2016], SO_2 flux from Minami-dake crater remains high between January and June 2015: daily SO_2 flux was ranging between 400 tons and 5,400 tons during this period. In 2014, the range of daily SO_2 flux was about 800-2,000 tons. Such a high SO_2 flux means that volcanic gas moved to the shallow part of Sakurajima during January and June 2015. As mentioned above, the significant expansion was detected by geodetic analysis in this period. Hence, the inflow of volcanic gas to opened cracks might have caused the gradual decoherences from April to June 2015.

We detected strong decoherences from July 2015, however, there are no significant areal strain changes in July 2015. SO_2 flux becomes small from July 2015, and it should be because the number of eruptions itself becomes small from July 2015; 241 in April, 244 in May, 103 in June, 21 in July, and 6 in August. The change region of seismic scattering property is located around the dike just after the dike intrusion. The penetration depth (quarter wave length) of Rayleigh waves in the 1-2 Hz band at Sakurajima is about 300 m. Although there are no other observations which detected significant changes from July 2015, our results indicate that some structural changes whose scale was comparable to a wavelength took place around the dike at depths shallower than about 300 m.

5.4.3 Imaging of scattering property changes in a multiple scattering regime

5.4.3.1 Asymmetry of decoherence values between causal and acausal parts

As shown in Figure 5.6 and Figure 5.7 (b), decoherence values on the causal and acausal parts calculated using equation (5.2) are not the same. Decoherence values become large if the change region is located near the source. In the Monte Carlo simulation, more energy particles radiated from the source are affected by scattering coefficient variation with space when a source is located near the change region. In contrast, if the change region locates far from the source, fewer energetic particles are affected by the scattering property change. We confirm it by conducting Monte Carlo simulations assuming the change region whose parameters are the same as those in the Period III. We divide the studied area into 1 km $\times$ 1 km cells and calculate spatial distributions of energies before and after the scattering property change, respectively: we count the number of energetic particles that exist in each cell for some time windows. Figures 5.9 (a) and (b) show spatial distributions of energy densities in 4 time windows (5.12-7.68 s, 7.68-10.24 s, 10.24-12.8 s, and 12.8-15.36 s), which are used to calculate decoherence values in this study. Regions where energy density decreases and increases associated with the scattering property change are shown by blue and red, respectively. In Figure 5.9 (a), V.SFT2 and V.SKRC are assumed as the source and receiver, respectively, and in Figure 5.9 (b), V.SKRC and V.SFT2 are assumed as the source and receiver, respectively. A blue rectangle on each panel in Figure 5.9 indicates the change region in the Period III. V.SFT2 is located near the change region and V.SKRC is located far from the change region. We can confirm that the regions with a large difference of energy densities (large $\left|I_2(t) - I_1(t)\right|$ in equation (5.2)) extend widely when V.SFT2 is the source. When the change region locates near V.SFT2, fewer energy particles radiated from V.SFT2 reach the receiver V.SKRC through the change region due to multiple scattering in the change region. As a result, energy densities decrease to the south of the change region and increase to the north of the change region. In contrast, we cannot recognize such a widespread difference of substantial energy density when V.SKRC is the source. This is because energy particles radiated from V.SKRC can reach V.SFT2 by going around outside the change region. As shown in Figure 5.6, decoherences are more significant when V.SFT2 is the source and V.SKRC is the receiver. An asymmetry of decoherence values is originally from a spatial variation in the scattering property, but it is enhanced in a multiple scattering regime, and it contains information about the relationship between the location of a change region and the locations of a source and a

receiver.

5.4.3.2 Limitation of our method

In chapter 2, we estimated scattering mean free paths at Sakurajima assuming that they are spatially uniform. Therefore, there is no prior information about the spatial variation of the scattering coefficient at Sakurajima so far. Therefore on the estimation of the change region in the Period I, we assumed that the scattering coefficient in the study area is spatially uniform and calculated energy density $I_1(t)$. However, Prudencio et al. [2017] estimated spatial distributions of scattering coefficient of S-waves (4-20 Hz band) using active shot records at Asama volcano, Japan, and they reported that the scattering coefficient in the area west of the summit is about 70 % higher than the mean scattering coefficient over the study area. Sakurajima is one of the most active volcanoes in Japan, and such a large spatial variation of the scattering coefficient may exist. For more reliable estimation of a change region, prior information about the spatial distribution of the scattering coefficient would be needed.

Another limitation of our method is the calculation cost of Monte Carlo simulations. In this study, we calculated energy densities $I_1(t)$ and $I_2(t)$ for two periods, and that increases the calculation cost. Accordingly it is hard to assume multiple change regions due to the high calculation cost. The necessary time for conducting the Monte Carlo simulation for one model is about 90 sec with the parallel computing using 4 CPU cores, and we conducted this computation for 7200 models with one change region. If we assume multiple change regions simultaneously, the necessary time for the calculations should increase significantly and our approach will not be practical: if we assume two change regions simultaneously, we need to conduct Monte Carlo simulations for more than 10^7 models.

Although sensitivity kernels are necessary in linear least-squares inversions, the calculation cost of sensitivity kernels is much lower than our approach; we do not need to conduct many Monte Carlo simulations. The values of Δg are estimated for the small cells, and hence we can easily consider plural change regions. Moreover, we can reduce a calculation cost by using sensitivity kernels. The linear least-squares inversions have such advantages, however, our method is also applicable even in the case that the number of seismic stations are not enough to conduct the linear least-squares inversion.

5.5 Conclusion

We proposed a method to estimate a region where seismic scattering property changed in a multiple scattering regime. We firstly calculated seismic ambient noise CCFs using seismic ambient noise data between 2012 and 2015 at Sakurajima, and succeeded in detecting a gradual decoherence between April and June in 2015 and a sharp coherence drop about one and half month before the dike intrusion on 15 August 2015. We secondly estimate the change regions of seismic scattering property. In previous studies, an inverse problem is linearized by assuming the scattering property changes affect the scattering only once. Hence, we proposed another method for estimating parameters of the change region which is also applicable in a multiple scattering regime. We assumed a square-shaped change region, and estimated its length, location, and variation of the scattering coefficient, Δg. The estimated change region extended widely around Kita-dake and Minami-dake with 0.25 km^{-1} and 1.10 km^{-1} of Δg in the Period I (Apr. 1 - May 31) and Period II (Jul. 6 - Aug. 14). The change region was located around the dike (east to Minami-dake) with 2.45 km^{-1} and Δg in the Period III (Aug. 16 - Sep. 15). In the Period IV (Sep. 16 - Oct. 31), the value of Δg decreased to 1.55 km^{-1} and the change region extended widely such as the Period I and Period II. Our method is applicable even in such a strong scattering case though the number of the change region is only one. This method should be useful for the continuous monitoring of structural changes beneath active volcanoes.

Table 5.1 Parameters used in the estimation of a change region of scattering coefficient. The origin of a coordinate is fixed at the center of the dike estimated by Hotta et al. [2016a].

Parameters	Search range	Increment
Length (km)	0.5 - 5.5	0.5
Easting (km)	-2.0 - +2.0	0.5
Northing (km)	-1.0 - +1.0	0.5
Δg (km^{-1})	0.0005 - 2.9005	0.05

Table 5.2 Best-fit parameters of the change region of scattering coefficient in each period. The values in brackets are the ranges between 5 percentile and 95 percentile obtained by the jackknife test.

Period	Length (km)	Easting (km)	Northing (km)	Δg (km^{-1})
Period I	4.5 (4.0 - 4.5)	+0.5 (+0.5)	+0.5 (+0.5 - +1.0)	0.25 (0.20 - 0.25)
Period II	4.0 (4.0 - 4.25)	0.0 (0.0)	0.0 (-0.25 - 0.0)	1.10 (1.05 - 1.10)
Period III	3.5 (3.0 - 3.5)	0.0 (0.0 - +1.0)	+1.0 (+0.5 - +1.0)	2.45 (2.05 - 2.45)
Period IV	4.5 (2.75 - 4.5)	-0.5 (0.0 - +1.0)	+0.5 (-0.5 - +1.0)	1.55 (1.15 - 1.55)

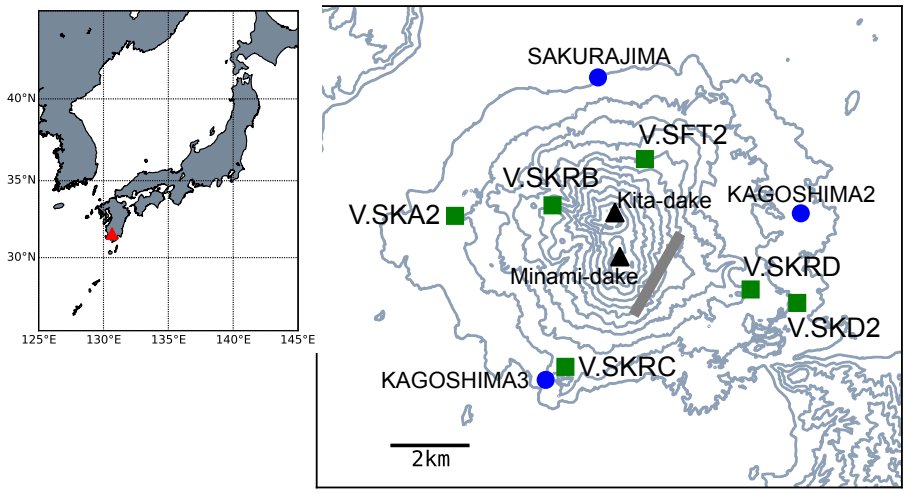

Figure 5.1 Spatial distribution of seismometers (green squares) and GNSS stations (blue circles) at Sakurajima volcano located in Kyushu island, Southwestern Japan (red triangle in the upper left panel). Gray contour lines show the topography of Sakurajima. The gray rectangle indicates the dike estimated by Hotta et al. [2016].

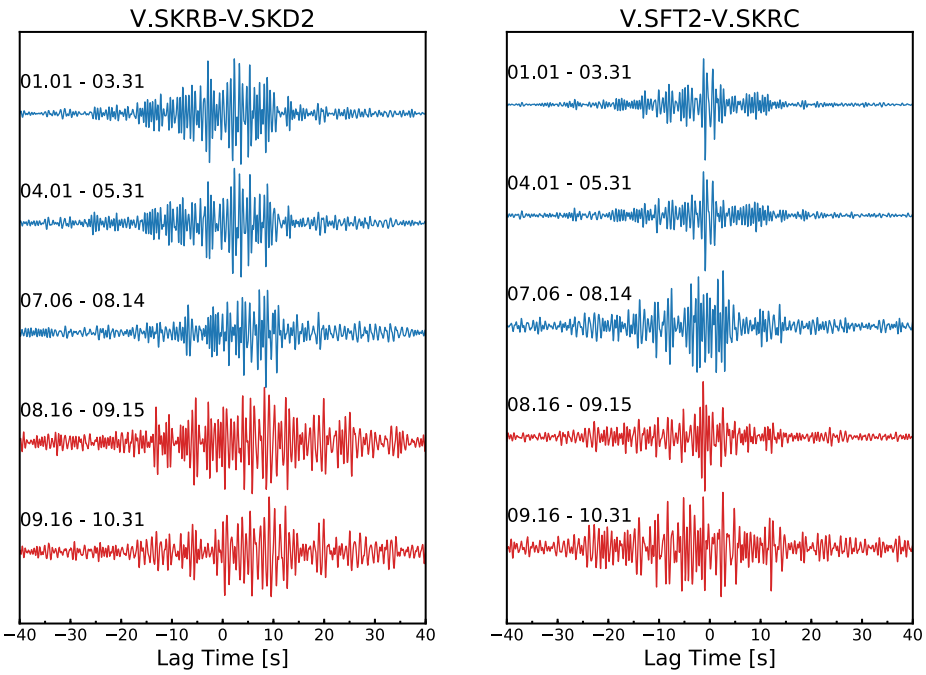

Figure 5.2 Waveforms of CCFs in 5 time periods of 2015 for 2 station pairs. Waveforms on the top are stacked CCFs from January to March, and those on the second row are ones in April and May. Waveforms from the third to fifth rows are stacked CCFs in periods just before and after the dike intrusion, respectively. In our analysis, CCFs between -15.36 s and +15.36 s in lag times are used.

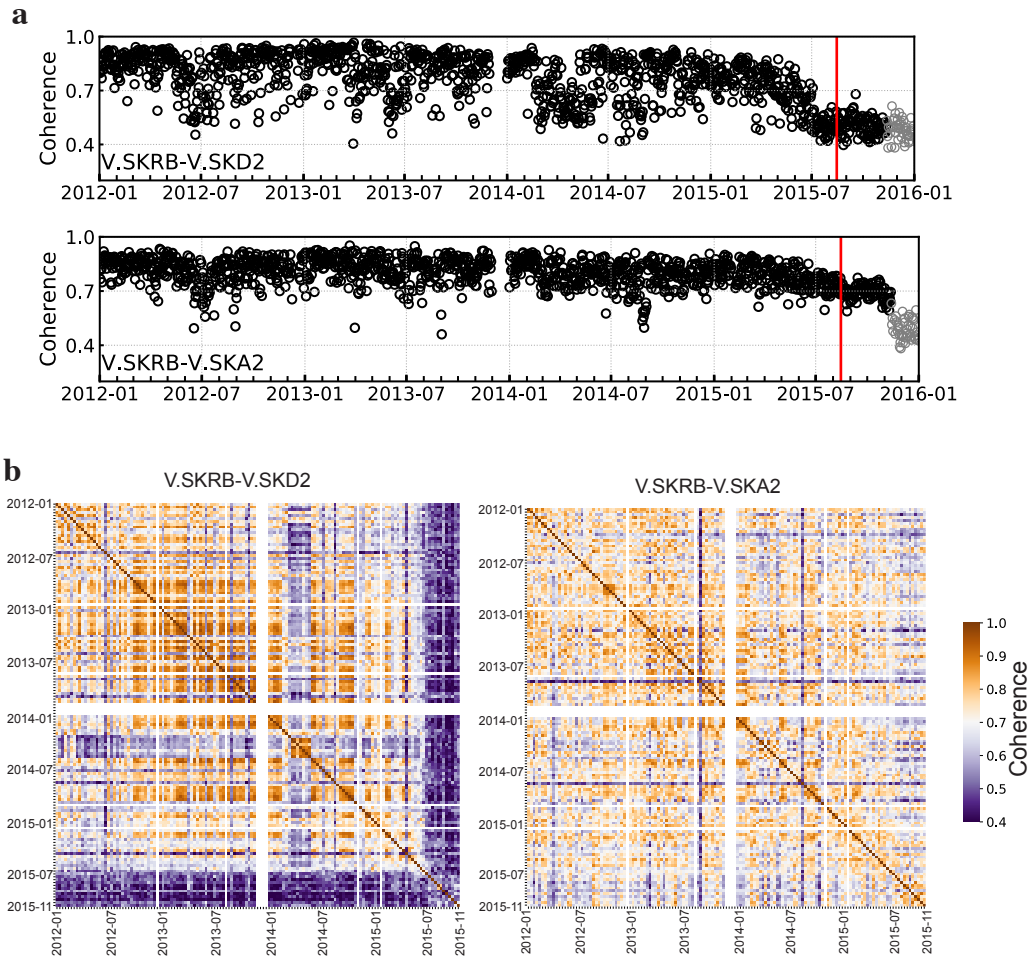

Figure 5.3 (a) Temporal changes of daily coherences for the station pairs of V.SKRB-V.SKD2 and V.SKRB-V.SKA2 between 2012 and 2015 (4 years). Black and grey circles indicate daily coherences which are computed between the RCCF and DCCF. Red vertical lines indicate the time of the dike intrusion. A seismometer failure occurred at V.SKRB between November 13 and December 31, 2015, and gray circles show daily coherences in this period. (b) The matrixes of coherences of DCCFs for the station pairs of V.SKRB-V.SKD2 and V.SKRB-V.SKA2. Coherences are calculated every 10 days for the time period between January 2012 and October 2015.

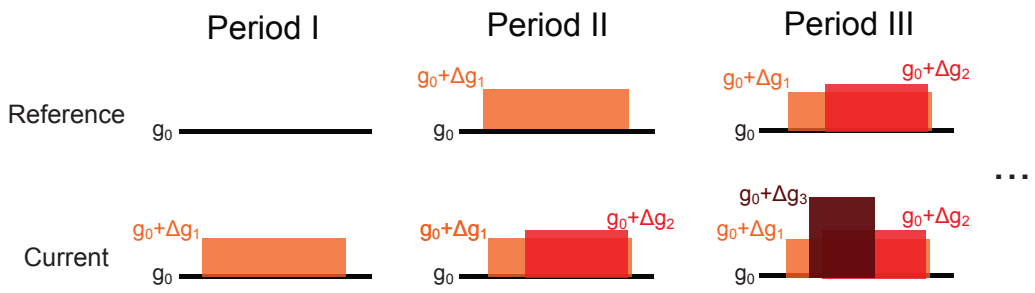

Figure 5.4 Schematic illustration of Monte Carlo Simulations in each period. Top three panels indicate spatial distributions of scattering coefficient in reference periods, and energy densities $I_1(t)$ in equation (5.1) are calculated under these conditions. Bottom three panels indicate those in current periods, and energy densities $I_2(t)$ in equation (5.1) are calculated under these conditions.

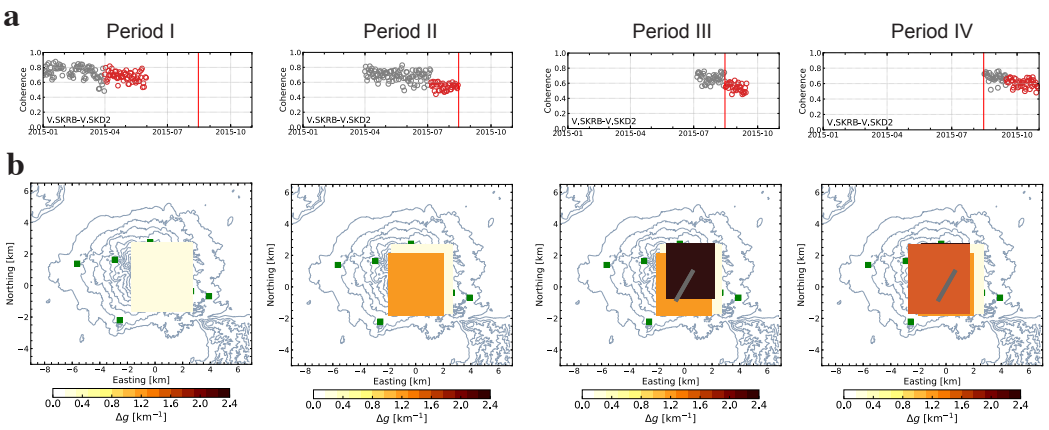

Figure 5.5 (a) Temporal changes of daily coherence values during 4 time periods. Gray circles show coherences in reference periods, and red circles show those in current time periods. Red vertical lines indicate the time of the dike intrusion. (b) Locations of the change regions of scattering property in each time period. Color of each square indicates the Δg value.

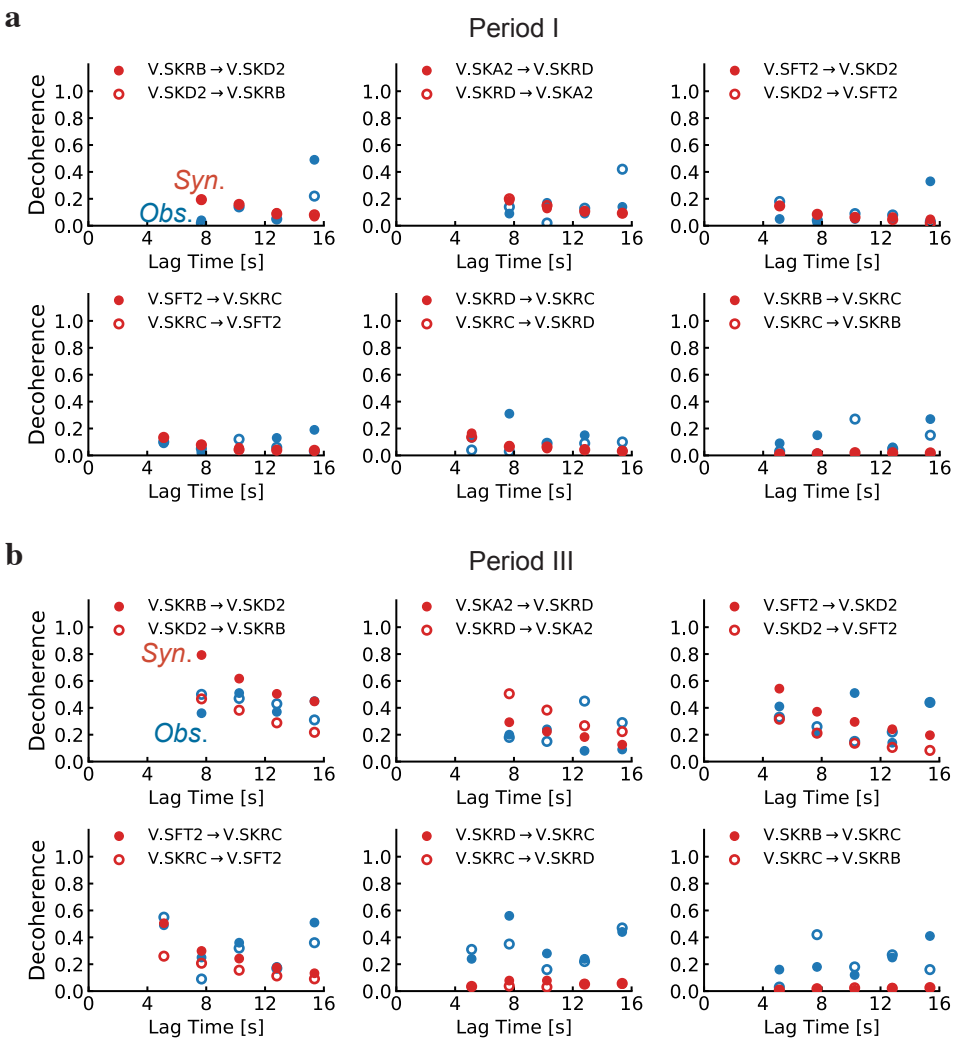

Figure 5.6 Decoherence values at each lag time for 6 station pairs. Blue and red indicate observed and synthesized decoherences, respectively. Decoherence values on the causal part and on the acausal part are shown by closed and open circles, respectively. Observed decoherence values are calculated by sliding a 2.56 s long short time window by every 2.56 s after the direct Rayleigh wave arrival.

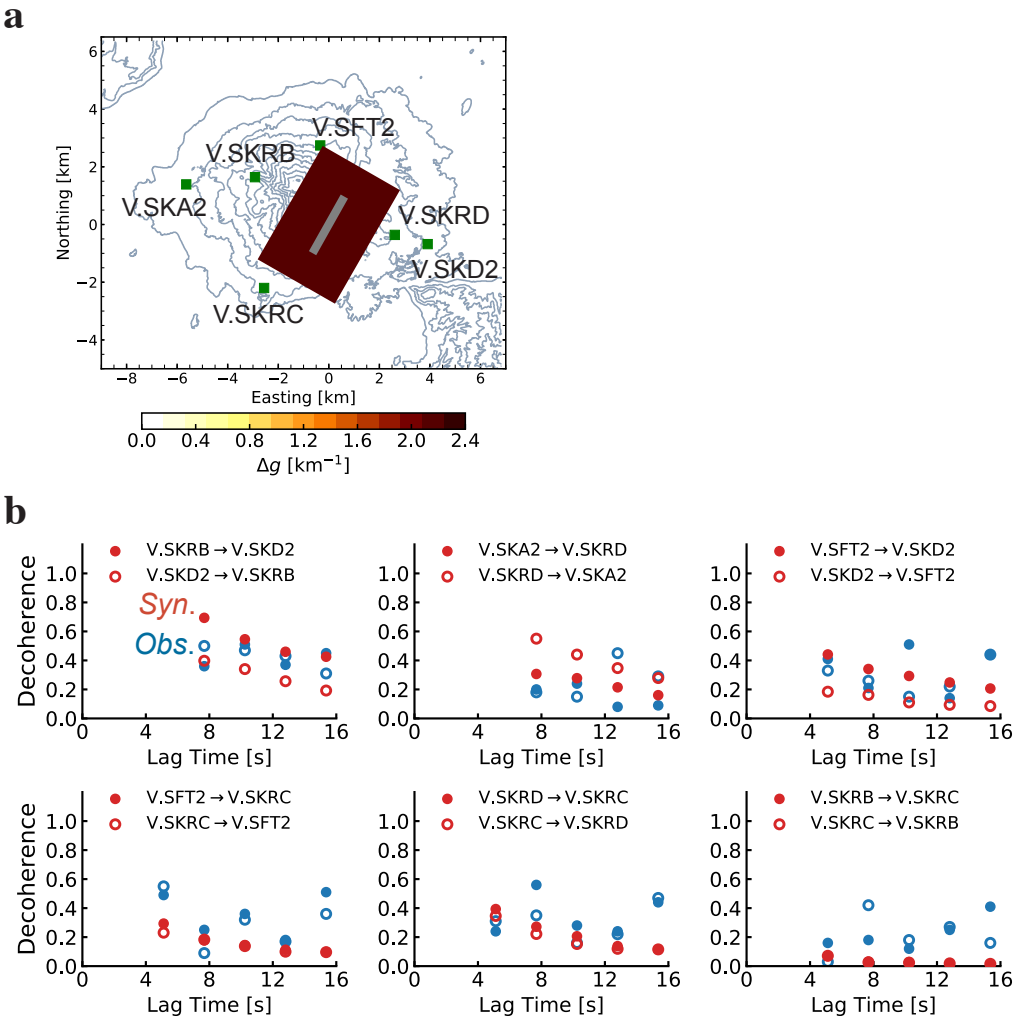

Figure 5.7 (a) The best-fit model with the location and azimuth of the rectangular change region fixed to the center of the dike and along the strike of the dike. In the grid-search, the length, width, and value of Δ g were changed. The gray rectangle indicates the dike. (b) Decoherence values at each lag time for 6 station pairs which are the same as shown in Figure 5.6.

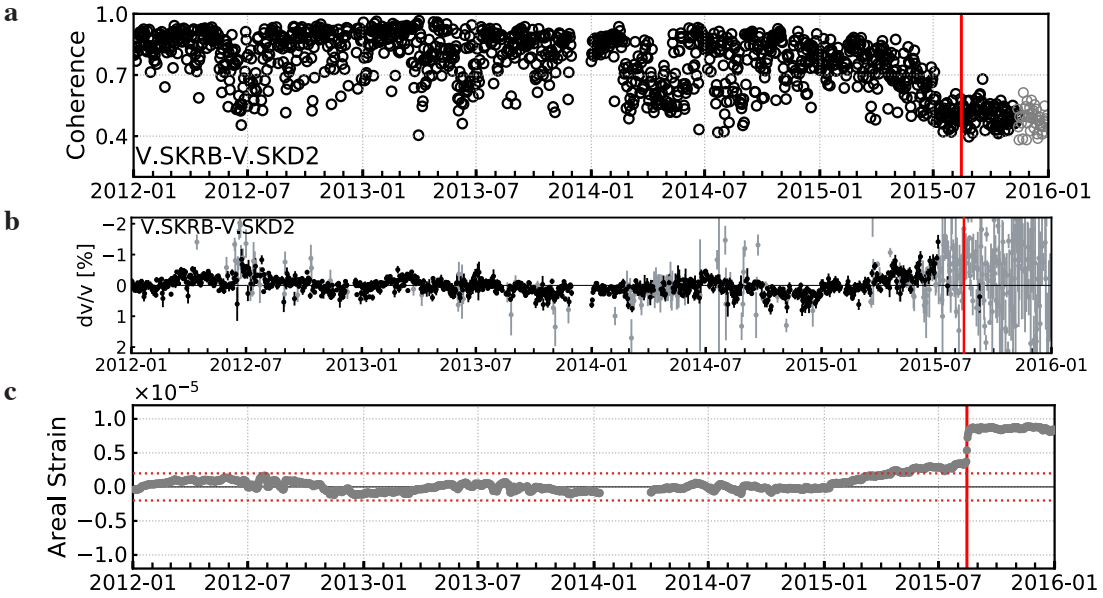

Figure 5.8 (a) Temporal changes of daily coherences for the station pair of V.SKRB-V.SKD2 between 2012 and 2015. (b) Temporal changes of relative velocities for the station pair V.SKRB-V.SKD2 between 2012 and 2015. These values are estimated using Moving Window Cross-Spectral technique [*Poupinet et al.*, 1984] and the linear regression. Gray dots represent that estimated velocity changes are not reliable because coherences are too low. (c) Areal strain changes at Sakurajima calculated by using the data recorded at 3 GNSS stations between 2012 and 2015. The 10-days-long median filter is applied to the time series of daily areal strains. Two red dashed lines indicate $\pm 3\sigma$ of areal strain change.

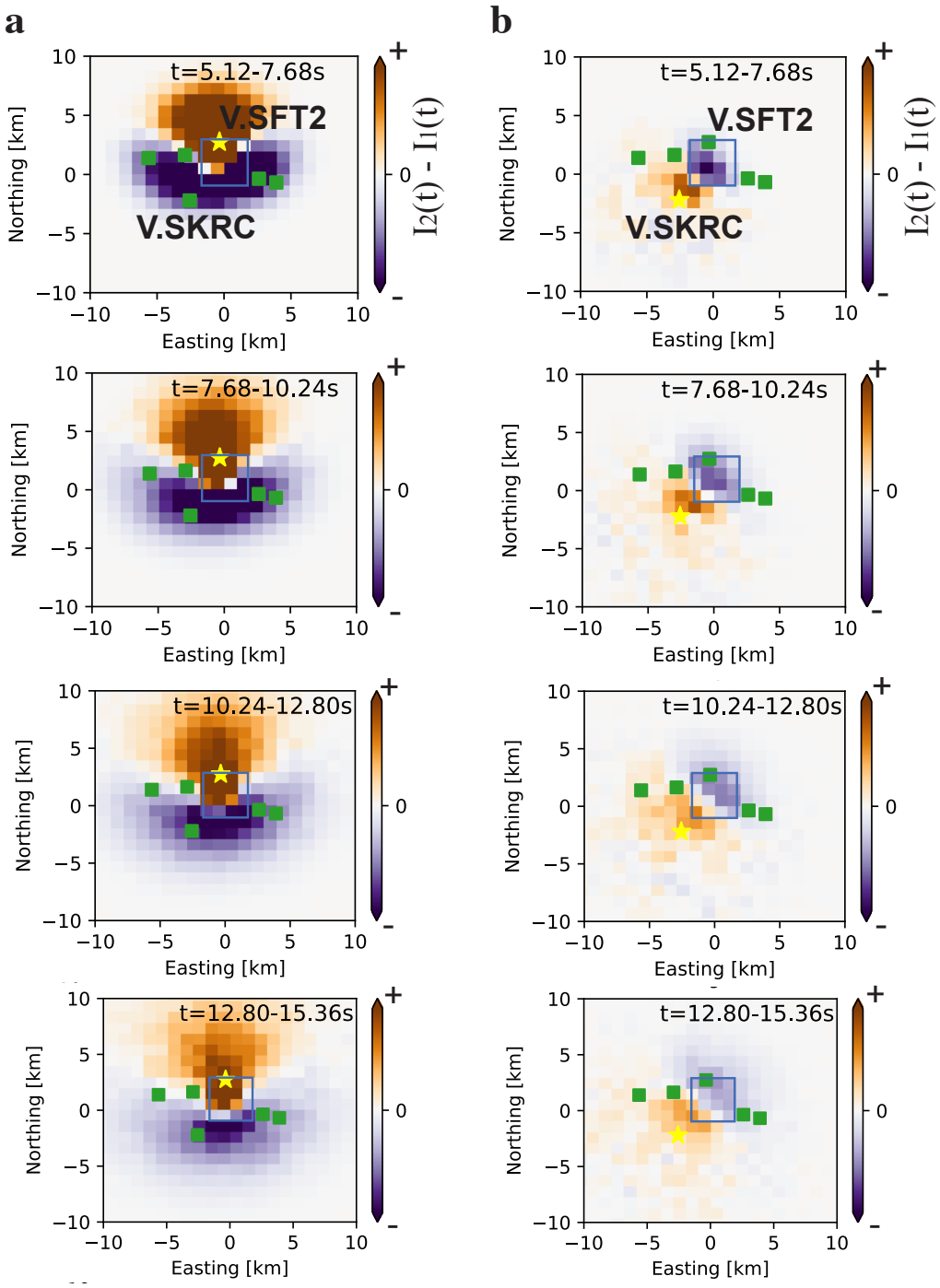

Figure 5.9 Spatial distributions of energy densities calculated by using the Direct Simulation Monte Carlo (DSMC) method [*Yoshimoto*, 2000] for four time windows. Blue rectangles on each panel indicate the change region between Period II and Period III. Red and blue indicate energy increases and decreases associated with the scattering coefficient change, respectively. (a) V.SFT2 is assumed as a source, and V.SKRC is assumed as a receiver. (b) V.SKRC is assumed as a source, and V.SFT2 is assumed as a receiver.

Chapter 6

Discussion

6.1 Future development of space-time imaging of seismic scattering properties

In chapter 5, we estimated the change regions of seismic scattering properties associated with the 2015 dike intrusion event at Sakurajima volcano by modeling multiple scattering in the change region. As discussed in chapter 5, applying linear least-squares inversion is difficult in a multiple scattering regime, because the size of small cells is set to be smaller than the scattering mean free path so that the scattering occurs only once within each small cell. Therefore, we proposed another approach to estimate a change region. Although this method is applicable even in a strong scattering regime, it is hard to assume multiple change regions due to the high calculation cost. If we assume two change regions simultaneously, we need to conduct Monte Carlo simulations for more than 10^7 models (chapter 5). If linear least-squares inversions are applicable, we can reduce the calculation cost. In chapter 4, we confirmed that sparse modeling is useful to locate change regions of seismic scattering properties from the small data set. The sparse modeling can be also useful for an imaging of seismic scattering properties in a multiple scattering regime. In the case of the 2008 Iwate-Miyagi Nairiku earthquake (chapter 4), we confirmed that we can retrieve the change regions from only 5 stations (45 decoherence values). In the case of Sakurajima, six short-period seismometers of JMA are deployed to surround the craters, and the location of the dike intrusion is inside this network. Therefore, it might be possible to image seismic scattering properties using linear least-squares inversions with the sparse modeling. As shown in chapter 2, the scattering mean free path at Sakurajima is about 1-2 km. This means that the size of small cells in the linear least-squares inversions should be a few hundred meters, and about 400 small cells will be necessary if the size of the small cells is 500 m$\times$500 m. In chapter 5, we used 136 decoherence values, and this is about one third of the number of the model parameters.

Extending sensitivity kernels is also important to improve imaging methods. Figure 6.1 is a schematic picture of the future development of space-time imaging. In our study and

most of the previous studies have assumed 2-D simple structure (top panel of Figure 6.1). This should be the first step of imaging. The second step is assuming 3-D simple structure (middle panel of Figure 6.1). The previous studies on seismic scattering property changes and our studies conducted imagings using 2-D sensitivity kernels. Rayleigh waves are used in these studies, and hence we can discuss the depth of a change by considering the wavelengths of Rayleigh waves. Recently, Obermann et al. [2018] located the 3-D position of seismic velocity changes in the focal area of the 2008 Wenchuan earthquake, China, by using a linear combination of the body- and surface- wave sensitivity kernels. The depth of the hypocenter is about 19 km, and large velocity reductions were detected at depths of 20-30 km. Obermann et al. [2016] reported that body waves become predominant after 6-8 scattering mean free times. The mean free time in a multiple scattering regime is much shorter than that in a weak scattering regime. Therefore, considering both body- and surface- waves will be important especially for the imaging in a multiple scattering regime. The third step is to consider topography and layered structure (bottom panel of Figure 6.1). The sensitivity kernels used in our studies do not consider these complicated structures in the study areas. Kanu and Snieder [2015] numerically computed the sensitivity kernel which included topography. They computed the sensitivity kernels using finite difference method. Their results showed that the topography-induced scattering which trapped seismic waves in the near-surface layer affects the sensitivity kernels largely. The effect of the topography can affect the estimation results of seismic scattering property changes, especially at volcanoes. In some cases, both of seismic velocity and seismic scattering property changes occur associated with earthquakes and volcanic activities. For example, we detected about 97 % of Δg value around the south of the epicenter of the 2008 Iwate-Miyagi Nairiku earthquake in the 0.5-1 Hz band (chapter 4). Hobiger et al. [2012] detected about 0.6 % velocity decrease in the same region at the 0.5-1 Hz band. Obermann et al. [2014] estimated about 35 % seismic scattering property change and 0.8-2.0 % seismic velocity decreases around the focal area of the 2008 Wenchuan earthquake, China. However, the effect of the seismic velocity changes is not considered in the estimation of the spatial distribution of seismic scattering property changes. The equation to compute synthesized decoherence values include the Rayleigh wave velocity, c, and the decorrelation kernel K_{dc} (see also equation (3.2)). The Rayleigh wave velocity c is assumed to be spatially uniform, and on the calculation of the decorrelation kernel, we also assumed the seismic velocity is spatially uniform. To consider seismic velocity changes in the estimation of the spatial distribution of seismic scattering property changes, we need to extend the estimation method.

6.2 Structural monitoring with multi parameters

As mentioned in chapter 1, seismic velocity changes have been widely estimated by many previous studies. In the previous studies that conducted space-time imaging of seismic scattering properties also estimated spatial distributions of seismic velocity changes [*Obermann et al.*, 2013; *Obermann et al.*, 2014; *Hillers et al.*, 2015; *Machacca et al.*, 2019]. The seismic velocity and seismic scattering property changes are sensitive to different spatial scales of structural changes: The seismic velocity is sensitive to a structural change whose scale is much larger than a wavelength, and the seismic scattering is sensitive to a structural change whose scale is comparable to a wavelength. Therefore, measuring both of seismic velocity and scattering property changes is important in structural monitoring. As we can see in Figure 5.8 (b), we could not estimate seismic velocity changes associated with the 2015 Sakurajima dike intrusion event due to large decoherences. We can measure seismic scattering property changes even in such a case.

Rayleigh waves have been used in many seismic interferometry analyses, and hence changes of S-wave velocities have been focused. On the other hand, Takano et al. [2019] succeeded in detecting about 2 % P-wave velocity decrease using the data from a dense array at Reunion island and interpreted such a velocity reduction might have been caused by an inflation of a volcanic pressure source at the shallow depth. A value of V_P/V_S reflects physical property of rocks: a kind of the rock and its fluid content. Estimating changes of both of P- and S-wave will be useful to interpret a cause of structural changes.

Shear wave splitting represents a dominant direction of anisotropy (orientation of cracks) and crack densities in a study area. Changes of seismic anisotropies associated with earthquakes and volcanic activities have been reported in some previous studies [e.g., *Liu et al.*, 2007; *Savage et al.*, 2015; *Saade et al.*, 2017], suggesting that measuring seismic anisotropies will be also useful for the structural monitoring.

In our studies, we assumed spatially uniform intrinsic absorptions. However, there are spatial variations of intrinsic attenuations in reality [e.g., *Calcoré and Sato*, 2010; *Takeuchi*, 2016; *Mayor et al.*, 2016; *Ogiso*, 2019]. For example, Mayor et al. [2016] estimated spatial distributions of intrinsic absorptions in the Alps from data of natural earthquakes by using absorption sensitivity kernels which were developed by Mayor et al. [2014] and Margerin et al. [2016]. The results around 1 Hz band showed that regions of high intrinsic absorption were correlated with the location of major Cenozoic flexural and extensional basins. The physical mechanisms of scattering attenuations and intrinsic absorptions are different. Therefore, estimating both of their spatial distributions will be

important.

There are many kinds of physical parameters we can use in structural monitoring. Measuring these parameters simultaneously will improve our understanding of the nature of the structural changes. Seismic interferometry is a useful tool to conduct such observations with multi parameters. Rock physics is helpful to interpret the results of seismic interferometry analyses.

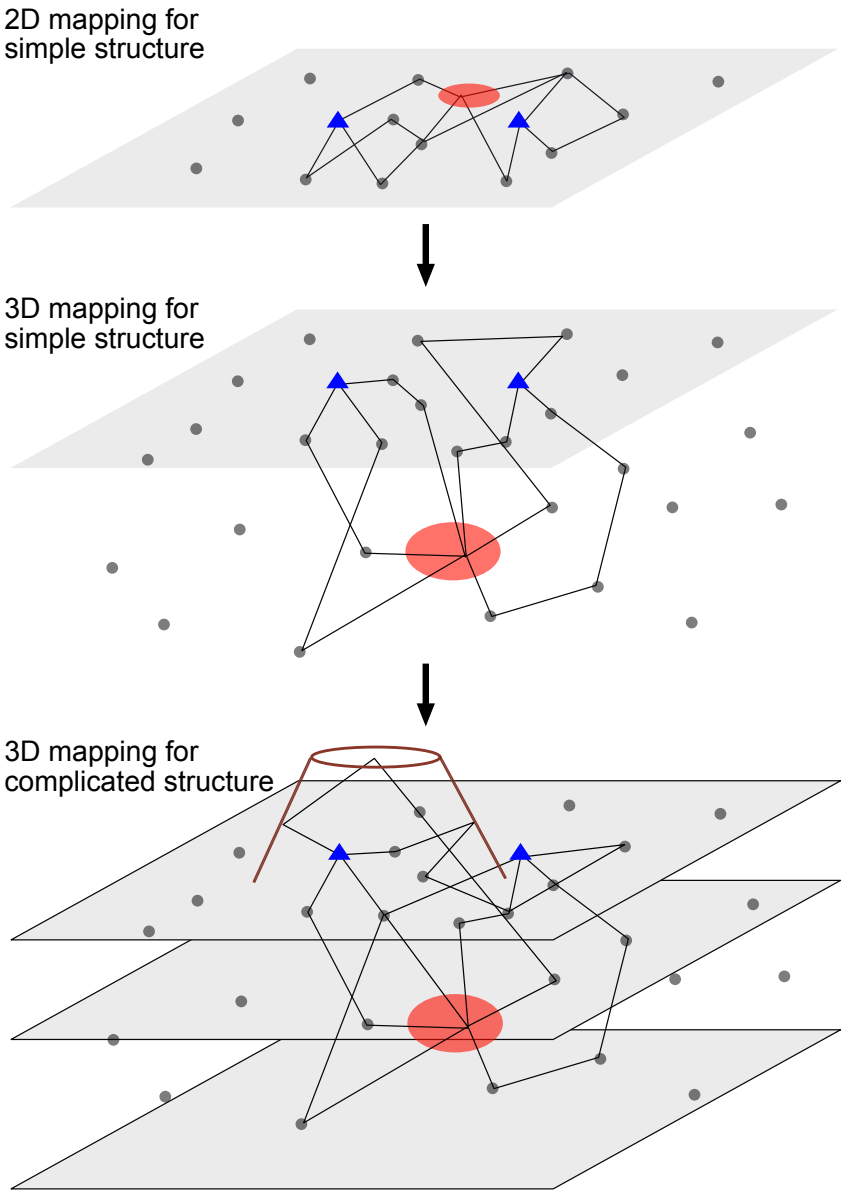

Figure 6.1 Schematic picture of the future development of space-time imaging.

Chapter 7

Conclusion

We developed a self-contained approach for space-time changes of seismic scattering properties based on seismic interferometry.

Firstly, we developed a passive estimation method of scattering and intrinsic absorption parameters and validated it by comparing results from our passive method and that from active shot records at Sakurajima volcano, Japan. The estimated parameters from seismic ambient noise CCFs were estimated to be 1.6-2.4 km and 0.04-0.06 s^{-1} at 0.5-1 Hz, 1.6-2.0 km and 0.08-0.09 s^{-1} at 1-2 Hz, and 1.6-3.2 km and 0.16-0.18 s^{-1} at 2-4 Hz, respectively. These values were consistent with those from active shot records at the 1-2 Hz and 2-4 Hz bands. Moreover, we explored an appropriate calculation procedure of ambient noise CCFs. In the case of applying one-bit normalization and spectral whitening which have been widely used in seismic interferometry analyses, scattering mean free paths were not constrained well and intrinsic absorption parameters were underestimated. Therefore, we concluded that it is better to apply temporal flattening for the estimation of scattering and intrinsic absorption parameters. We also estimated these parameters in the focal area of the 2008 Iwate-Miyagi Nairiku earthquake and at Miyakejima volcano, Japan. The scattering mean free path and intrinsic absorption parameter in the focal area of the Iwate-Miyagi Nairiku earthquake were estimated to be 30 km and 0.02 s^{-1} at the 0.5-1 Hz band. At Miyakejima, the scattering mean free paths were estimated to be 1.6 km at the 1-2 Hz band and 2.0 km at the 2-4 Hz band, respectively. The intrinsic absorption parameters were estimated to be 0.12 s^{-1} at the 1-2 Hz band and 0.16 s^{-1} at the 2-4 Hz band, respectively. The estimated scattering mean free paths at Sakurajima and Miyakejima were 2-3 orders shorter than those in non-volcanic regions. These results suggest that medium heterogeneities are strong at shallow parts of these active volcanoes.

Secondly, we estimated spatio-temporal changes of seismic scattering properties in the northeast part of Japan from 2008 to 2012, which is in a weak scattering regime. This is the first study which estimated spatial distributions of seismic scattering property changes in this region. Significant seismic scattering property changes were estimated around the epicenter of the 2008 Iwate-Miyagi Nairiku earthquake. The maximum Δg value was

5.7×10^{-4} km^{-1} ($\Delta g/g_0$ = 5.7 %). The large seismic scattering property change that we estimated at the south of the main shock was consistent with such observations. We interpreted that structural changes caused by the large slip and/or strong motions introduced the large seismic scattering property change in the shallow medium to the south of the epicenter. We also detected significant seismic scattering property changes around some active volcanoes in Tohoku region associated with the 2011 Tohoku-Oki earthquake. The maximum change was estimated around the Bandai volcano and its Δg value was 3.6×10^{-4} km^{-1} ($\Delta g/g_0$ = 3.6 %). Significant seismic velocity decreases and subsidences associated with this earthquake were detected by seismic interferometry and analyses of InSAR data. Our results provided a new piece of evidence that significant structural changes occurred beneath active volcanoes in Tohoku region associated with the 2011 Tohoku-Oki earthquake. In the southwest part of Tohoku region, strong seasonal seismic scattering property changes were detected, and its maximum Δg value was estimated to be 3.0×10^{-4} km^{-1} ($\Delta g/g_0$=3.0 %) in winter. Regarding seismic velocities, the effect of external environmental perturbations have been reported by many previous studies. However, the meteorological effects to seismic scattering property changes are not evaluated yet, and this will be important for interpreting seismic scattering property changes as well.

Thirdly, we applied sparse modeling to the imaging of seismic scattering property changes related to the 2008 Iwate-Miyagi Nairiku earthquake. We used 17 seismic stations to validate the applicability of the sparse modeling. The region of the largest seismic scattering property changes was located at the south of the epicenter. The maximum value of Δg, a variation of scattering coefficient, at this region was estimated to be 0.032 km^{-1} ($\Delta g/g_0$=97 %). We also conducted the ordinary linear least-squares inversion with the ℓ^2 norm regularization. The result from the sparse modeling and that from the ℓ^2 norm regularization were consistent, and this indicates that the result from the sparse modeling is reliable. We explored the applicability of the sparse modeling by reducing the number of seismic stations and confirmed that we can retrieve the change regions from 5 stations which are deployed to surround the change regions. In contrast, we could not retrieve the result from all 17 stations in the case of applying ℓ^2 norm regularization to the data from these 5 stations. In terms of the ℓ^2 norm regularization, 15 stations were necessary to retrieve the result from all 17 stations. In practice, the number of seismic stations that we can use for imaging is limited, and these results suggest that the sparse modeling will be useful to estimate the spatial distribution of seismic scattering property changes from the small data set.

Finally, we estimated a change region of seismic scattering properties associated with

the 2015 dike intrusion event at Sakurajima volcano. In previous studies, an inverse problem is linearized by assuming the scattering property changes affect the scattering only once. However, this approach is difficult to apply in a multiple scattering regime. Therefore, we proposed a new alternative method for estimating parameters of the change region which is applicable even in a multiple scattering regime. The estimated change region extended widely around Kita-dake and Minami-dake with Δg of 0.25 km^{-1} and 1.10 km^{-1} in the periods of Apr. 1 - May 31 and Jul. 6 - Aug. 14 (before the dike intrusion). The change region was located around the dike (east to Minami-dake) with Δg of 2.45 km^{-1} in the period of Aug. 16 - Sep. 15 (just after the dike intrusion). Our method is applicable even in such a strong scattering case though the number of the change region is assumed to be only one. This method should be useful for the continuous monitoring of structural changes beneath active volcanoes.

Estimating space-time changes of seismic scattering properties will be important for structural monitoring. In this thesis, we develop a self-contained approach to the estimation of space-time changes of seismic scattering properties based on seismic interferometry. By applying the appropriate imaging method, we can locate significant seismic scattering changes both in a weak scattering regime and strong scattering regime. Moreover, the passive estimation of scattering and intrinsic absorption parameters and the sparse modeling will be useful to improve the applicability of the passive time-lapse imaging. By conducting imaging in various regions and comparing the results with other observations, relationships between seismic scattering changes and other changes will be understood. This should contribute to the monitoring of the dynamic Earth and the understanding of their physical mechanisms.

References

Aoi, S., T. Kunugi, and H. Fujiwara (2008), Trampoline effect in extreme ground motions, *Science*, **322**, 727–730, doi:10.1126/science.1163113.

Asano, Y., and A. Hasegawa (2004), Imaging the fault zones of the 2000 western Tottori earthquake by a new inversion method to estimate three-dimensional distribution of the scattering coefficient, *J. Geophys. Res.*, 109:B06306, DOI:10.1029/2003JB002761.

Beck, A., and M. Teboulle (2009), A Fast Iterative Shrinkage-Thresholding Algorithm for Linear Inverse Problems, *SIAM Journal on Imaging Sciences*, **2**(1):183–202.

Beck, A., and M. Teboulle (2010), Gradient-based algorithms with applications to signal recovery problems, *Convex Optimization in Signal Processing and Communications, Cambridge*, U.K.:Cambridge Univ. Press.

Bensen, G. D., M. H. Ritzwoller, M. P. Barmin, A. L. Levshin, F. Lin, M. P. Moschetti, N. M. Shapiro, and Y. Yang, (2007), Processing seismic ambient noise data to obtain reliable broad-band surface wave dispersion measurements, *Geophys. J. Int.*, **169**, 1239–1260.

Brenguier, F., M. Campillo, C. Hadziioannou, N. M. Shapiro, R. M. Nadeau, E. Larose (2008a), Postseismic relaxation along the San Andreas fault at Parkfield from continuous seismological observations, *Science*, **321**(5895), 1478–1481, https://doi.org/10.1126/science.1160943.

Brenguier, F., M. Campillo, T. Takeda, Y. Aoki, N.M. Shapiro, X. Briand, K. Emoto, and H. Miyake (2014), Mapping pressurized volcanic fluids from induced crustal seismic velocity drops, *Science*, **345**, 80–82, 10.1126/science.1254073.

Carcolé, E., and H. Sato (2010), Spatial distribution of scattering loss and intrinsic absorption of short-period S waves in the lithosphere of Japan on the basis of the multiple lapse time window analysis of Hi-net data, *Geophys. J. Int.*, **180**(1), 268–290. https://doi.org/10.1111/j.1365-246X.2009.04394.x.

Claerbout, J. F., and F. Muir (1973), Robust modeling with erratic data, *Geophysics*,

38(5), 826–844, doi:10.1190/1.1440378.

Curtis, A., P. Gerstoft, H. Sato, R. Snieder, and K. Wapenaar (2006), Seismic interferometry-Turning noise into signal, *The Leading Edge*, **25**:1082–1092, doi:10.1016/j.jvolgeores.2006.04.003.

Evans, E. L., and B. J. Meade (2012), Geodetic imaging of coseismic slip and postseismic afterslip: Sparsity promoting methods applied to the great Tohoku earthquake, *Geophys. Res. Lett.*, **39**, L11314, doi:10.1029/2012GL051990.

Fehler, M., M. Hoshiba, H. Sato, and K. Obara (1992), Separation of scattering and intrinsic attenuation for the Kanto-Tokai region, Japan, using measurements of S-wave energy versus hypocentral distance, *Geophys. J. Int.*, **108**(3), 787–800. https://doi.org/10.1111/j.1365-246X.1992.tb03470.x.

Hanasoge, S. M. (2013), The influence of noise sources on cross-correlation amplitudes, *Geophys. J. Int.*, **192**(1), 295–309.

Hatovec-Ellis, A. J., J. S. Gomberg, J. E. Vidale, and K. C. Creager (2014), A continuous record of inter-eruption velocity change at Mount St. Helens from coda-wave interferometry, *J. Geophys. Res., in press.*, **119**, 2199–2214.

Hillers, G., S. Husen, A. Obermann, T. Planès, E. Larose, and M. Campillo (2015), Noise-based monitoring and imaging of aseismic transient deformation induced by the 2006 Basel reservoir stimulation, *Geophysics*, **80**:4, KS51-KS68.

Hirose, T., H. Nakahara, and T. Nishimura (2017), Combined use of repeated active shots and ambient noise to detect temporal changes in seismic velocity: Application to Sakurajima volcano, Japan, *Earth, Planets and Space*, **69**(1), 42.

Hirose, T., H. Nakahara, and T. Nishimura (2019), A passive estimation method of scattering and intrinsic absorption parameters from envelopes of seismic ambient noise cross-correlation functions, *Geophys. Res. Lett.*, **46**, 3634–3642, doi: 10.1029/2018GL080553.

Hobiger, M., U. Wegler, K. Shiomi, and H. Nakahara (2012), Coseismic and postseismic elastic wave velocity variations caused by the 2008 Iwate-Miyagi Nairiku earthquake, Japan, *J. Geophys. Res.*, **117**, B09313, doi:10.1029/2012JB009402.

Hobiger, M., U. Wegler, K. Shiomi, H. Nakahara (2014), Single-station cross-correlation analysis of ambient seismic noise: application to stations in the surround-

ings of the 2008 Iwate-Miyagi Nairiku earthquake, *Geophys. J. Int.*, 1**98**, 90–109, https://doi.org/10.1093/gji/ggu115.

Hoshiba, M. (1993), Separation of scattering attenuation and intrinsic absorption in Japan using the multiple lapse time window analysis of full seismogram envelope, *J. Geophys. Res.*, **98**:15, 809–15,824, DOI 10.1029/93JB00347.

Hotta, K., M. Iguchi, and T. Tameguri (2016a), Rapid dike intrusion into Sakurajima volcano on August 15, 2015, as detected by multi-parameter ground deformation observations, *Earth Planets Space*, **68**, doi:10.1186/s40623-016-0450-0.

Hotta, K., M. Iguchi, T. Ohkura, K. Yamamoto, and T. Tameguri (2016b), Comparison between ground deformation events at Sakurajima from January to June 2015 and on August 15, 2015, Japan Geoscience Union Meeting 2016, SVC47-03.

Iguchi M., T. Tameguri, Y. Ohta, S. Ueki, and S. Nakao (2013), Charactristics of Volcanic Activity at Sakurajima Volcano's Showa Crater During the Period 2006 to 2011, *Bull Volcanol Soc Japan*, *58*:115–135.

Iinuma, T., et al. (2009), Aseismic slow slip on an inland active fault triggered by a nearby shallow event, the 2008 Iwate-Miyagi Nairiku earthquake (Mw6.8), *Geophys. Res. Lett.*, **36**, L20308, doi:10.1029/2009GL040063.

Japan Meteorological Agency (2015) (3) Sakurajima. Documents for the 133th meeting of the coordinating committee for prediction of volcanic eruptions (in Japanese) Accessed 31 March 2018, `http://www.data.jma.go.jp/svd/vois/data/tokyo/STOCK/kaisetsu/CCPVE/shiryo/133/133_03.pdf`.

Japan Meteorological Agency (2016) (2-1) Sakurajima. Documents for the 134th meeting of the coordinating committee for prediction of volcanic eruptions (in Japanese) Accessed 31 March 2018, `http://www.data.jma.go.jp/svd/vois/data/tokyo/STOCK/kaisetsu/CCPVE/shiryo/134/134_02-1.pdf`.

Kanu, C., and R. Snieder (2015), Numerical computation of the sensitivity kernel for monitoring weak changes with multiply scattered acoustic waves, *Geophys. J. Int.*, **203**(3), 1923–1936, https://doi.org/10.1093/gji/ggv391.

Larose, E., A. Derode, M. Campillo, and M. Fink (2004), Imaging from one - bit correlations of wideband diffuse wave fields, *Journal of Applied Physics*, **95**(12), 8393–8399,

https://doi.org/10.1063/1.1739529.

Larose, E., T. Planès, V. Rosetto, and L. Margerin (2010), Locating a small change in a multiple scattering regime, *App. Phys. Lett.*, **96**.

Larose, E., A. Obermann, A. Digulescu, T. Planès, J.F. Chaix, F. Mazerolle, and G. Moreau (2015), Locating and characterizing a crack in concrete with diffuse ultrasound: A four-point bending test, *J. acoust. Soc. Am.*, **138**(1), 232–241.

Liu, X., Y. Ben-Zion, and D. Zigone (2015), Extracting seismic attenuation coefficients from cross-correlations of ambient noise at linear triplets of stations, *Geophys. J. Int.*, **203**(2), 1149–1163, https://doi.org/10.1093/gji/ggv357.

Liu, Y., H. Zhang, C. Thurber, and S. Roecker (2007) Shear wave anisotropy in the crust around the San Andreas fault near Parkfield: spatial and temporal analysis, *Geophys. J. Int.*, **172**, 957–970.

Machacca-Puma R., P. Lesage, E. Larose, P. Lacroix, and R. M. Anccasi-Figueroa (2019), Detection of pre-eruptive seismic velocity variations at an andesitic volcano using ambient noise correlation on 3-component stations: Ubinas volcano, Peru, 2014, *Journal of Volcanology and Geothermal Research*, **381**, 83–100, https://doi.org/10.1016/j.jvolgeores.2019.05.014.

Margerin, L., T. Planès, J. Mayor, and M. Calvet (2016), Sensitivity kernels for coda-wave interferometry and scattering tomography: theory and numerical evaluation in two-dimensional anisotropically scattering media, *Geophys. J. Int.*, **204**, 650–666, https://doi.org/10.1093/gji/ggv470.

Matsumoto, S., K. Obara, K. Yoshimoto, T. Saito, A. Hasegawa, and A. Ito (1999), Imaging of crustal inhomogeneous structure of the crust beneath Ou Backbone Range, northeastern Japan, based on small aperture seismic array obsevations, *Zisin* (in Japanese) **52**:293–297.

Mayor, J., L. Margerin, and M. Calvet (2014), Sensitivity of coda waves to spatial variations of absorption and scattering: radiative transfer theory and 2-D examples, *Geophys. J. Int.*, **197**, 1117–1137, https://doi.org/10.1093/gji/ggu046.

Mayor, J., M. Calvet, L. Margerin, O. Vanderhaeghe, and P. Traversa (2016), Crustal structure of the alps as seen by attenuation tomography, *Earth planet. Sci. Lett.*, **439**,

71–80.

Meier, U., N. M. Shapiro, and F. Brenguier (2010), Detecting seasonal variations in seismic velocities within Los Angeles basin from correlations of ambient seismic noise, *Geophys. J. Int.*, **181**(2), 985–996.

Morishita, Y., T. Kobayashi, and H. Yarai (2016), Three-dimensional deformation mapping of a dike intrusion event in Sakurajima in 2015 by exploiting the right- and left-looking ALOS-2 InSAR, *Geophys. Res. Lett.*, **43**, doi:10.1002/2016GL068293.

Nakahara, H. (2015), Auto correlation analysis of coda waves from local earthquakes for detecting temporal changes in shallow subsurface structures: the 2011 Tohoku-Oki, Japan Earthquake, *Pure and Applied Geophysics*, **172**, 213–224, doi:10.1007/s00024-014-0849-0.

Nakata, N., and R. Snieder (2011), Near-surface weakening in Japan after the 2011 Tohoku-Oki earthquake, *Geophys. Res. Lett.*, **38**, L17302, doi: 10.1029/2011GL048800.

Nakata, R., T. Kuwatani, M. Okada, and T. Hori (2016), Geodetic inversion for spatial distribution of slip under smoothness, discontinuity, and sparsity constraints, *Earth Planets Space*, **68**:20.

National Research Institute for Earth Science and Disaster Resilience (2019), NIED Hi-net, National Research Institute for Earth Science and Disaster Resilience, doi:10.17598/NIED.0003.

National Research Institute for Earth Science and Disaster Resilience (2019), NIED K-NET, KiK-net, National Research Institute for Earth Science and Disaster Resilience, doi:10.17598/NIED.0004.

Nishigami, K. (2000), Deep crustal heterogeneity along and around the San Andreas fault system in central California and its relation to the segmentation, *J. Geophys. Res.*, **105**:7983–7998, DOI 10.1029/1999JB900381.

Obermann, A., T. Planès, E. Larose, and M. Campillo (2013a), Imaging preeruptive and coeruptive structural and mechanical changes of a volcano with ambient seismic noise, *J. Geophys. Res.*, **118**, 6285–6294, doi:10.1002/2013JB010399.

Obermann, A., B. Froment, M. Campillo, E. Larose, T. Planès, B. Valette, J. H. Chen, and Q. Y. Liu (2014), Seismic noise correlations to image structural and mechanical changes

associated with the Mw7.9 2008 Wenchuan earthquake, *J. Geophys.*, **119**, 3155–3168, doi:10.1002/2013JB010932.

Obermann, A., T. Planès, C. Hadziioannou, and M. Campillo (2016), Lapse-time-dependent coda-wave depth sensitivity to local velocity perturbations in 3-D heterogeneous elastic media, *Geophys. J. Int.*, **207**(1), 59–66.

Obermann, A., T. Planès, E. larose, and M. Campillo (2018), 4-D Imaging of Subsurface Changes with Coda Waves: Numerical Studies of 3-D Combined Sensitivity Kernels and Applications to the Mw 7.9, 2008 Wenchuan Earthquake, *Pure Appl. Geophys.*, **176**(3), 1243–1254.

Ogiso, M. (2019) A method for mapping intrinsic attenuation factors and scattering coefficients of S waves in 3-D space and its application in southwestern Japan, *Geophys. J. Int.*, **216**(2), 948–957, https://doi.org/10.1093/gji/ggy468.

Ohta, Y., M. Ohzono, S. Miura, T. Iinuma, K. Tachibana, K. Takatsuka, K. Miyao, T. Sato, and N. Umino (2008), Coseismic fault model of the 2008 Iwate-Miyagi Nairiku earthquake deduced by a dense GPS network, *Earth Planets Space*, **60**, 1197–1201.

Parikh, N., and S.P. Boyd (2013), Proximal algorithms, *Foundations and Trends in Optimization*, **1**(3):123–231.

Planès, T., E. Larose, V. Rosetto, and L. Margerin (2015), Imaging multiple local changes in heterogeneous media with diffuse waves, *J. Acoust. Soc. Am.*, **137**(2), 660-667.

Poupinet, G., VL. Ellsworth, and J. Frechet (1984), Monitoring velocity variations in the crust using earth- quake doublets: An application to the Calaveras fault, California, *J. Geophys. Res.*, **89**:5719–5732, DOI 10.1029/JB089iB07p05719.

Prudencio, J., E. Del Pezzo, J.M. Ibáñez, E. Giampiccolo, and D. Patané (2015), Two - dimensional seismic attenuation images of Stromboli Island using active data, *Geophys. Res. Lett.*, **42**, 1717–1724.

Prudencio, J., Y. Aoki, M. Takeo, J.M. Ibáñez, E. Del Pezzo, and W.Z. Song, W. Z. (2017), Separation of scattering and intrinsic attenuation at Asama volcano (Japan): Evidence of high volcanic structural contrasts, *Journal of Volcanology and Geothermal Research*, 96–103.

Saade, M., J.P. Montagner, P. Roux, K. Shiomi, B. Enescu, and F. Brenguier (2017), Mon-

itoring of seismic anisotropy at the time of the 2008 Iwate-Miyagi (Japan) earthquake, *Geophys. J. Int.*, **211**(1), 483–497, https://doi.org/10.1093/gji/ggx321.

Santosa, F., and W. W. Symes (1986), Linear inversion of band-limited reflection seismograms, *SIAM J. Sci. Stat. Comput.*, **7**(4), 1307–1330, doi:10.1137/0907087.

Sato, H. (1993), Energy Transportation In One- and Two-Dimensional Scattering Media: Analytic Solutions of the Multiple Isotropic Scattering Model, *Geophys. J. Int.*, **112**:141–146, doi:10.1111/j.1365-246X.1993.tb01443.x.

Sato, H., M. C. Fehler, and T. Maeda (2012), Seismic Wave Propagation and Scattering in the Heterogeneous Earth, vol. 496, Springer, Berlin.

Savage, M. K., et al. (2015), Seismic anisotropy and its precursory change before eruptions at Piton de la Fournaise volcano, La Réunion, *J. Geophys. Res.*, **120**, 3430–3458, doi:10.1002/2014JB011665.

Sawazaki K., H. Kimura, K. Shiomi, N. Uchida, R. Takagi, and R. Snieder (2015), Depth-dependence of seismic velocity change associated with the 2011 Tohoku earthquake, Japan, revealed from repeating earthquake analysis and finite-difference wave propagation simulation, *Geophys. J. Int.*, **201**(2), 741–763, https://doi.org/10.1093/gji/ggv014.

Sens-Schönfelder, C., and U. Wegler (2006), Passive image interferometry and seasonal variations of seismic velocities at Merapi Volcano, Indonesia, *Geophys. Res. Lett.*, **33**, L21302. https://doi.org/10.1029/2006GL027797.

Shang, T., and L. Gao (1988), Transportation theory of multiple scattering and its application to seismic coda waves of impulsive source, *Scientia Sinica* (series B, China), **31**, 1503–1514.

Shapiro, N. and M. Campillo (2004), Emergence of broadband Rayleigh waves from correlations of the ambient seismic noise, *Geophys. Res. Lett.*, **31**(7): L07614 doi:10.1029/2004gl019491.

Shapiro, N. M., M. H. Ritzwoller, and G. D. Bensen (2006), Source location of the 26 sec microseism from cross-correlations of ambient seismic noise, *Geophys. Res. Lett.*, **33**, L18310, https://doi.org/10.1029/2006GL027010.

Silver, P. G., T. M. Daley, F. Niu, and E. L. Majer (2007), Active source monitoring of cross-well seismic travel time for stress-induced changes, *Bulletin of the Seismological*

Society of America, **97**(1B), 281–293.

Snieder, R., A. Grêt, H. Douma, and J. Scales (2002), Coda Wave Interferometry for Estimating Nonlinear Behavior in Seismic Velocity, *Science*, **295**(5563):2253–2255.

Snieder, R. (2004), Extracting the Green's function from the correlation of coda waves: A derivation based on stationary phase, *Phys. Rev. E.*, **69**:046610, DOI: 10.1103/PhysRevE.69.046610.

Snieder, R. (2006), The theory of coda wave interferometry, *Pure Appl. Geophys.*, **163**:455–473.

Stehly, L., M. Campillo, and N. M. Shapiro (2006), A study of the seismic noise from its long-range correlation properties, *J. Geophys. Res.*, **111**, B10306. https://doi.org/10.1029/2005JB004237.

Suzuki, W., A. Shin, and H. Sekiguchi (2010), Rupture Process of the 2008 Iwate-Miyagi Nairiku, Japan, Earthquake Derived from Near-Source Strong-Motion Records, *Bull. Seismol. Soc. Am.*, **100**(1), 256–266, doi: 10.1785/0120090043.

Takada, Y., and Y. Fukushima (2013), Volcanic subsidence triggered by the 2011 Tohoku earthquake in Japan, *Nat. Geosci.*,**6**, 637–641, doi:10.1038/ngeo1857.

Takagi, R., T. Okada, H. Nakahara, N. Umino, and A. Hasegawa (2012), Coseismic velocity change in and around the focal region of the 2008 Iwate - Miyagi Nairiku earthquake, *J. Geophys. Res.*, **117**, B06315, doi:10.1029/2012JB009252.

Takagi, R., and T. Okada (2012), Temporal changes in shear velocity and polarization anisotropy related to the 2011 M9.0 Tohoku-Oki earthquake examined using KiK-net vertical array data, *Geophys. Res. Lett.*, **39**, L09310, doi: 10.1029/2012GL051342.

Takano, T., T. Nishimura, and H. Nakahara (2017), Seismic velocity changes concentrated at the shallow structure as inferred from correlation analyses of ambient noise during volcano deformation at Izu-Oshima, Japan, *J. Geophys. Res.*, **122**, 6721–6736, DOI:10.1002/2017JB014340.

Takano, T. (2019), Temporal changes in seismic velocity of shallow structures at active volcanoes as inferred from analyses of ambient noise correlations, *PhD thesis*, Tohoku University, Japan.

Takeuchi, N. (2016), Differential Monte Carlo method for computing seismogram envelopes and their partial derivatives, *J. Geophys. Res.*, **121**, 3428–3444, doi:10.1002/2015JB012661.

Tibshirani, R. (1996), Regression Shrinkage and Selection via the Lasso, *Journal of the Royal Statistical Society*, Series B, **58**(1), 267–288, http://www.jstor.org/stable/2346178.

Tsai, V. C. (2011), A model for seasonal changes in GPS positions and seismic wave speeds due to thermoelastic and hydrologic variations, *J. Geophys. Res.*, **116**, B04404. https://doi.org/10.1029/2010JB008156.

Tsutsui, T., M. Iguchi, T. Tameguri, and H. Nakamichi (2016), Structual evolution beneath Sakurajima Volcano, Japan, revealed through rounds of controlled seismic experiments, *J. Volcanol. Geotherm. Res.*, **315**:1–14: doi:10.1016/j.jvolgeores.2016.02.008.

Wang, H., and C. Leng. (2009) Shrinkage tuning parameter selection with a diverging number of parameters, *Journal of Royal Statistical Society*, Series B, **71**(3), 671–683.

Wang, Q.-Y., F. Brenguier, M. Campillo, A. Lecointre, T. Takeda, and Y. Aoki, (2017), Seasonal crustal seismic velocity changes throughout Japan, *J. Geophys. Res.*, **122**, 7987–8002.

Weaver, R. L. (2011a), On the amplitudes of correlations and the inference of attenuations, specific intensities and site factors from ambient noise, *Comptes Rendus Geoscience*, **343**(8–9), 615–622.

Wegler, U., and B. Lühr (2001), Scattering behaviour at Merapi volcano (Java) revealed from an active seismic experiment, Tohoku earthquake, Japan, revealed from repeating earthquake analysis and finite-difference wave propagation simulation, *Geophys. J. Int.*, **145**(3), 579–592. https://doi.org/10.1046/j.1365-246x.2001.01390.x.

Wegler, U., and C. Sens-Schönfelder (2007), Fault zone monitoring with passive image interferometry, *Geophys. J. Int.*, **168**(3), 1029–1033. https://doi.org/10.1111/j.1365-246X.2006.03284.x.

Yamamoto, M., and H. Sato (2010), Multiple scattering and mode conversion revealed by an active seismic experiment at Asama volcano, Japan, *J. Geophys. Res.*, **115**, B07304. https://doi.org/10.1029/2009JB007109.

Yao, H., P. Gerstoft, P. M. Shearer, and C. Mecklenbräuker (2011), Compressive sensing of the Tohoku-Oki Mw 9.0 earthquake: Frequency-dependent rupture modes, *Geophys. Res. Lett.*, **38**, L20310, doi:10.1029/2011GL049223.

Yoshimoto, K. (2000), Monte-Carlo simulation of seismogram envelope in scattering media, *J. Geophys. Res.*, **105**:6153-6161, DOI:10.1029/1999JB900437.

Zhang, J., and X. Yang (2013), Extracting surface wave attenuation from seismic noise using correlation of the coda of correlation, *J. Geophys. Res.*, **118**, 2191–2205, https://doi.org/10.1002/jgrb.50186.